



# Point-of-Care Systems for Cellular Analysis

## Citation

Song, Jun. 2015. Point-of-Care Systems for Cellular Analysis. Doctoral dissertation, Harvard University, Graduate School of Arts & Sciences.

## Permanent link

<http://nrs.harvard.edu/urn-3:HUL.InstRepos:14226047>

## Terms of Use

This article was downloaded from Harvard University's DASH repository, and is made available under the terms and conditions applicable to Other Posted Material, as set forth at <http://nrs.harvard.edu/urn-3:HUL.InstRepos:dash.current.terms-of-use#LAA>

## Share Your Story

The Harvard community has made this article openly available.  
Please share how this access benefits you. [Submit a story](#).

[Accessibility](#)

# **Point-of-Care Systems for Cellular Analysis**

A Dissertation Presented

by

Jun Song

to

The School of Engineering and Applied Sciences

In partial fulfillment of the requirements

for the degree of

Doctor of Philosophy

in the subject of

Applied Physics

Harvard University

Cambridge Massachusetts

December 2014

© 2014 by Jun Song

All rights reserved.

Dissertation co-advisors: Prof. Ralph Weissleder and Prof. Robert Westervelt

Author: Jun Song

Point-of-Care Systems for Cellular Analysis

## **Abstract**

Cellular analysis is a vital part of diagnostics testing for most diseases. The development of modern technologies has led to great advancement in this task. However, the use of cellular analysis systems is limited mainly to laboratories and clinics due to their high cost and large size. Providing affordable and accessible diagnostic testing to the majority of population in the developing world and resources-limited regions remains a technical challenge.

To overcome this challenge, cost-effective and portable point-of-care (POC) systems have emerged in recent years as a promising approach. This thesis focuses on the development of such POC systems for the purpose of cellular analysis. These systems include sub-pixel resolution holographic imager for cellular profiling and microfluidic platforms for sorting cell populations in clinical samples and capturing single cells.

First, a new lens-free holographic system is reported as a portable imaging tool for fast screening and profiling of individual cells. Compared to conventional microscopy, this system is cheaper in cost, and portable; it can provide fast automatic detection over a large field-of-view and profile cells for in terms of their molecular properties.

To enhance the resolution of the lens-free holographic system, a novel sub-pixel resolution enhancement method has been developed. Typical lens-free holographic systems are limited in resolution by the pixel size of their inherent image sensors. The developed method can overcome this limitation by applying compressive sensing strategy to the reconstruction process.

Compared to other resolution enhancement methods for lens-free holography, this method does not require additional hardware or multiple exposures in measurement, thus provides the potential for fast imaging of sub-pixel targets. It can also be further applied to other nonlinear holographic imaging systems.

In addition to cell imaging, novel microfluidic platforms were also developed to address the challenges in separating and capturing scant cells in blood or other fluid samples from patients.

A single-cell capturing system is developed for the detection of lymphoma from cerebral spinal fluid (CSF) samples. Compared to existing single-cell capturing systems, this chip offers the advantage of antibody-free trapping mechanism, large number of sites for high throughput screening, and special geometry that size-selectively captures lymphoid cells.

Blood sample usually contains a variety of cell populations which makes it difficult to sort low abundant cell for clinical diagnosis. To achieve high efficiency separation of cell populations in blood stream, a hybrid magnetic-microfluidic cell sorting system was developed. Compared with previous work, the new system achieved higher separation efficiency without damaging target cells; it is also easier to assemble and thus eliminates additional training needed for device operation.

These POC systems provide versatile approach for fast, cheap and accurate disease diagnosis. With further customization specific to the diseases and more clinical testing, they can be applied as powerful tools for more accessible healthcare in low-income and resources limited regions.

# Table of Contents

Abstract	iii
Table of Contents	v
Acknowledgement	viii
List of Figures	xi
List of Tables	xiii
Chapter 1 Introduction	1
1.1. Motivation	1
1.1.1. Point-of-Care (POC) diagnostic system	1
1.1.2. POC Systems for Cellular analysis	2
1.1.3. Optical POC Systems	3
1.1.4. Microfluidic POC System	4
1.2. Thesis organization	5
Chapter 2 Digital In-line Holography for Point-of-Care Diagnostics	6
2.1. Background	6
2.1.1. POC Imaging System	6
2.1.2. Digital In-line Holography	6
2.2. Methods	9
2.2.1. Digital Diffraction Diagnostics (D3) Platform	9
2.2.2. Reconstruction and Counting Algorithm	13
2.2.3. Target Cell Detection	16
2.2.4. D3 App and GPU Server	18
2.2.5. Cell Labeling Strategy	19
2.3. Demonstration	22
2.3.1. Reconstruction and Cell Detection	22
2.3.2. Quantitative Cell Profiling	26
2.4. Summary and Discussion	30
Chapter 3 Resolution Enhancement of Digital In-line Holography with Compressed Sensing	32
3.1. Background	32

3.1.1. Super-resolution Methods for Holography	32
3.1.2. Compressed Sensing for Holography	33
3.2. Methods	34
3.2.1. LDIH Measurement System	34
3.2.2. Imaging System Model	35
3.2.3. L0-norm minimization	37
3.2.4. Compressive LDIH Algorithm	38
3.3. Demonstration	41
3.3.1. Resolution of Compressive LDIH	41
3.3.2. Resolution Enhancement of Non-Phase Objects	43
3.3.3. Resolution Enhancement of Object Phase	43
3.4. Summary and Discussion	47
Chapter 4 Single-cell Capturing Chip for CNS Lymphoma Analysis	48
4.1. Background	48
4.1.1. CNS Lymphoma Diagnosis	48
4.2. Methods	51
4.2.1. System Design and Fabrication	51
4.2.2. System Characterization	57
4.2.3. Cell Line Profiling	62
4.2.4. Labeling Strategy	64
4.2.5. Imaging Analysis	66
4.3. Demonstration	69
4.3.1. On-Chip Cell Staining and Imaging	69
4.3.2. Analysis of Clinical Samples	72
4.3.3. Drug Sensitivity Testing	74
4.4 Summary and Discussion	76
Chapter 5 Magnetic-Microfluidic Chip for Circulating Tumor Cell Separation	78
5.1. Background	78
5.1.1. Separation of Circulating Tumor Cells (CTC)	78
5.1.2. Magnetic-microfluidic Cell Sorting	79
5.2. Methods	80

5.2.1. System Design	80
5.2.2. Magnetic Field Simulation	86
5.2.3. Magnetic Force Calculation	89
5.3. Demonstration	91
5.3.1. On-chip Bead Separation	91
5.3.2. On-chip Cell Sorting	96
5.4. Summary and Discussion	99
Chapter 6 Conclusion & Perspectives	100
6.1. Summary	100
6.2. Future directions	101
References	102



# Acknowledgement

There are many people I want to thank for supporting me through the past five years at Harvard and MGH. It has been a challenging journey and I would not have made it without their guidance, understanding, and encouragement.

First of all, I would like to thank my advisors and mentors Dr. Ralph Weissleder, Dr. Robert Westervelt and Dr. Hakho Lee. It's a great honor for me to have the opportunity of working with these top minds in science and medicine. Since I joined CSB, Dr. Ralph Weissleder has been my role model in pursuing highest quality research. I have benefited greatly from learning his way of scientific thinking, especially on the profound questions intersecting biology, engineering, and chemistry. I am also grateful for his trust in my ability to pursue my own research area of interest, and for his guidance in applying my work to the very important development in healthcare and technology.

Dr. Robert Westervelt has given me crucial support through my PhD. He has guided me in making many important decisions during this process, from choosing research areas and topics at the very beginning to thinking about post-PhD career plan. I feel very grateful for his constructive feedbacks on my work, his contributions of novel ideas to my research, and for his understanding and patience when guiding me in challenging situations. He is also a mentor with much wisdom and a great sense of humor. From many enjoyable conversations with him, I learned not only the essence of scientific thinking, but also new ways to view life outside of science.

Dr. Hakho Lee has given me a tremendous amount of guidance during my PhD. He has devoted countless hours to teach and mentor me. It is from him that I have learned how to be

rigorous, creative, and practical in research. His deep passion in science and medicine has been a great inspiration to me throughout my PhD. For example, despite of his many other research duties, he worked side-by-side with me at Harvard machine shop and taught me the art of machining. In addition, he has provided me with many rich learning experiences including the weekly journal clubs, trips to national conferences, and informal lunch discussions at the navy yard cafe. I am so grateful to have him as an extremely intelligent yet modest, demanding yet kind-hearted mentor.

I also want to thank all my colleagues at Weissleder Group for their support. Dr. Hyungsoon Im has taught me many things in optics; Dr. Kyunghoon Lee gave me a lot of guidance in microfluidics; Dr. David Issadore and Dr. Jaehoon Chung trained me in microfabrication from the very basics to advanced techniques. I also learned new knowledge from discussing and collaborating with Dr. Sangmoo Jeong, Dr. Huilin Shao, Dr. Anna Turetsky, Dr. Eunha Kim, Dr. Yongil Park, Changwook Min, Dr. Christine Swisher, and Liubov Fexon. I am grateful for having the opportunity to work with these outstanding researchers. Moreover, they also made it fun to be working in this lab.

I would like to thank the supportive faculties and staff at Harvard School of Engineering and Applied Sciences. c. Michael Brenner, Prof. Neel Joshi and Prof. Vinodhan Manoharan have kindly devoted their time and helped me with my dissertation and academic pursuit. The staff in SEAS student affairs office also provided great support during my time in the department.

I also feel very lucky to have many friends who stayed by my side through this journey. I thank George, Jun, Xiaodan, Zhenghan, Chenhui, Yakun, and Yingying for lightening my life outside of lab. They made me laugh even during stressful times.

Last but not least, I thank my incredibly supportive parents. Without their understanding, unconditional support and sacrifices, it would not be possible for me to study in the US and pursue my passion in science and engineering.

# List of Figures

Figure 2.1. Digital diffraction diagnosis (D3) platform.	11
Figure 2.2. Implemented digital diffraction diagnostic (D3) platforms.	12
Figure 2.3. Real-time reconstruction and counting process.	15
Figure 2.4. Principle of counting algorithm.	17
Figure 2.5. Optimization of microbead size for cell labeling.	21
Figure 2.6. High-throughput cell and bead identification.	23
Figure 2.7. Reconstructed images of microbeads.	24
Figure 2.8. Reconstructed images of leukocytes.	25
Figure 2.9. Detecting cancer cell markers with immunobead labeling.	27
Figure 2.10. Cancer cells labeled with different numbers of microbeads.	28
Figure 2.11. Molecular profiling of A431 cancer cells.	29
Figure 3.1 Schematics of LDIH device.	36
Figure 3.2. Block diagram of compressive LDIH (cLDIH) algorithm.	39
Figure 3.3. An example of compressive LDIH (cLDIH) reconstruction.	40
Figure 3.4. Resolution of cLDIH for various detector pixel sizes.	42
Figure 3.5. Reconstruction of sub-pixel patterns using cLDIH.	45
Figure 3.6. Reconstruction of patterns with phase contrast using CLDIH.	46
Figure 4.1. Summary of lymphoma detection and analysis scheme.	54
Figure 4.2. Photograph and schematics of lymphocyte capture chip.	55
Figure 4.3. Fluidic structures in microfluidic chip.	56
Figure 4.4. Validation of on-chip capture and imaging.	57
Figure 4.5. Capture efficiency characterization.	59
Figure 4.6. Flow rate optimization.	61
Figure 4.7. Antibody validation and cell line profiling by flow cytometry.	63
Figure 4.8. Imaging strategy for clinical diagnosis	65
Figure 4.9. Sample image analysis using an in-house image processing algorithm.	68
Figure 4.10. On-Chip Imaging.	70
Figure 4.11. Cell profiling for kappa/lambda monoclonality by image analysis.	73
Figure 4.12. On-chip drug testing.	75

Figure 5.1. Schematics of chessboard type magnetic-microfluidic cell sorter.	82
Figure 5.2. Top view of microfluidic channel.	83
Figure 5.3. Cross section view of system.	84
Figure 5.4. Configuration of magnet arrays in simulation.	85
Figure 5.5. Magnetic field distribution along z-direction (from bottom to top array).	87
Figure 5.6. Cross section view of magnetic field strength.	88
Figure 5.7. Comparison of magnetic force (chessboard vs uniform).	90
Figure 5.8. Enrichment ratio test using microbeads.	93
Figure 5.9. Representative images at inlet and outlet from enrichment ratio test.	94
Figure 5.10. Enrichment ratio of the system from bead sorting test.	95
Figure 5.11. Schematics of cell sorting and capture experiment.	97
Figure 5.12. Images of cell capture zone from blood sample tests.	98

## List of Tables

Table 2.1. D3 assay configurations for different detection targets.	8
Table 4.1. Cell Counts in Cerebral Spinal Fluid	50
Table 4.2. Antibodies for On-chip Imaging.	71

# Chapter 1 Introduction

*Point-of-Care (POC) Testing: Medical care testing at or near the site of patient care.*

## 1.1. Motivation

### 1.1.1. Point-of-Care (POC) diagnostic system

Providing quality healthcare to people in low-income countries or resource limited areas remains a major global challenge. Diseases such as tuberculosis and meningitis are still prevalent in many regions over the world. One reason behind is that most diagnostic tools can only be afforded or operated in well-funded hospitals or laboratories. Patients without access to these facilities or those in resource-limited regions have to suffer from late or inaccurate diagnosis, which severely lowers their chances of being cured. {Yager et al., 2008, #57872; Mabey et al., 2004, #51751}

One promising solution to this problem is to develop point-of-care (POC) test systems, which can provide low cost, miniaturized system size and integration of complex diagnostic functions. Many POC systems have been advanced in recent years and been shown as promising diagnostic tools for developing countries and low-income regions {Yager et al., 2006, #66170; Chin et al., 2007, #8508}. These systems include holographic imaging, microfluidic sorting, surface plasmon resonance, electrical impedance, magnetometry, nuclear magnetic relaxometry and more {Myers and Lee, 2008, #2685; Castro et al., 2014, #42059; Chung et al., 2013, #6542; Im et al., 2014, #68496; Issadore et al., 2012, #19027; Issadore et al., 2014, #86766; Peterson et al., 2013, #350; Ullal et al., 2014, #18788; Chan et al., 2013, #66131; Haun et al., 2011, #29551;

Lee et al., 2008, #38056; Lee et al., 2008, #14988; Nagrath et al., 2007, #54886; Sun et al., 2007, #18617; Bishara et al., 2011, #126}.

Despite the success of these recent developments, there are still unmet needs in realizing cost-effective, fast and accurate POC diagnosis routines. This thesis hence focuses on the further development of POC systems to meet these needs, especially in detecting and profiling scant cells in blood.

### **1.1.2. POC Systems for Cellular analysis**

Two tasks are crucial in the process of POC testing. The first is to isolate the cells of interests for analysis. This task can be extremely challenging for cells of low abundance in blood and other bodily fluids. One example of such low abundance cells is circulating tumor cells (CTC). These cells are shed from primary tumor and circulate in the blood stream. CTCs have been shown as promising non-invasive measure of cancer progression{Cristofanilli et al., 2004, #6958; Maheswaran et al., 2008, #90478}. Despite their clinical importance, the concentration of CTC is extremely low, ranging from 1 to 10 cells in every mL in blood. Finding and isolating these cells from other cell populations can be as difficult as finding needles in a haystack.

The second task is to profile cells in respect to protein expression, which provides important information about the related disease{Basik et al., 2013, #37148}. For example, the protein expression of CTC cells can indicate the progression, treatment response, and overall survival of the cancer{Cristofanilli et al., 2004, #6958; Maheswaran et al., 2008, #90478}. Currently cellular profiling is usually performed using flow cytometry or fluorescence microscope. These tools are often bulky and expensive, which limits their use outside of well-



equipped laboratories. Moreover, these tools are low in throughput and thus cannot provide fast screening for a large population of patients in a short time frame.

Given the significance of cell sorting and profiling, this thesis focuses on the development POC systems that can perform these tasks in a cost effective and high efficiency manner.

### **1.1.3. Optical POC Systems**

Microscope is the most widely used diagnostic tools for numerous diseases. With the development of fluorescent techniques, modern microscopy also offers the capability of cell profiling. However, conventional microscopy cannot be easily adapted for POC uses because of its bulky and expensive optics, as well as its requirement for trained microscopists.

With the fast development of digital sensors and computational tools, new microscopy techniques have been introduced in recent years. Digital holography, in particular, has emerged as one promising alternative to conventional microscopy {Garcia-Sucerquia et al., 2006, #85554; Greenbaum et al., 2013, #29283; Lee et al., 2011, #28843; Mudanyali et al., 2011, #36359; Seo et al., 2010, #24199; Su et al., 2013, #64959; Zheng et al., 2013, #82582}. Utilizing the rich information from optical diffraction, it becomes possible to achieve the similar imaging resolution as in a conventional microscopy.

Lens-free holography was first developed by Kreuzer's group {Xu et al., 2001, #53324}, followed by various systems {Garcia-Sucerquia et al., 2006, #85554; Greenbaum et al., 2012, #78517; Gurkan et al., 2011, #36369; Kim et al., 2011, #51285; Zheng et al., 2011, #96855}. Most of recently developed systems have been relying on morphology for target

recognition {Garcia-Sucerquia et al., 2006, #85554; Greenbaum et al., 2013, #29283; Lee et al., 2011, #28843; Mudanyali et al., 2011, #36359; Seo et al., 2010, #24199; Su et al., 2013, #64959; Zheng et al., 2013, #82582}. Although morphology can sometimes be sufficient for target cell detection, it omits the molecular information carried by cells, and thus is not adequate for accurate diagnostics of most diseases {Ojesina et al., 2014, #81013} {Schiffman and Solomon, 2013, #73415}.

In order to successfully apply lens-free holography technology to POC diagnostics, new detection strategy is needed to accurately perform cellular profiling.

#### **1.1.4. Microfluidic POC System**

Many different types of microfluidic systems have been developed to address the challenge in POC tests {Chin et al., 2007, #8508; Myers and Lee, 2008, #2685; Yager et al., 2006, #66170} {Gubala et al., 2012, #87653}. These platform includes blood glucose test, CD4+ T-cell counters for monitoring HIV, bacteria detection for malaria, etc {Chin et al., 2012, #889} {Gubala et al., 2012, #87653}.

We have adopted microfluidic systems for the purpose of cancer detection in clinical samples. One example is the detection of central nervous system (CNS) lymphoma, which requires clonal analysis of lymphoma cells in the cerebral spinal fluid (CSF). Currently, the clinical diagnosis of CNS lymphoma still relies on conventional cytopathology of CSF or MRI. Because lymphoma cells are in low abundance in the CSF, POC system capable of capturing them individually and performing on-chip profiling is needed.

Another bottleneck for POC cancer diagnostics lies in extracting rare cells from blood or other fluid samples. CTCs have been shown as a promising non-invasive biomarker for cancer diagnosis and treatment monitoring {Cristofanilli et al., 2004, #71167; Gottlieb et al., 1981, #79461}. However, their low abundance in blood make it difficult to separate them from the complex background of other cell populations. Therefore high-efficiency cell sorting mechanism is needed to meet this needs.

## **1.2. Thesis organization**

This thesis introduces novel optical and microfluidic POC systems for cellular analysis. Chapter 2 and 3 focus on optical imaging diagnostic systems, and Chapter 4 and 5 focus on microfluidic systems. First, Chapter 2 describes a new lens-free holographic imaging system for cell detection and profiling. Chapter 3 introduces a novel resolution enhancement method for lens-free in-line holography using compressive sensing. Chapter 4 describes a high-throughput single-cell capturing system for lymphoma detection in CSF. And lastly, Chapter 5 details a magnetic-microfluidic system for the isolation of low abundant cells in blood.

# Chapter 2 Digital In-line Holography for Point-of-Care

## Diagnostics

### 2.1. Background

#### 2.1.1. POC Imaging System

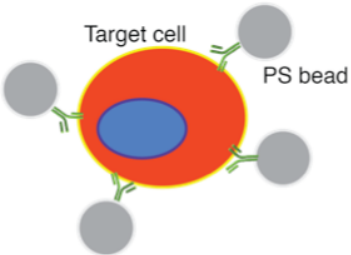

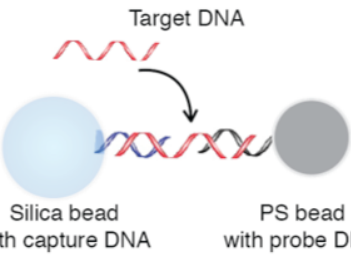

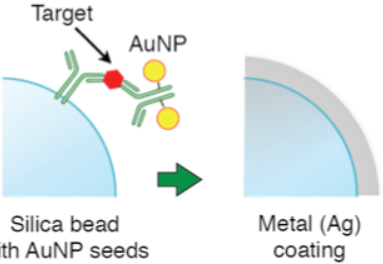
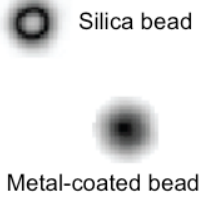
The rapid dissemination of electronic communication devices such as smartphones, tablets and wearable electronics, all with integrated sensors, creates new possibilities for inexpensive point-of-care (POC) diagnostics and care delivery. One example is detecting cancer in low- and middle-income countries where limited resources and geographical constraints often lead to missed opportunities for intervention, resulting in mortalities even in treatable cancers{Varmus and Trimble, 2011, #76720}. Current efforts to control cancer thus focus on implementing population-based early screening programs; a key element for success is a cost-effective, robust diagnostic platform that can be readily deployed into POC settings{Chin et al., 2012, #45171}. While conventional microscopy of human samples (smears, aspirates, biopsies, blood) is the most widely used to diagnose cancer, its POC adaptation is limited by inherent drawbacks such as bulky optics, requirements for trained microscopists and operator-dependent variability.

#### 2.1.2. Digital In-line Holography

Lens-free Digital In-line Holography (LDIH) has been recently developed as a promising tool for portable microscopy. Compared to traditional microscopy, LDIH allows compact and

easy setup, with no intermediate optical components between sample and imaging sensor. LDIH systems can achieve low cost, large field-of-view (FOV) and three dimensional reconstruction. {Greenbaum et al., 2012, #2354} {Jericho and Jürgen, 2011, #17612} {Garcia-Sucerquia et al., 2008, #51555} {Lee et al., 2012, #2412; Lewis et al., 2006, #18978; Mudanyali et al., 2010, #23835; Mudanyali et al., 2009, #67598; Seo et al., 2009, #36409}. Recent applications of the LDIH technique has shown its clinical and biomedical potential in the detection and visualization of cells such as bacteria, blood cells, and large organelles (e.g., *C. elegans*, plankton) . {Coskun et al., 2010, #29609; Garcia-Sucerquia et al., 2008, #51555; Greenbaum et al., 2012, #2354; Isikman et al., 2010, #29258; Jericho and Jürgen, 2011, #87140; Mudanyali et al., 2010, #23835; Seo et al., 2009, #36409; Zheng et al., 2010, #73017; Guoan Zheng et al., 2011, #63857}.

Here we describe a new approach of LDIH, termed digital diffraction diagnostics (D3), based on the computational analysis of distinct diffraction patterns generated by microbeads that bind to biological targets of interests. The strategy can detect broad range of targets (Table 1.1): soluble proteins, nucleic acids or cellular proteins. We tested the approach by first exploring cancer cell profiling with immunomicrobeads. Diffraction patterns generated by microbeads were detected by a smartphone camera, and digital processing reconstructed images of bead-bound cells to retrieve molecular information. To provide effective POC operation at remote sites, we further adopted a client-server model: the data acquired by a smartphone were digitally processed by a remote parallel-computing server. By optimizing the assay protocol and the computational algorithm, we achieved real-time molecular analyses on  $>10^6$  cells. The D3 assay was simple and fast ( $< 45$  min for the entire assay including immunolabeling or  $< 3$  min for data analysis), requiring minimal sample preparation.

Targets	Assay type	Optical signature
Cell	 <p>Target cell PS bead</p>	 <p>Beads bound to cells</p>
Nucleic acid	 <p>Target DNA Silica bead with capture DNA PS bead with probe DNA</p>	 <p>Formation of PS-silica dimers</p>
Protein	 <p>Target AuNP Silica bead with AuNP seeds Metal (Ag) coating</p>	 <p>Silica bead Metal-coated bead Changes in transmittance</p>

**Table 2.1. D3 assay configurations for different detection targets.**

For cells, immunomicrobeads in different sizes and optical transmittance bind to specific markers on extracellular membranes. For nucleic acids, two different types of microbeads, coated with oligonucleotides complementary to each side of target DNA, dimerize. For proteins, a sandwich assay with affinity ligands (e.g. peptide, antibodies) is used to coat the silica microbead surface with Au nanoparticles, subsequently converted to a metallic film. The changes in light transmittance of metal-coated silica beads are detected by the D3 platform.

## 2.2. Methods

### 2.2.1. Digital Diffraction Diagnostics (D3) Platform

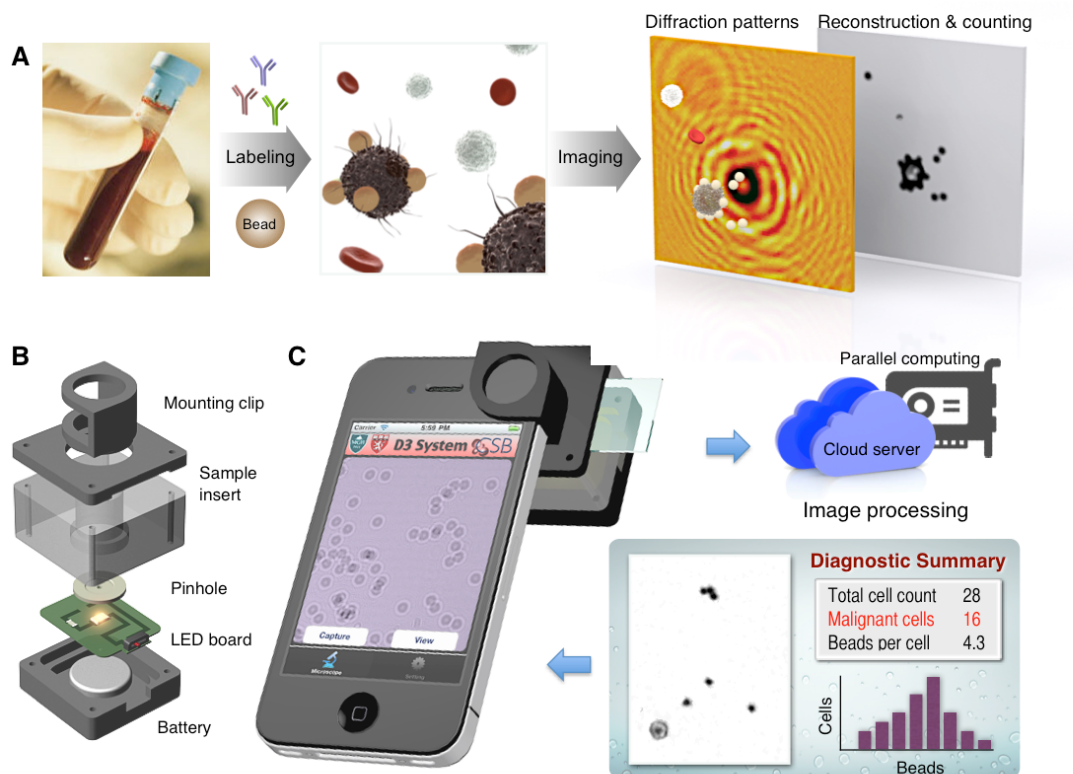
The D3 assay for cell detection is illustrated in Figure 2.1A. Specimens are obtained from minimally invasive procedures (e.g., smears, brushings, fine needle aspiration, blood draw), and cells are molecular-specifically labeled with microbeads. Labeled samples are placed directly on the imaging device. Interference patterns between scattered light from the specimen and the reference light are recorded {Fung et al., 2011, #27933; Mudanyali et al., 2010, #7741}. Digital signal processing then recovers and analyzes object images. Because individual cells are spatially resolved and only target cell-associated beads are counted, there is no need for washing steps, which simplifies the assays. Selective microbead binding is critical to distinguishing target cells from other host cells and quantitatively profiling protein markers per cell.

To perform the D3 assay in POC settings, we implemented a portable sensing terminal that utilizes the embedded optics and communication functions of a smartphone (Figure 2.1B). We constructed a snap-on module, which contained a light source and a sample insert, to be mounted on a phone camera. The acquired diffraction patterns were transferred to a dedicated server for post-processing (figure 2.1C). Following this step, the analytical readouts (e.g., target cell counts, bead counts per cell) and reconstructed images were sent back to the smartphone for display. This scheme frees the sensing terminals from heavy computation load, thereby making their implementation simple and cost-effective. All data were communicated through a secure cloud service, and we programmed a user-friendly interface to streamline the process.

Alternatively, a miniaturized image sensor connected to a local computer can also be used (Figure 2.2).

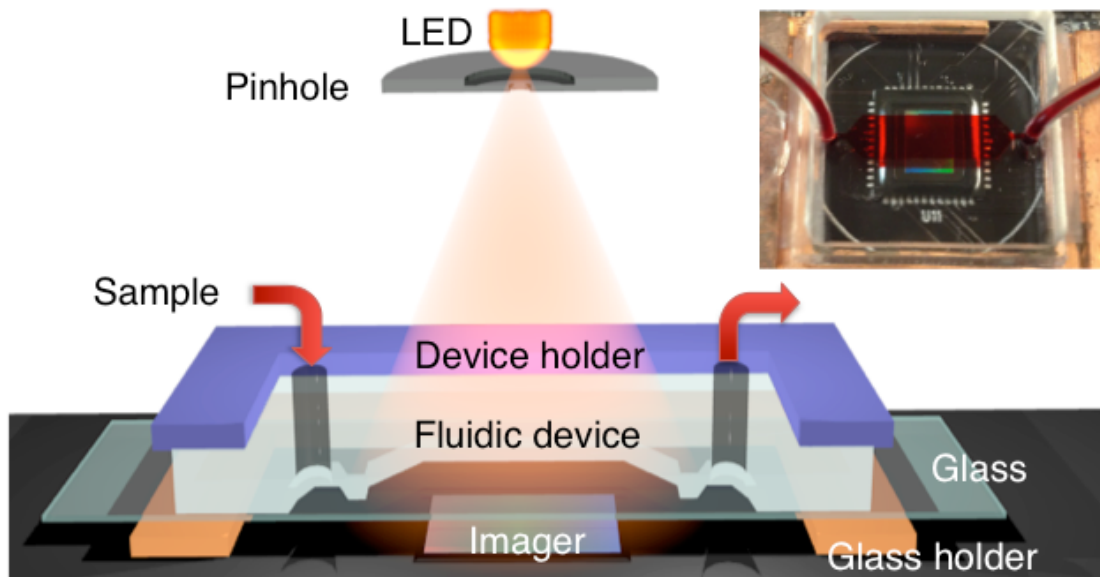
Electrical components (e.g., light emitting diode, battery socket, switch) were purchased (Digi-Key) and mounted on a custom-designed printed circuit board. The main body of the snap-on module was machined on black acrylic plastic, and the light source (590 nm) and a 100  $\mu\text{m}$  pin-hole were housed inside. The size of the snap-on was  $4 \times 4 \times 5.5 \text{ cm}^3$ .





**Figure 2.1. Digital diffraction diagnosis (D3) platform.**

(A) Assay schematic for cellular detection. Target cells in patient samples (e.g., blood or biopsy) are immuno-labeled with microbeads, and their diffraction patterns are recorded. The diffraction images are then digitally reconstructed into object images wherein bead-labeled target cells are identified. For the detection of other types of targets, see table 2.1. (B) The snap-on module for a smartphone consists of a light-emitting diode (LED) powered by a coin battery, a pinhole for uniform illumination with partial coherence and a sample mount. (C) The D3-mounted smartphone's embedded phone camera is used to record the diffraction images of the specimen. The recorded images are transferred to a server via the cloud service for real-time image reconstruction and analyses, which can be returned to the smartphone in less than 1-2 min.



**Figure 2.2. Implemented digital diffraction diagnostic (D3) platforms.**

Imager IC (integrated circuit)-based system. The device combined the D3 with microfluidics to provide high throughput, in-flow measurements. The fluidic device was bonded to a glass coverslip (thickness, 160  $\mu\text{m}$ ), and placed right above the imager. (Inset) Samples were delivered to the imaging area through a microfluidic channel.

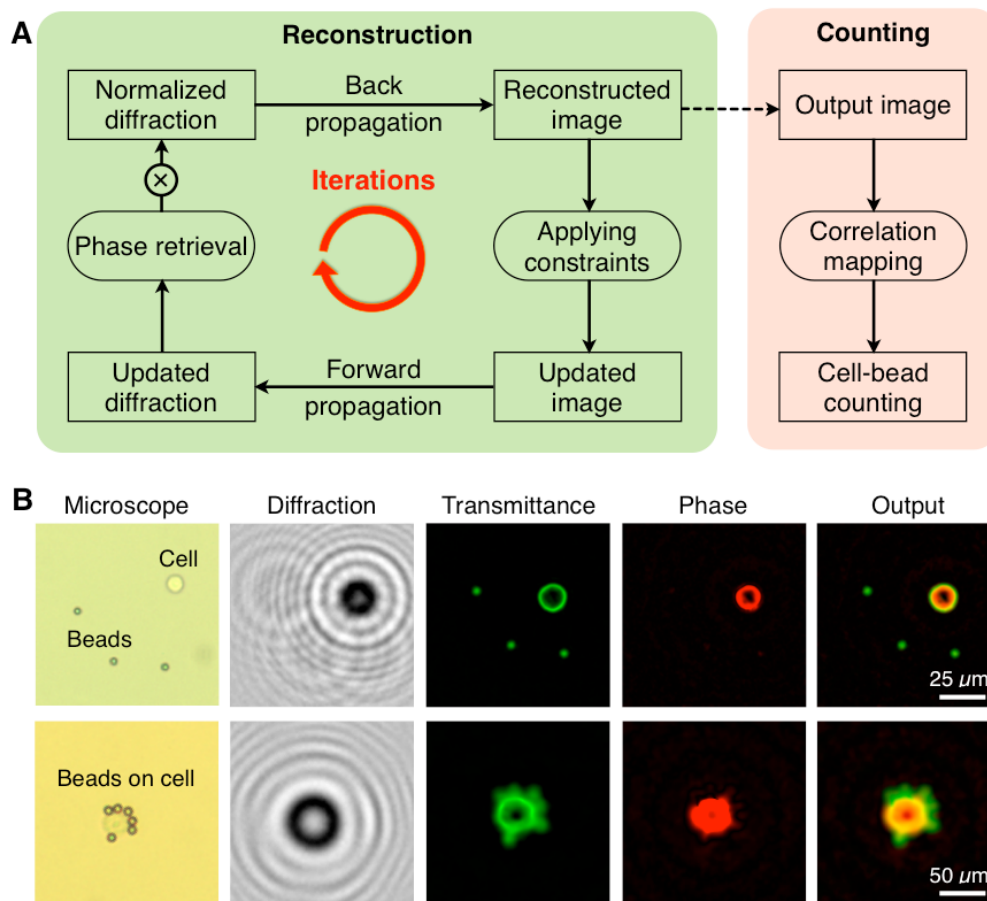
### 2.2.2. Reconstruction and Counting Algorithm

To accurately detect bead-bound target cells, we formulated a new processing algorithm for image reconstruction and post-analysis (Figure 2.3A). The reconstruction was based on the Rayleigh-Sommerfeld diffraction principle but was extended to digitally retrieve both transmittance and phase shift of objects through an iterative optimization {Fienup, 1982, #63988; Kreis, 2002, #60650; Latychevskaia and Fink, 2007, #63427}. In each iteration, the routine applied physical constraints (i.e., light transmittance and object supports) to a reconstructed object image and updated the corresponding diffraction patterns with retrieved phase information. The method restored high phase-contrast between cells and microbeads (Figure 2.3B).

The size of an uncompressed raw image file on the iPhone 4S was ~24 megabytes (2448 × 3264 pixels, 24-bit RGB). This raw image file was converted to gray-scale PNG (~2.7 megabytes) or JPEG (~0.4 megabytes) files, and normalized by a reference image recorded without samples.

The normalization removed intrinsic defects and accurately calculated object transmittance {Latychevskaia and Fink, 2007, #63427}. The normalized diffraction images were up-sampled 4 times through cubic interpolation and used as input data for reconstruction. The reconstruction was based on phase retrieval algorithms, which can recover phase information from intensity-based diffraction patterns through iterative processes {Fienup, 1982, #63988; Garcia-Sucerquia et al., 2006, #85555; Mudanyali et al., 2010, #7741}. As shown in Figure 2.3A, the algorithm has 4 steps: 1) back-propagate an input image, 2) apply constraints, 3) forward-propagate updated image and 4) update retrieved phase information. First, the

normalized diffraction image was numerically back-propagated by an optical distance between the object and the imager. We calculated the optimal optical distance by finding a focal depth with the sharpest object boundary{McElhinney et al., 2007, #55580}. Calculating field propagation was based on the Rayleigh-Sommerfeld diffraction integral in a convolution approach, where the propagated field was calculated by the inverse Fourier transform of the multiplication between the Fourier transform of field and the transfer function{Kreis, 2002, #60650}. During the first iteration, object supports were defined using a segmentation method, where object boundaries were found by thresholding intensity variances{McElhinney et al., 2007, #55580}. For the back-propagated image, pixels outside the object supports were regarded as background, and their transmittance values (i.e., the modulus of field) were set to unity. If a pixel inside the object support had a transmittance value larger than unity due to artificial twin image superimposition, its transmittance value was also forced to unity. After applying the constraints, the updated image was propagated to the image plane, where the forward-propagated field had non-zero phase information. The phase information was added to the measured diffraction image as a new input. The process was usually repeated by 10 ~ 30 times until the reconstructed image with retrieved phase information converged.



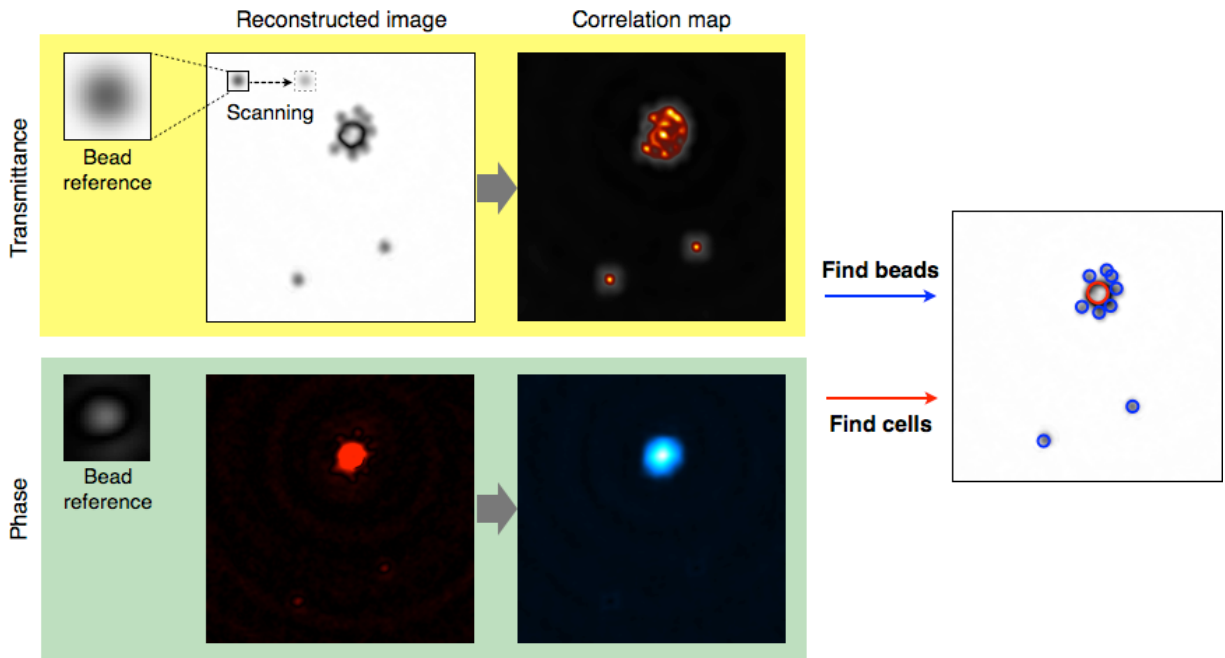
**Figure 2.3. Real-time reconstruction and counting process.**

(A) Diagram of reconstruction and counting algorithm. A diffraction image, normalized by a reference image obtained in the absence of specimens, is reconstructed through an iterative process. Following the image reconstruction, cells and beads are detected using a counting algorithm, which scanned a reference image of a microbead over the reconstructed image. (B) Examples of the image reconstruction. Raw diffraction patterns of cancer cells and 7- $\mu\text{m}$  microbeads show undecipherable patterns. The reconstruction algorithm recovers both transmittance and phase information. Cells and microbeads can be differentiated from their high phase contrast. The bead-bound cells are automatically identified, and the bead numbers are counted. The transmittance (green) and phase contrast (red) images are pseudo-colored to better visualize optical properties of cells and beads.

### **2.2.3. Target Cell Detection**

Following reconstruction, images were processed by the detection routine. The algorithm generated transmittance and phase correlation maps by scanning a microbead reference image over the reconstructed images (Figure 2.4). The reference microbead image was obtained by averaging microbead images in a pure bead solution. The correlation coefficients for modulus and phase were calculated from pixel-to-pixel comparison between reference and reconstructed images. Cells and microbeads could be differentiated from the transmittance and phase correlations, respectively. Subsequently, cells labeled with microbeads were automatically identified, and their individual bead counts were recorded.

Cells were first detected when a local maximum phase correlation coefficient was larger than the threshold value of phase correlation coefficient, which was obtained from images of pure cell population. For each cell detected, microbeads within the object support were detected from the local maxima of the modulus correlation coefficients. To distinguish microbeads from cells in similar sizes (e.g. white blood cells, macrophages), the phase and phase correlation coefficients were also considered and should be smaller than bead threshold values.



**Figure 2.4. Principle of counting algorithm.**

Cells and beads are detected based on transmittance and phase correlation maps. The transmittance correlation map is generated by scanning the transmittance of a reference bead over that of a reconstructed image (top). The phase correlation map is generated in a similar manner using phase information (bottom). The beads are identified in the transmittance correlation map, whereas the cells are detected in the phase correlation map.

#### 2.2.4. D3 App and GPU Server

The D3 App was programmed with user-friendly interfaces for operation in iOS 6 or higher version. The App has three main screens: 1) image capturing and processing, 2) reconstruction parameters settings and 3) data communication with a cloud service. The images captured by a phone camera module were saved as raw data (TIFF, PNG) or compressed image (JPEG) and uploaded along with other imaging information (e.g., wavelength, diagnosis location, time, patient data) into a dedicated folder in a cloud storage (Dropbox). The uploaded images were processed by a D3 image GPU server (see below), and the results were saved into a subfolder. The D3 App subsequently downloaded reconstructed images and analysis results. All data was encrypted according to the 256-bit Advanced Encryption Standard (AES). The application program interface (API) library from the vendor (Dropbox) was used to implement the data transfer routine.

To accelerate imaging analyses, we used a server equipped with a graphic processing unit (GPU) containing a large number of core processors. The program codes were optimized to execute massively parallel image processing threads (e.g., > 5000) in a GPU, which permitted near instantaneous image reconstruction and post-analyses. For instance, using a 448-core GPU, a 16-bit  $1024 \times 1024$  diffraction images could be analyzed within 90 msec, ~3000-fold faster than a conventional computer (4-core 2.4 GHz central processing unit).

The D3 server (HP xw4600 workstation, Hewlett Packard) had the following system specifications: CPU, Core2 Duo E8500 3.16 GHz (Intel); memory, 8 gigabyte DDR2 (double data rate2); GPU, Tesla C-2070 (Nvidia); operating system, Ubuntu 12.04 64-bit. The GPU had 448 CUDA (Compute Unified Device Architecture) cores and 6 gigabyte memory. The signal



processing program was written in C++ language and used vendor-provided modules (CUDA extensions, CUDA driver 5.0, CUFFT library). The imaging server polled a dedicated folder in a cloud storage (Dropbox). When new images and image information were uploaded, the imaging server executed image reconstruction and post imaging analyses (cell and bead counting). The reconstructed images and counting statistics were then saved into a subfolder. When synchronized in the cloud storage, the image and data files could be accessed by users.

### **2.2.5. Cell Labeling Strategy**

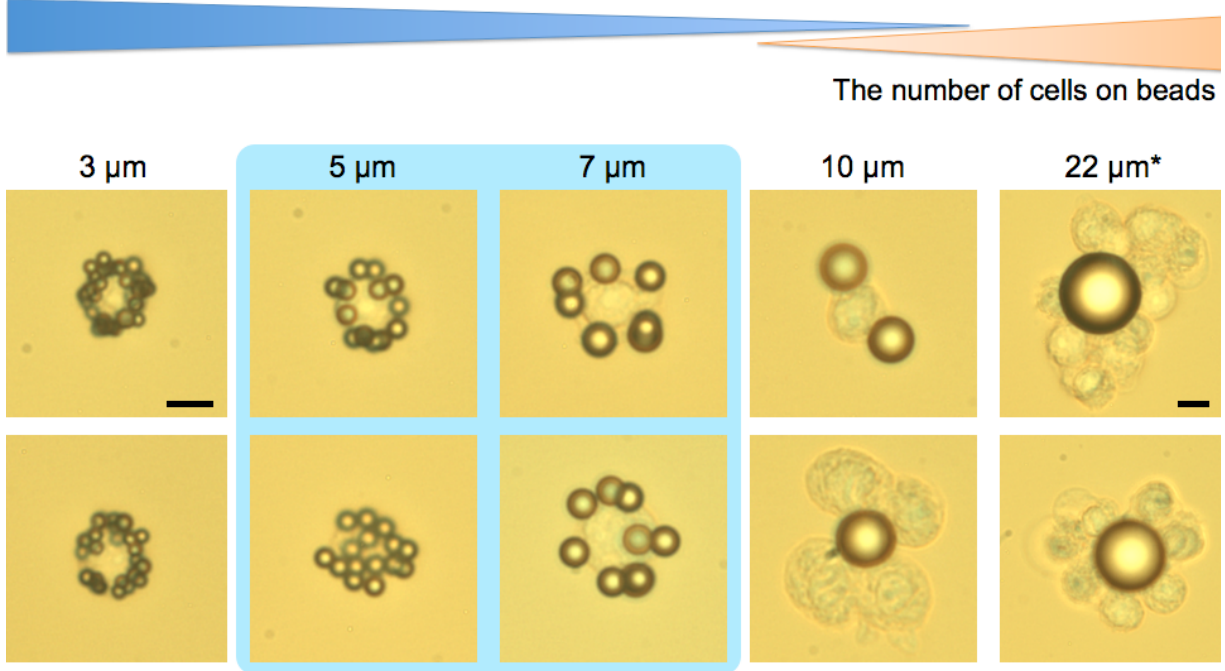
New cell labeling strategy is needed in the D3 assay for cell profiling. Human cancer cell lines were immunolabeled with microbeads to generate specific diffraction signatures. While it is possible to use antibody-coated microbeads directly on cells, we found that a two-step approach increased bead-binding{Agasti et al., 2012, #40836}. We thus opted for highly efficient bioorthogonal (e.g., between trans-cyclooctene and tetrazine{Haun et al., 2010, #21127}) or a streptavidin/biotin approaches. For example, using the latter, cells were first targeted by biotinylated antibodies and subsequently incubated with streptavidin-coated microbeads. We further tested commercially available microbeads in different sizes (diameter, 3 – 22  $\mu\text{m}$ ). A bead diameter between 5 – 7  $\mu\text{m}$  was found to optimize accurate bead-counting while minimizing cell clustering (Figure 2.5).

In a typical labeling experiment,  $10^5$  cells were labeled with biotinylated anti-HER2, anti-EpCAM or anti-EGFR (2  $\mu\text{g}/\text{mL}$ , 8 biotin molecules/antibody) and streptavidin-coated polystyrene particles (0.5 mg, 6.7  $\mu\text{m}$  diameter, Spherotech), each for 10 min at room temperature. Leukocytes were prepared from 0.6 ml blood samples mixed with 12 mL BD

Phosflow Lyse/Fix buffer (1×) for 15 min at 37 °C. The cells were resuspended in 1× PBS containing 2% serum and 1% BSA (PBS+).

SkBr3 and A431 human cancer cells were cultured in DMEM medium and supplemented with fetal bovine serum (10%), penicillin and streptomycin (1%) and L-glutamine (1%). Cell lines were maintained at 37°C in a humidified atmosphere containing 5% CO<sub>2</sub>. At confluence, the cells were washed, trypsinized and resuspended in 1× phosphate buffer saline (PBS) containing 2% fetal bovine serum and 1% BSA (PBS+).

The number of beads on cells



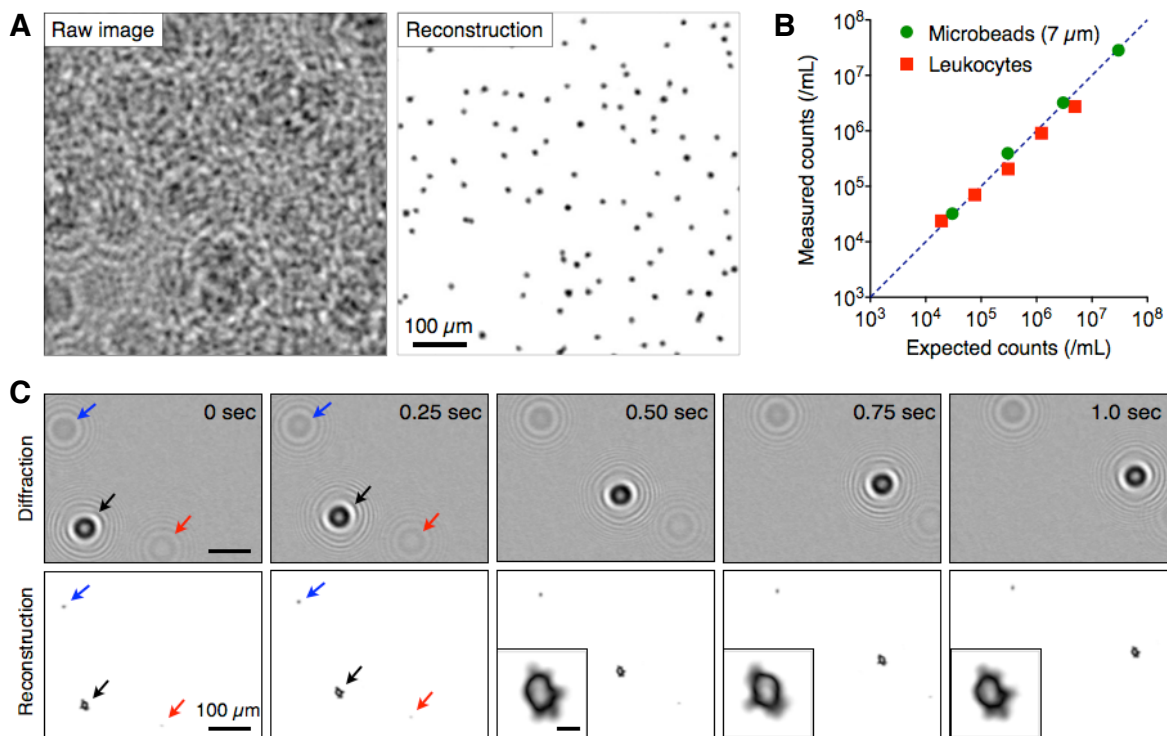
**Figure 2.5. Optimization of microbead size for cell labeling.**

Microscope images of cancer cells labeled with differently sized microbeads. The number of beads bound to cells decreased with the bead diameter up to 10  $\mu\text{m}$ . When the diameter was  $>10$   $\mu\text{m}$ , multiple cells were aggregated around a single microbead. The micrographs for 22- $\mu\text{m}$  beads are down-scaled by 70%. Scale bar, 10  $\mu\text{m}$ .

## 2.3. Demonstration

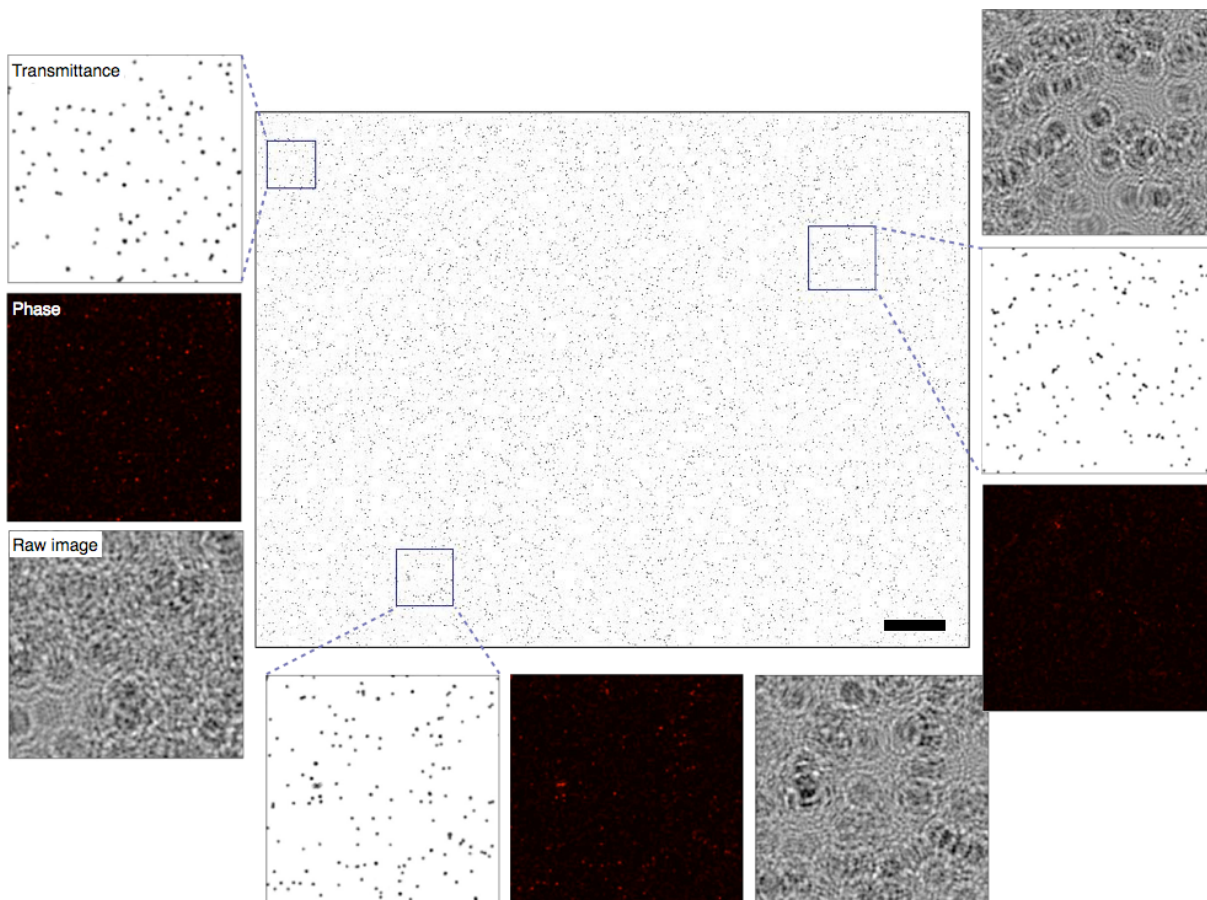
### 2.3.1. Reconstruction and Cell Detection

With its large field-of-view and rapid image processing, the D3 platform enabled high throughput cellular analyses. In a single image acquisition, more than 10000 objects could be detected at microscopic resolution (Figure 2.6A, Figure 2.7). The dynamic range of detection spanned over 3 orders of magnitude (Figure 2.6B), with the object concentration reaching up to  $\sim 10^7$  microbeads or cells per milliliter of sample (Figure 2.7 and 2.8). The capacity for high density imaging, combined with the recognition of bead-bound cells, made it possible to detect target cells in the presence of abundant host cells (e.g., leukocytes) and unbound microbeads, which eliminated the need for external washing and purification steps. The assay throughput could be further increased by flowing target cells through a microfluidic channel and performing real-time ( $>10$  full-frames/sec) D3 assay (Figure 2.6C). This is akin to a flow cytometer with imaging capabilities for quantitative analysis{Basiji et al., 2007, #14844}, but in a miniaturized system.



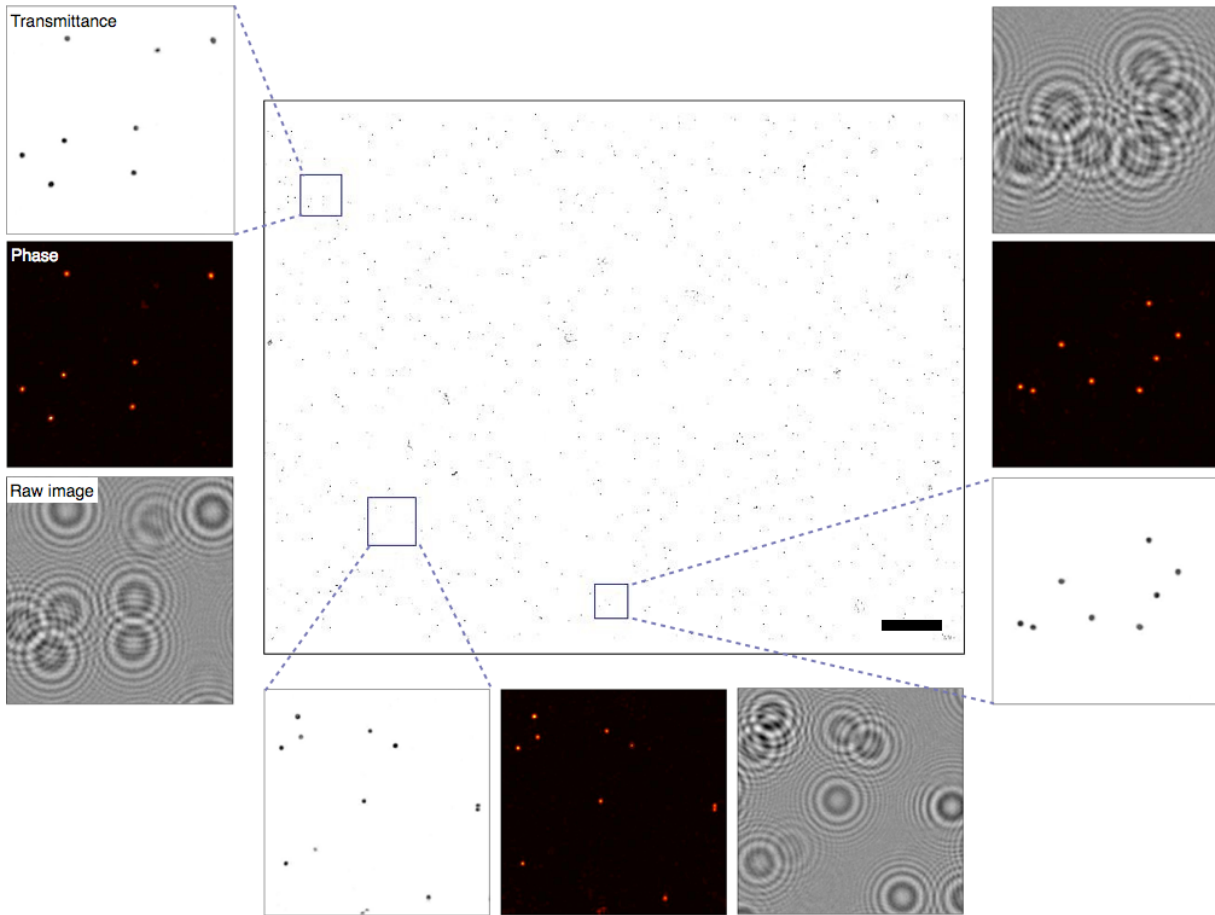
**Figure 2.6. High-throughput cell and bead identification.**

(A) Diffraction and reconstructed images of 7  $\mu\text{m}$  microbeads at a concentration of  $5 \times 10^7$  beads/mL. More than  $10^5$  objects can be detected at microscopic resolution from a single imaging. (B) Comparison between the D3-counted microbeads and leukocytes and their expected counts. Note the linearity ( $R^2 > 0.97$ ) even at very high bead concentration ( $5 \times 10^7$  beads/mL); also, the leukocyte concentration ( $5 \times 10^6$  cells/mL) is comparable to that in whole blood. (C) Temporal image reconstruction of cells in flow. Diffraction images were recorded at 4 frames/sec and reconstructed in real time by the D3 server. A bead-labeled cancer cell (black arrow), a non-targeted cell (blue) and a free-floating microbead (red) are automatically identified. The inset shows high resolution details of the bead-labeled cell undergoing rotational motion in the flow stream.



**Figure 2.7. Reconstructed images of microbeads.**

Polystyrene microbeads (diameter, 7  $\mu\text{m}$ ) were imaged at high concentrations ( $\sim 3 \times 10^7$  beads/mL) in the field-of-view of 24  $\text{mm}^2$ . Reconstructed amplitude, phase and raw diffraction images are shown for three selected spots. Note that microbeads are highly visible only in transmittance images. Scale bar, 500  $\mu\text{m}$ .



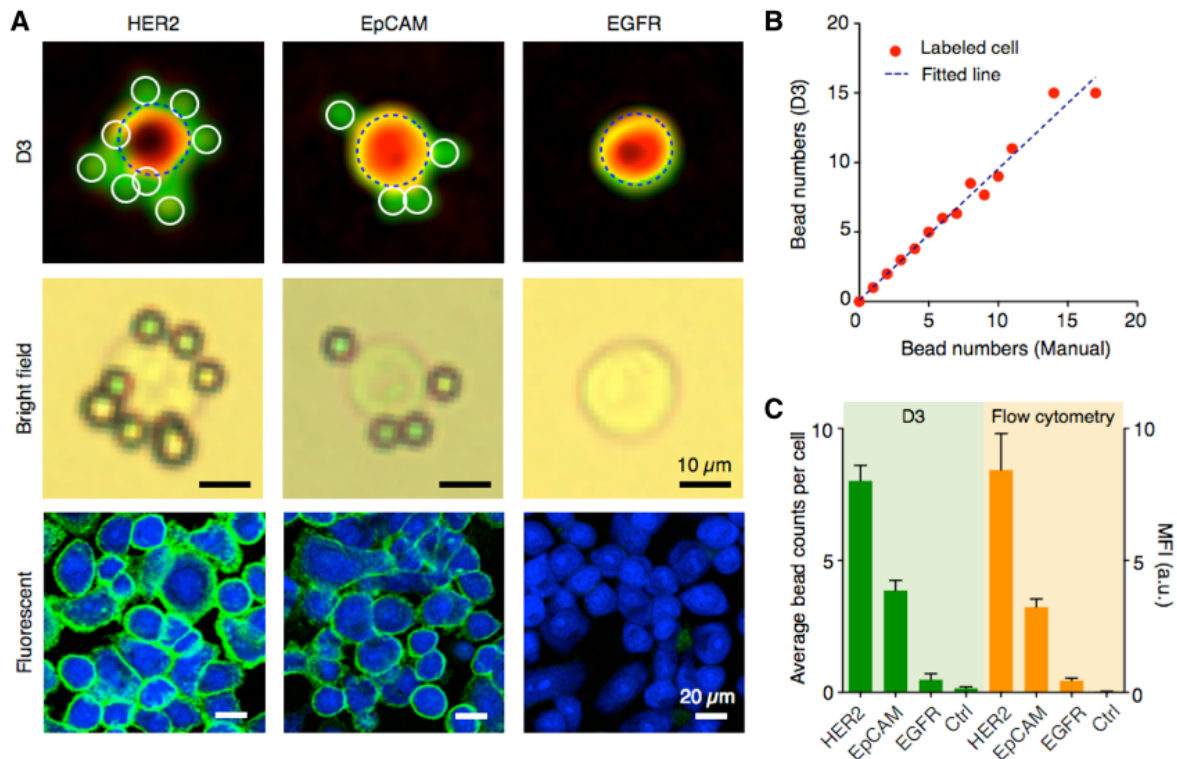
**Figure 2.8. Reconstructed images of leukocytes.**

Human leukocytes at physiological concentrations ( $\sim 5 \times 10^6$  cells/mL) were imaged in the field-of-view of  $24 \text{ mm}^2$ . Reconstructed amplitude, phase and raw diffraction images are shown for three selected spots. Unlike polystyrene microbeads, leukocytes are highly visible both in transmittance and phase images. Scale bar,  $500 \mu\text{m}$ .

### 2.3.2. Quantitative Cell Profiling

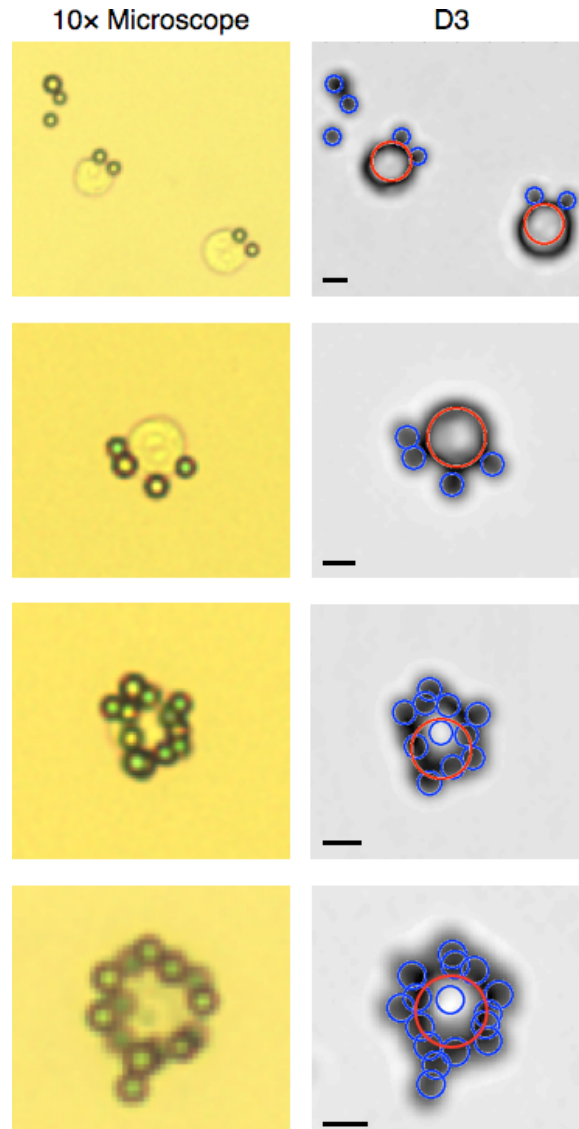
We next applied the D3 assay to cell profiling (Figure 2.9A). To validate D3-based cellular profiling, we measured the expression of three protein markers, human epidermal growth factor receptor 2 (HER2)/neu, epithelial cell adhesion molecule (EpCAM) and epidermal growth factor receptor (EGFR), on human cells (SkBr3, human breast carcinoma). Samples were immunolabeled with 7- $\mu$ m microbeads and analyzed using the D3 system. The average bead count per cell was highest for HER2/neu targeting (8.0 beads/cell), followed by EpCAM (3.9 beads/cell) and EGFR (0.5 beads/cell); these results were consistent with immunofluorescence microscopy. Unlike microscopy, however, the D3 assay enabled simultaneous analyses of far greater numbers of cells (>10000 cells) because of its wide field-of-view(>10 mm<sup>2</sup>). The cellular bead counts generated with automated D3 analyses were statistically identical with those from manual microscopy enumeration ( $p = 0.43$ ; paired t-test; Figure 2.9B and Figure 2.10). Further comparison with flow cytometry validated D3 assay's analytical capacity (Figure 2.9C). The number of beads per cell correlated linearly with levels of marker expression ( $R^2 = 0.99$ ). Similar D3 profiling on a different cell line (A431, human epidermoid carcinoma) also matched well with immunofluorescence microscopy and flow cytometry results (Figure 2.11).





**Figure 2.9. Detecting cancer cell markers with immunobead labeling.**

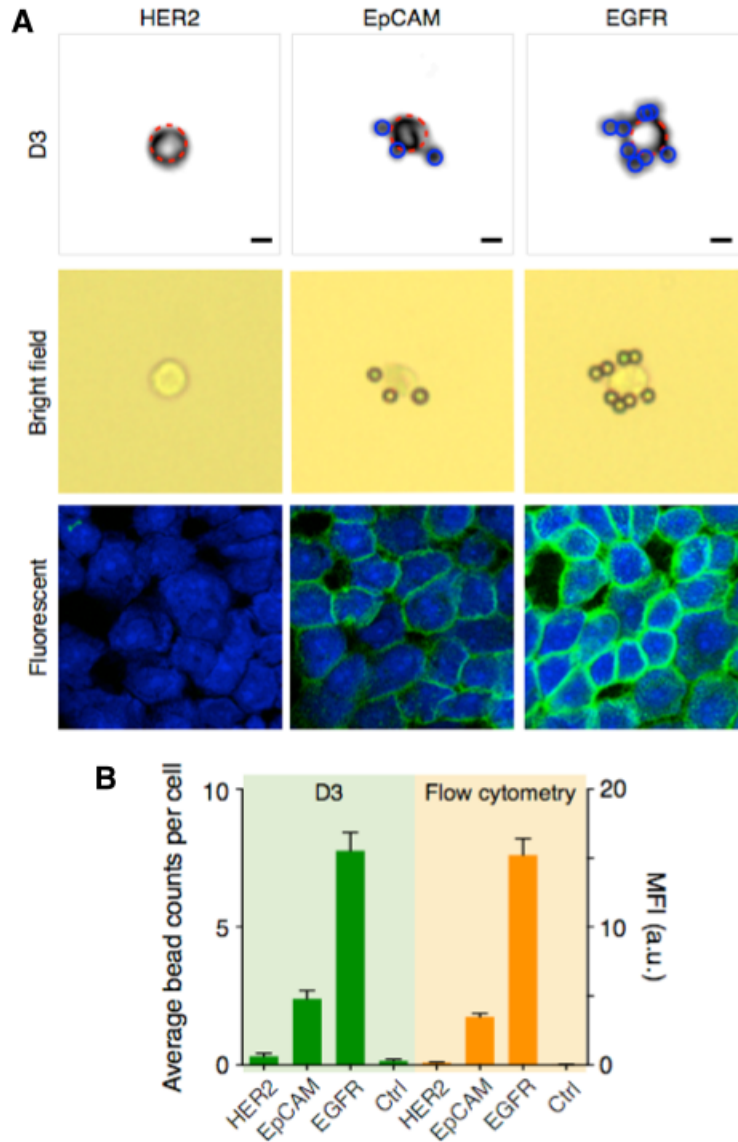
(A) Cancer cells (SkBr3, human breast carcinoma) were immunobead-labeled for HER2, EpCAM and EGFR. The top row shows reconstructed images in pseudo-color (green, transmittance; red, phase). The middle row is the corresponding bright-field micrographs. The bottom row, shows cells labeled with fluorescent antibodies for comparison. HER2, human epidermal growth factor receptor 2; EpCAM, epithelial cell adhesion molecule; EGFR, epidermal growth factor receptor. (B) The bead numbers on labeled cells, determined automatically by D3, were in good agreement ( $R^2 = 0.97$ ) with those counted manually from microscope images. (C) The average bead count per cell correlated with the expression level of a target marker as determined by flow cytometry ( $R^2 = 0.99$ ).



**Figure 2.10. Cancer cells labeled with different numbers of microbeads.**

Reconstructed images (right) are compared with conventional bright-field micrographs (left).

Both cancer cells and 7- $\mu\text{m}$  microbeads are accurately detected by the detection algorithm. Scale bar, 10  $\mu\text{m}$ .



**Figure 2.11. Molecular profiling of A431 cancer cells.**

(A) Reconstructed images of A431 cells labeled for HER2, EpCAM, and EGFR immunobeads (7  $\mu\text{m}$ , top row) are compared with corresponding bright-field microscope images (middle row). The number of beads on the cells correlates with the expression level of a target marker (bottom row). (B) The average number of beads per cell showed an excellent match with the mean fluorescence intensity (MFI) from flow cytometry ( $R^2 = 0.99$ ). Scale bar, 10  $\mu\text{m}$ .

## 2.4. Summary and Discussion

Global cancer rates continue to increase, and the World Health Organization (WHO) predicts new cases to rise to 19.3 million by 2025 as the world's population grows, ages and gains access to antiretroviral drugs{Beaglehole et al., 2011, #44569; Daar et al., 2007, #23957; Narayan et al., 2011, #80701; Trimble, 2010, #87516; Varmus and Trimble, 2011, #76720}. Rapid cancer screening in POC settings remains an unmet clinical need. The D3 strategy reported here could address some of the diagnostic challenges in resource-limited areas. By installing a small add-on module, the ubiquitous smartphone can be converted into a moderate-throughput screening tool. Molecular diagnoses are achieved by integrating immunolabeling assay, cloud computing and digital processing. The resulting system enables quantitative cellular analysis and reports not only cancer cell counts but also the expression levels of molecular markers.

We anticipate further improvements in some of analytical capabilities of D3. First, a next-generation system would incorporate multiplexed cellular detection based on different optical properties of microbeads. We have shown that microbeads can be differentiated based on their size and absorbance. Applying these signatures would enable multiplexed molecular profiling of the same cells to improve detection accuracy. In parallel, super-resolution approaches could be used to improve the spatial resolution{Bishara et al., 2011, #35031; Gazit et al., 2009, #84419; Mudanyali et al., 2013, #70327; Zheng et al., 2011, #96856}, and thereby further boost D3's multiplexing capacity. The compressive sensing{Brady et al., 2009, #11420}, in particular, could be adapted to numerically reconstitute high frequency information (i.e., small features in images) that is lost due to the discrete pixel size of an image sensor. By incorporating compressive

sensing, we expect to reconstruct images beyond the current resolution limit ( $\sim 1.5 \mu\text{m}$ ). Second, the DNA detection should be further developed for POC operation. This would require implementing disposable cartridges{Hoffmann et al., 2010, #20597; Liu et al., 2011, #70962} and portable systems{Huang et al., 2013, #49213; Jiang et al., 2014, #81967} for DNA extraction and amplification. Finally, the platform can be simplified for robust field-operation. We plan to establish a lyophilization protocol for transport and storage of reagents (e.g., antibodies, microbeads){Bhambhani and Blue, 2010, #74857}; and to extend validation tests using larger cohorts, variably skilled operators and diverse environment settings. These advances will position D3 as a versatile screening tool for various cancer types (e.g., cervix, breast, lymphoma) and infectious diseases (e.g. HIV, tuberculosis) with applications in field work, mobile clinics and home care settings.

# Chapter 3 Resolution Enhancement of Digital In-line Holography with Compressed Sensing

## 3.1. Background

### 3.1.1. Super-resolution Methods for Holography

Although lens-free digital in-line holography (LDIH) systems has achieved success in many microscopic applications, its resolution is limited by the pixel size of the inherent image sensors. Due to the nature of digital imaging sensors, hologram information smaller than single pixel is bound to be lost in the recording process. Hence the imaging target of LDIH has been limited to objects larger than the pixel sizes of its sensor. While imagers with smaller pixels would provide a higher resolution, the approach is practically limited by device cost, heating from high density pixels, and often reduced imaging area.

To overcome this limit, new resolution enhancement methods have been recently introduced to LDIH systems. The first method is multi-frame reconstruction {Zheng et al., 2010, #95617} {Bishara et al., 2011, #35030} {Guoan Zheng et al., 2011, #63857}. This method relies on using a sequence of low resolution images to reconstruct a single high resolution image. Such method increased complexity of image acquisition and often require additional hardware components. The other resolution enhancement method is using pixel function of imaging sensor. This method is prone to errors in the measurement system and therefore cannot resolve well for imager with small pixel sizes {Greenbaum et al., 2013, #70439}.

### 3.1.2. Compressed Sensing for Holography

In this work, the compressive sensing (CS) approach is chosen to overcome the resolution limit. Compressive sensing theory was developed in recent years to reconstruct signals from under-sampled measurements {Candes and Wakin, 2008, #43399} {Candès, 2006, #77509}. This approach is particularly appealing for LDIH systems, because it entails little modification in system optics and reduces data acquisition time. CS has been successfully applied to other holographic systems, including off-axis holography, multiple view projection holography, Fresnel holography {Marim et al., 2011, #41051} {Rivenson et al., 2013, #28022} {Rivenson et al., 2011, #28609}.

Despite its success in other holography systems, the use of compressive sensing in LDIH has been limited. This is mainly due to incompatibility between CS algorithms and the nonlinear nature of the LDIH recording system. The nonlinearity of LDIH comes due to the loss of phase information at recording step, as only amplitude information can be recorded by digital imaging sensors. Existing CS method is based on linear algorithms, namely L1-norm minimization techniques {Bruckstein et al., 2009, #32944}. L1-norm minimization is favored for CS because it is not an NP hard problem, and it is easier to implement with less computational efforts. However, given the nonlinearity of LDIH, L1 algorithms cannot be readily applied to the systems.

We propose a new CS method that can be used for LDIH and other nonlinear holography systems. Instead of L1 algorithm, this method uses a L0-norm minimization strategy. This strategy minimizes the total number of non-zero elements in a matrix, and is compatible with nonlinear measurement systems. L0-norm minimization has been successfully applied to other optical systems {Szameit et al., 2012, #9753}. However, L0-norm minimization method, to our

knowledge, has not been applied to any holographic systems. We show that this new CS method is capable of resolving sub-pixel features for LDIH with single-frame measurement. It can be used for reconstruction of objects with or without strong phase contrast. Compared to other resolution enhancement methods, it provides the advantage of single-frame exposure and uniform sampling measurement. Such advantages are crucial to POC imaging systems, such as D3 system mentioned in the previous chapter, because it ensures simple setup and fast image acquisition speed. Furthermore, this method can be used as a general framework for applying CS to nonlinear holographic setups.

## **3.2. Methods**

### **3.2.1. LDIH Measurement System**

Figure 3.1 shows the schematic of the LDIH measurement system used in this chapter. In this system, a partially coherent light source is generated using a monochromatic LED with a micron-sized pin-hole. The incident light illuminates the sample and interferes with the scattered light from the object. The CMOS imaging sensor (pixel size  $2.2 \mu\text{m} \times 2.2 \mu\text{m}$ ) is positioned directly underneath the sample and records the hologram resulted from the light interference. The platform is portable in size, low cost and provides a large field-of-view ( $20 \text{ mm}^2$ ).

With a unit magnification, the resolution limit of this LDIH system is the pixel size of its imaging sensor. The imaging sensor acts as a low pass filter in the spatial domain. The hologram information smaller than a single pixel are lost in the recording process. When imaging samples



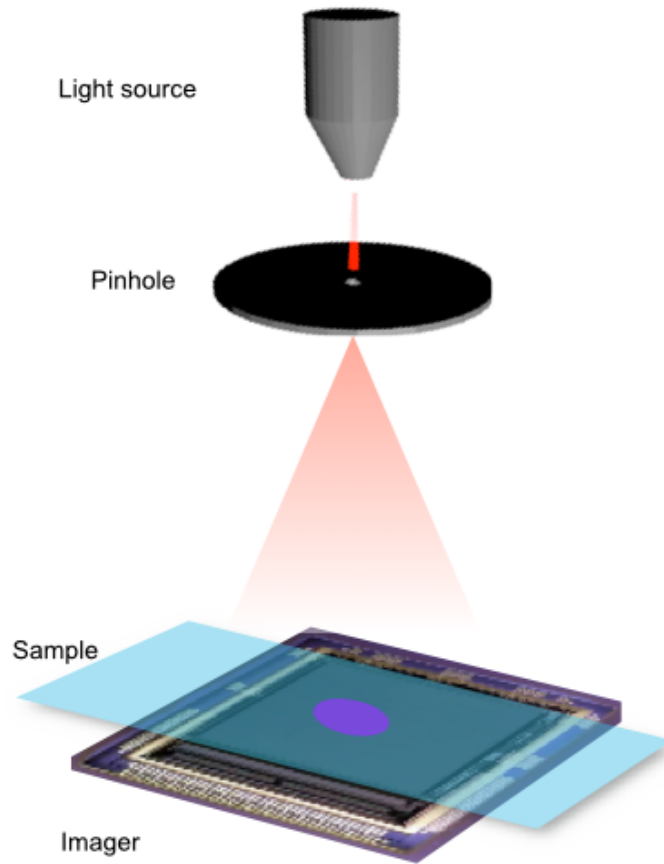
with features smaller than pixel size, the measurement becomes under-sampled and only blurred images can be reconstructed.

### 3.2.2.Imaging System Model

To recover under-sampled measurements, typical CS methods relies on L1-norm minimization strategy, which requires linear measurements. However, LDIH systems are nonlinear, which can be shown in its mathematical model for imaging acquisition. The mathematical model of the LDIH measurement is described as

$$y = |BHx| \quad \text{Eqn.1}$$

, where  $y$  is the recorded hologram from the LDIH system,  $x$  is the original object measured by the system,  $H$  denotes the hologram formation operator,  $B$  denotes the blurring filter associated with the CMOS sensor, magnitude operator  $| \cdot |$  is used because only intensity value can be recorded by the system. Eqn.1 shows a non-linear measurement system due to the loss of phase information in the recording process. Therefore L1-norm minimization techniques cannot be applied here without approximations, which can lead to inaccurate reconstruction result.



**Figure 3.1 Schematics of LDIH device.**

The light source is composed of an LED and a pinhole which generates partially coherent light. The sample is placed above the CMOS sensor.

### 3.2.3.L0-norm minimization

Given the system nonlinearity, we chose to apply the L0-norm minimization strategy. L0-norm measures the total number of non-zero elements in a matrix or vector. Its mathematical definition is

$$\|x\|_0 = \#(i \mid x_i \neq 0) \quad \text{Eqn.2}$$

Although computationally more complex than L1-norm minimization, L0-norm minimization has been successfully applied to other nonlinear optical system {Szameit et al., 2012, #31871}. To apply the L0-norm minimization to LDIH system, we set up the following optimization problem,

$$\begin{aligned} \min \|x\|_0 \\ \text{s.t. } \|BHx - y\|_2^2 \leq \varepsilon \end{aligned} \quad \text{Eqn.3}$$

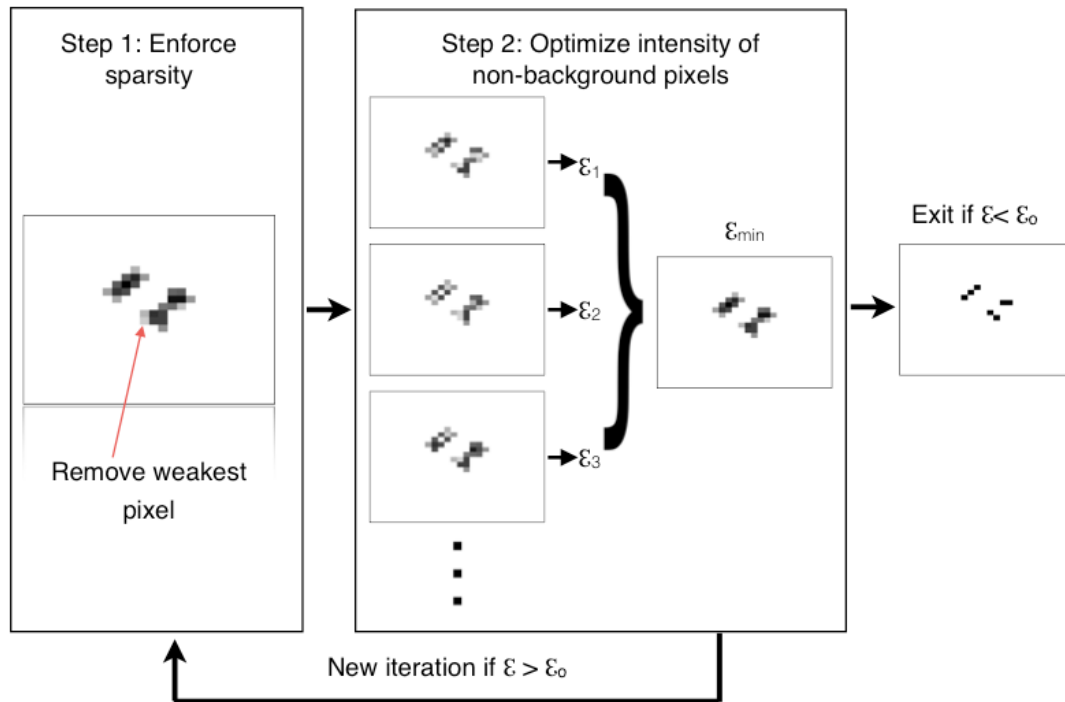
, where  $\|x\|_0$  is the L0-norm of  $x$ , namely the number of nonzero elements in vector  $x$ , which also represents the sparsity of the signal, and  $\varepsilon$  is the desired error threshold. From any image  $x$ ,  $|BHx|$  is the numerically estimated hologram for the system.  $\|BHx - y\|_2^2$  is then the discrepancy between the measured hologram and the estimated hologram derived from estimated signal. This optimization problem aims to find the sparsest possible solution of  $x$  (image reconstruction), such that the error value between measurement and estimated hologram is minimized. The technique works best when the original signal is sparse by nature or by mathematical transformation. For this work, we will focus on images that are sparse by nature.

### 3.2.4. Compressive LDIH Algorithm

To solve the L0 optimization problem in Eqn.3, we developed an compressive sensing algorithm, termed compressive LDIH (cLDIH) algorithm. This algorithm can reconstruct high resolution image from single-frame low-resolution measurement.

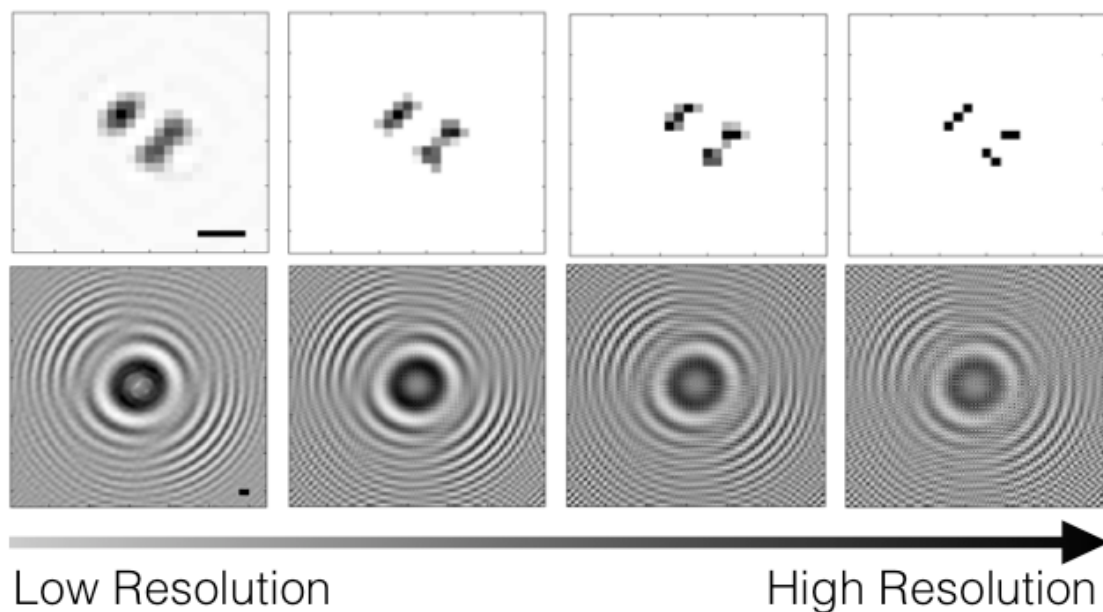
Figure 3.2 shows a block diagram demonstrating the algorithm. The algorithm goes through an iterative process, which gradually decrease the sparsity of the spatial image. In each iteration, two steps are performed in sequence. In the first step, the pixel whose value is closest to the background is removed from the image. This step reduces number of non zeros elements in the estimated signal and results in a smaller L0-norm, namely a more sparse signal. The second step is to solve the minimization problem  $\|BHx - y\|_2^2 \leq \epsilon$  using L-BFGS techniques. {Liu and Nocedal, 1989, #46455}. The second step finds the optimized signal x at a given sparsity and generates a new hologram with sub-pixel information. A low-pass filter is then applied to the new hologram to obtain a ‘simulated measurement’ according to the sensor properties of the LDIH system. The simulated hologram is then compared against the measured hologram to obtain an error value. The error value decreases as the solution converges to the true image. The algorithm exits the iteration once the error is less than the predetermined threshold.

Figure 3.3 shows an example of the progression of iterative process using a simulated object. Each iteration improves the resolution of the spatial image and the estimated hologram.



**Figure 3.2. Block diagram of compressive LDIH (cLDIH) algorithm.**

Compressive LDIH is an iterative process. Each iteration includes two steps. In the first step, the pixel with intensity closest to background is removed. In the second step, the intensity of other non background pixels is adjusted and error values are calculated for each new image.  $\epsilon_0$  is the threshold on error value to determine when to exit the program.  $\epsilon_1$ ,  $\epsilon_2$ ,  $\epsilon_3$  are the error values obtained by comparing measured hologram with holograms estimated from each new spatial image.



**Figure 3.3. An example of compressive LDIH (cLDIH) reconstruction.**

We used a simulated object to test cLDIH algorithm. An object containing sub-pixel features ( $<2.2 \mu\text{m}$ ) was simulated. A blurred hologram was then calculated based on the mathematical model of the LDIH measurement system. The blurred hologram was input into the original reconstruction algorithm from previous chapter to obtain the initial spatial reconstruction. The reconstruction is blurry because some features were sub-pixel in size. cLDIH algorithm was then applied to this spatial reconstruction and obtains a high resolution image identical to the original object. Images from left to right are outputs after iteration #1, #8, #18, #106. Scale bar,  $5 \mu\text{m}$ .

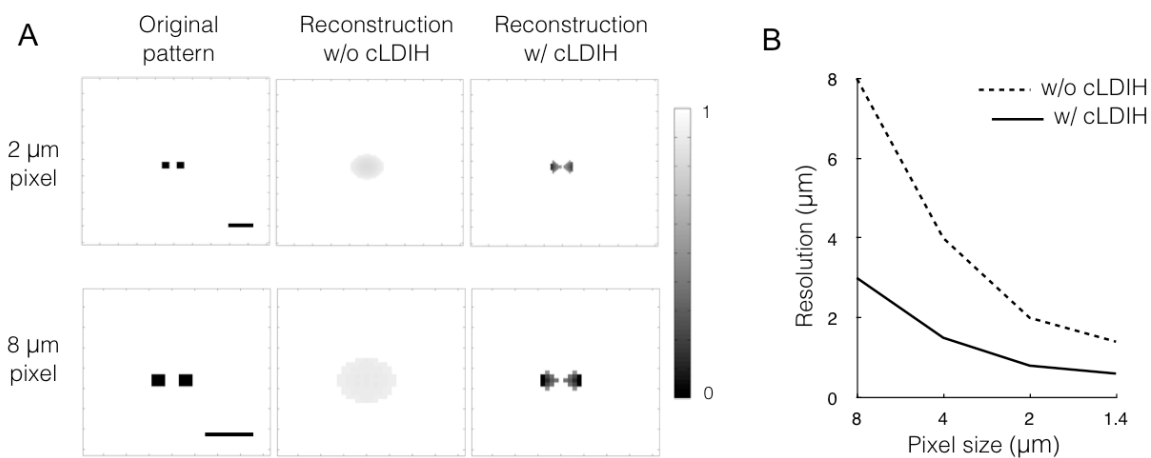
## **3.3. Demonstration**

### **3.3.1. Resolution of Compressive LDIH**

Figure 3.4 shows the resolution of compressive LDIH for various detector pixel sizes. We simulated holograms of two objects positioned at a distance smaller than the pixel size. The pixel sizes tested range from 1.4 to 8  $\mu\text{m}$ . The reconstruction results from cLDIH algorithm were compared against original reconstruction algorithm from previous chapter.

For the simulation, blurred hologram was calculated based on the pixel size value and mathematical model of the LDIH measurement system. The blurred hologram was input into the original reconstruction algorithm from previous chapter to obtain the initial spatial reconstruction. Because the distance between two objects was smaller than the pixel size, reconstruction without resolution enhancement cannot resolve the two objects. cLDIH algorithm was then applied to this spatial reconstruction to resolve the objects. To find the resolution limit of cLDIH, various distances between objects were tested until cLDIH can no longer resolve the objects.

Compared to the previous reconstruction algorithm, cDLIH gives two- to three- fold increase in resolution across a wide range of detector pixel size (Figure 3.4B).



**Figure 3.4. Resolution of cLDIH for various detector pixel sizes.**

(A) Top panel: Simulation of two closely positioned squares with distance  $0.8 \mu\text{m}$  and their holograms on a  $2 \mu\text{m}$ -pixel image sensor. Reconstruction results with and without cLDIH are shown. Scale bar,  $2 \mu\text{m}$ . Bottom panel: simulation of two squares with distance of  $3 \mu\text{m}$  and their holograms on a image sensor with  $8 \mu\text{m}$  pixel size. Scale bar,  $8 \mu\text{m}$ . (B) Comparison between reconstruction with and without cLDIH using simulation of holograms on image sensor with various pixel sizes:  $1.4, 2, 4, 8 \mu\text{m}$ .



### **3.3.2. Resolution Enhancement of Non-Phase Objects**

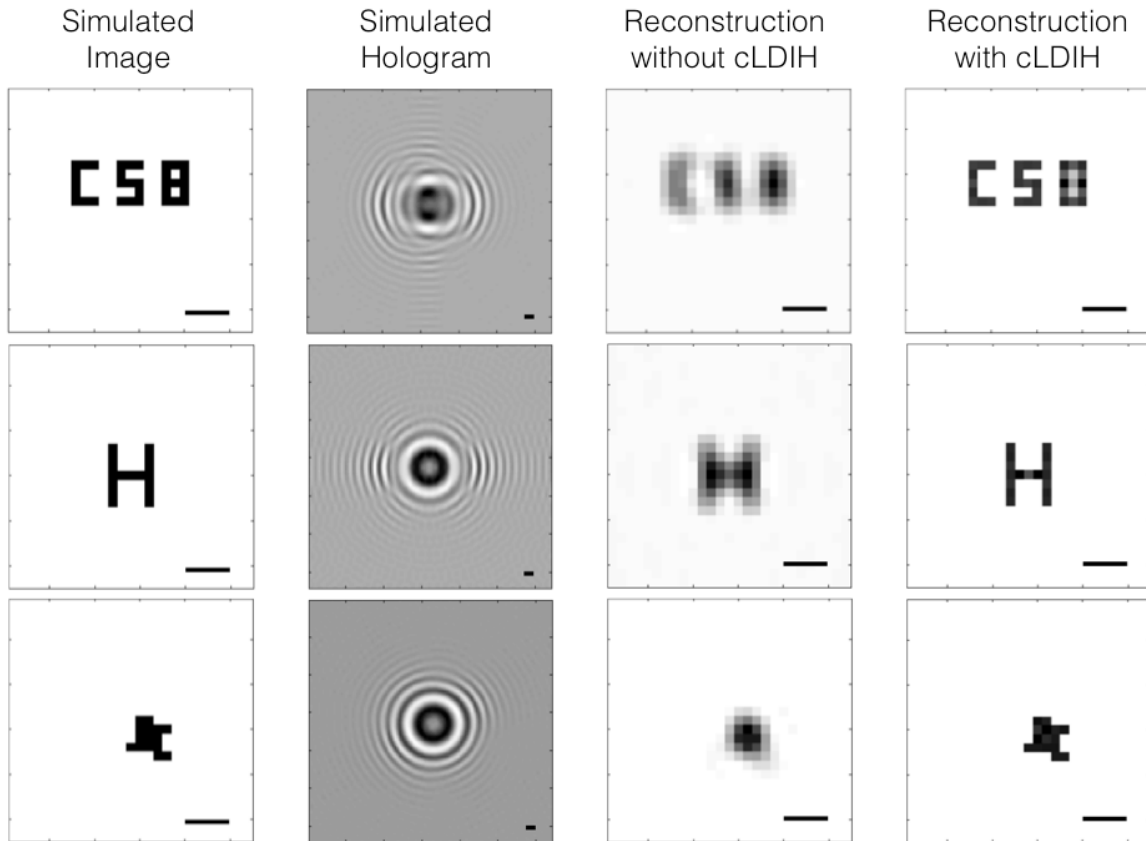
We further tested cLDIH reconstruction in numerical simulation with a variety of patterns, shown in Figure 3.5. Multiple object patterns and corresponding hologram patterns were simulated with 2.4  $\mu\text{m}$  pixel size. To model the pixel size limit of our system, we used perfect low pass filter in frequent domain as the blurring filter **B**. The low pass filter was applied to hologram patterns to simulate the measured hologram from the system. Using cLDIH, we successfully reconstructed 0.8  $\mu\text{m}$  object features using a 2.4  $\mu\text{m}$  pixel size in simulation.

### **3.3.3. Resolution Enhancement of Object Phase**

We further extended the algorithm to recover the object phase as well as the amplitude. The phase information is useful because it can be used 1) to remove unfocused twin images in LDIH reconstruction, and 2) to enhance contrasts between different objects (red blood cells *vs.* leukocytes). To incorporate phase reconstruction we model complex object  $X$  as  $X(m,n) = A(m,n) \cdot \exp[jP(m,n)]$ , where  $(m,n)$  refers to the spatial coordinate of  $X$ ,  $A(m,n)$  is the amplitude at position  $(m,n)$ , and  $P(m,n)$  is the phase at position  $(m,n)$ . We assume that  $A$  (amplitude) and  $P$  (phase) have the same shape, and thus their spatial sparsity are identical to each other.

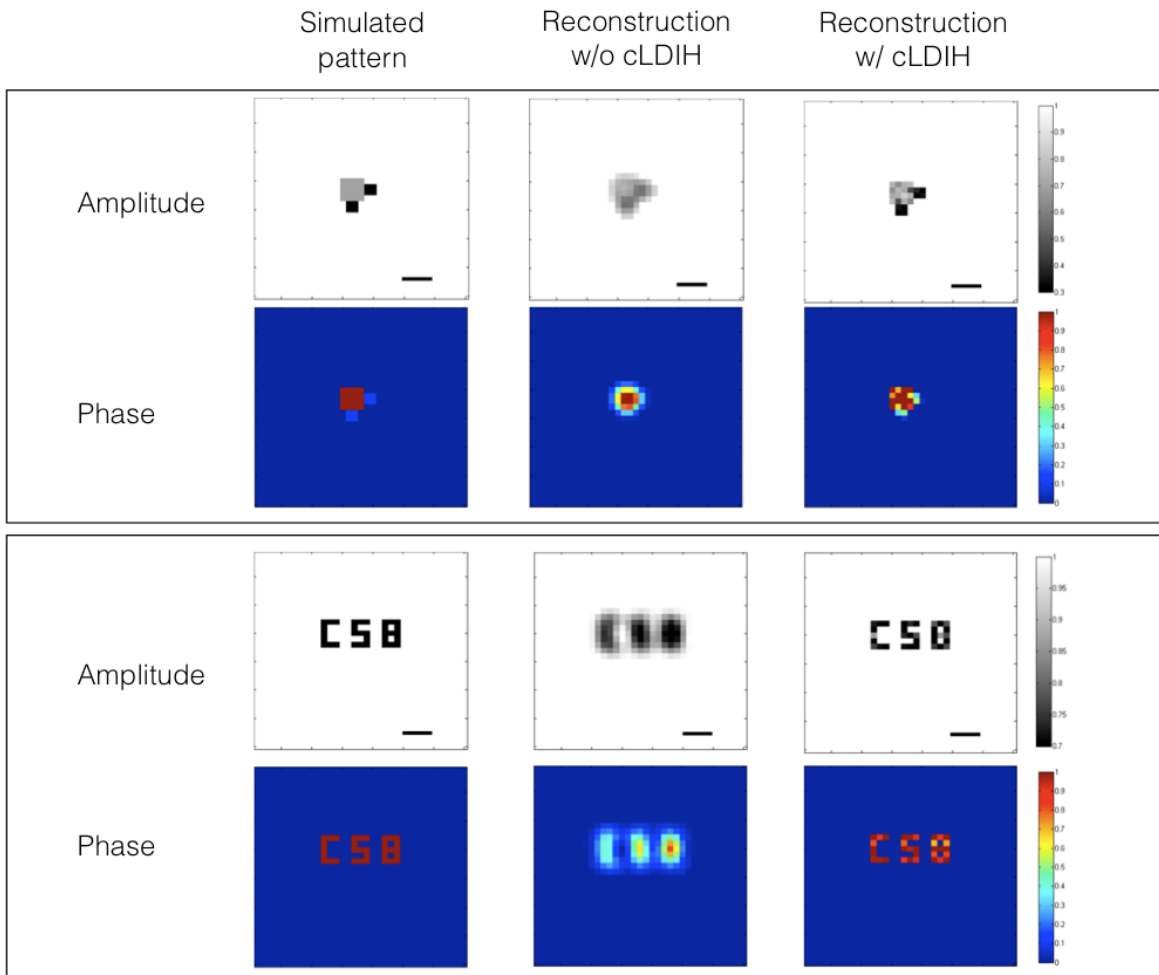
The differences between amplitude-only and phase-friendly algorithms are that 1) the latter method minimizes the the number of nonzero elements in both the  $A$  (amplitude) and  $P$  (phase) matrices; 2) it adjusts the pixel values in both  $A$  (amplitude) and  $P$  (phase) to minimize error; 3) it uses either  $A$  (amplitude) or  $P$  (phase) to determine which pixel to remove. In the examples shown in this paper, we used amplitude as the dominate factor when choosing weakest pixel in each iteration step.

We tested the phase-friendly algorithm using objects with homogeneous and inhomogeneous phase distributions (Figure 3.6). Patterns with feature size  $1.1\ \mu\text{m}$  were used and holograms were calculated with a low pass filter with a  $2.2\ \mu\text{m}$  pixel detector. Conventional reconstruction produced blurred images and inaccurate phase information. In comparison, both amplitude and phase were recovered with high fidelity using the proposed method. We found that the computational load for phase reconstruction algorithm is twice of the amplitude-only version. It's mainly because there are twice the amount of pixel variables to adjust in the error minimization step.



**Figure.3.5. Reconstruction of sub-pixel patterns using cLDIH.**

Patterns contain features as small as  $0.8 \mu\text{m}$ . In ‘CSB’ and ‘H’ patterns, the line width is  $0.8\mu\text{m}$ ; In the last pattern, the smallest width is  $0.8\mu\text{m}$ . Holograms are simulated with  $2.4 \mu\text{m}$  pixel size. Diffraction column shows the reconstruction result using conventional method. Wavelength is  $405\text{nm}$ . Object to detector distance is  $1.5\text{mm}$ . Scale bar =  $5\mu\text{m}$ .



**Figure 3.6. Reconstruction of patterns with phase contrast using CLDIH.**

Reconstruction of sub-pixel complex patterns using CLDIH. In the top panel, the line width of letters is  $1.1\mu\text{m}$ . Phase value is the homogeneous across the pattern and is different from the background. Holograms are simulated with  $2.2\mu\text{m}$  pixel size. In the bottom panel, the smallest feature of the pattern is  $1.1\mu\text{m}$ . Phase values vary inside the pattern. Wavelength is  $420\text{nm}$ . Object to detector distance is  $1.5\text{mm}$ . Scale bar =  $5\mu\text{m}$ .

### 3.4. Summary and Discussion

We have demonstrated a novel compressive sensing method for lens-free digital in-line holography (LDIH). Using a L0-norm minimization techniques, this method can improve the resolution of LDIH by three fold and is effective for imaging sensors with a board range of pixel sizes. Moreover, it does not require additional hardware or image acquisition steps. High resolution image can be reconstructed using single-frame measurement. Therefore it can be easily implemented for LDIH POC systems introduced in the previous chapter. Furthermore, it provides a framework for applying compressive sensing to nonlinear holographic systems.

There are several directions for future work on cLDIH. First, incorporating parallel computing technologies such as graphic processing unit (GPU) can help achieve real-time image reconstruction at sub-pixel resolution level. Second, to expand the application of cLDIH to non-sparse samples, mathematical transformations, such as wavelet transformation, can be added to the algorithm{Brady et al., 2009, #70176}. Third, cLDIH can be customized to solve specific clinical diagnostic problem. For example, the diagnosis of cervical cancer relies on the detection of abnormality in cell shape{Bengtsson and Malm, 2014, #86924}. These abnormality often manifests in non-smooth cell edges of sub-micron scales, and thus is difficult to detect using POC imaging systems with finite pixel sizes. Applying cLDIH algorithm can potentially achieve fast and accurate screening method for such disease.

# Chapter 4 Single-cell Capturing Chip for CNS Lymphoma

## Analysis

### 4.1. Background

#### 4.1.1. CNS Lymphoma Diagnosis

Central nervous system (CNS) lymphoma is diagnosed in about 10,000 new patients per year in the US and is either primary (de novo lymphoma) or secondary (metastases from systemic disease). Primary CNS lymphoma (PCNSL) accounts for 1,500 – 3,000 patients in the US, but affects an estimated 2-6% of all AIDS patients and is thus more prevalent in low/middle income countries with high AIDS frequency {Schabet, 1999, #21927; Villano et al., 2011, #41759}. With respect to secondary lymphoma, 25% of Diffuse Large B-Cell Lymphoma (DLBCL) and mantle cell lymphoma patients, and up to 50% of Burkitt Lymphoma patients will ultimately exhibit CNS involvement {Ziegler et al., 1970, #60656; Liang et al., 1990, #19495; Quijano et al., 2009, #55668; Gill et al., 2009, #14662}. Importantly, secondary CNS lymphoma is often the cause of death in high-grade lymphomas unresponsive to treatment {van Besien et al., 1998, #19820}.

Clinical diagnosis of CNS lymphoma typically relies on conventional cytopathology of CSF or radiographic means (MRI). Recent molecular distinctions have been made between germinal (GCB) type DLBCL, activated (ABC) type DLBCL, and Burkitt's lymphoma, and prognosis and treatment choices have been shown to depend on these cell-of-origin distinctions,

highlighting the need for a diagnostic platform that can support molecular phenotyping {Alizadeh et al., 2000, #58500; Rubenstein et al., 2006, #21434; Dave et al., 2006, #48162; Lossos and Morgensztern, 2006, #85276; Lenz et al., 2008, #31648}.

Lumbar puncture is used to collect small volumes of cerebrospinal fluid (CSF). CSF has a viscosity similar to that of water, and contains scant cells {Bloomfield et al., 1998, #23945}. In normal individuals, 1 mL of CSF contains 150-2,000 T lymphocytes, 80-1,100 monocytes, and 0-30 B lymphocytes, as well as other less common cell populations {de Graaf et al., 2011, #80392; Weston et al., 2011, #70731}. Table 4.1 summarizes the cell counts for the major cell populations. In patients with CNS lymphoma, lymphocyte populations increase in number and are often monoclonal. Conventional cytology (smear test) is only useful when lymphoma cells make up more than 5% of cells in a sample of CSF, and can be difficult to interpret due to similar morphology between benign and malignant lymphocytes {Hegde et al., 2005, #40169}. Newer approaches such as flow cytometry have shown impressive sensitivity, but require sufficient numbers of cells for analysis {Schroers et al., 2010, #85267; Weston et al., 2011, #70731}. Thus, estimates of secondary CNS lymphoma prevalence have differed in the literature.

	Normal	CNS lymphoma	Inflammation
B cells (per mL)	0-30	10-500,000	200-43,000
T cells (per mL)	150-2,000	250-180,000+ (max 97.2%)	9,000-460,000
Monocytes (per mL)	80-1,100	—	—
Granulocytes (per mL)	20-430	—	—
NK cells (per mL)	0-50	max 7.4%	1,500-50,000

**Table 4.1. Cell Counts in Cerebral Spinal Fluid**



To address these unmet needs, we sought to design a microfluidic chip that allows analysis of all harvested cells (i.e. without the need of sample preparation which often loses cells and/or alters them) and which could potentially be used in resource limited settings where HIV is more prevalent. Based on previous designs of chips incorporating individual cell capture/analysis{Peterson et al., 2013, #69899}, we designed and developed an integrated device that allows for comprehensive staining, phenotyping, and drug response measurements. We expect that this approach will provide a flexible platform to profile lymphoma cells from paucicellular samples, thus enhancing the accuracy and ease of CNS lymphoma diagnosis, the potential for biomarker-based treatments, and the ability to track the efficacy of those treatments over time.

## **4.2. Methods**

### **4.2.1. System Design and Fabrication**

We designed a microfluidic chip which meets several criteria for processing CSF samples, including a) sites to capture a large number of lymphoid cells, such that if lymphoma cells make up 0.1% of the population, we could capture sufficient numbers of cells to identify a monoclonal population, b) antibody-free capture, c) capture sites for cells in the 8-10  $\mu\text{m}$  size range, d) gaps so that erythrocytes would not be captured, and e) suitable build and materials for cellular analysis.

Figure 4.1 summarizes the procedure for lymphocyte detection and profiling. First, samples are harvested, typically in the range of 1-3 mL. The entire sample is then loaded onto the

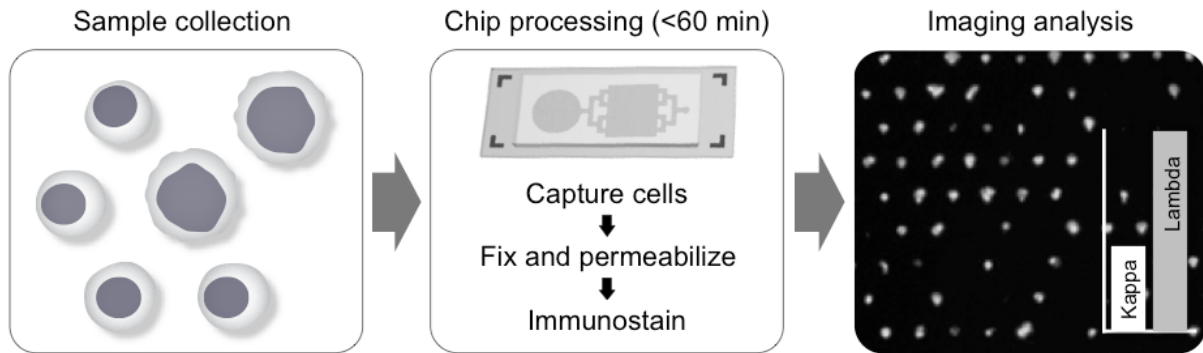
chip; individual cells are captured in sub-nanoliter traps and on-chip stained for fluorescent imaging. Acquired images are then analyzed with an automatic computational algorithm to generate cell characterization data.

The  $2 \times 4 \text{ cm}^2$  chip contains 24,000 staggered, butterfly-shaped traps arranged in four bands of  $20 \times 300$  (Figure 4.2). The capture site was designed to trap a single lymphocyte, while a  $4\text{-}\mu\text{m}$  gap between the butterfly “wings” was incorporated to allow smaller cells, such as erythrocytes, to pass through without being captured. The chips were fabricated via standard soft lithography and the estimated cost per chip is  $<\$1$ . Containing a large number of capturing sites, the chip enables high-throughput analysis. For instance, with typical flow rates of 2-5 mL/hr, target cells could be captured and stained in  $<1$  hour, important for processing clinical samples.

The fluidic system has a single-layer structure that is composed of a capture site region, a fluidic channel, and a debris filter at the inlet. (Figure 4.3) Injected fluids (e.g. cells, buffers, antibodies) first pass through the microfilter array ( $200 \mu\text{m}$  in diameter) in order to filter large aggregates and debris. The fluids then pass through the capture site region ( $12000 \mu\text{m}$  in width;  $5800 \mu\text{m}$  in length). Figure 4.2 shows the detailed dimensions of the single-cell capture sites, which were designed to capture lymphocytes  $\sim 10 \mu\text{m}$  in diameter. There are two capture regions with different gap sizes ( $W_1 = 30 \mu\text{m}$  and  $16 \mu\text{m}$ ;  $L_2 = 40 \mu\text{m}$  and  $25 \mu\text{m}$ ) for enhancing the capture rate. The height of the fluidic channel is  $25 \mu\text{m}$ .

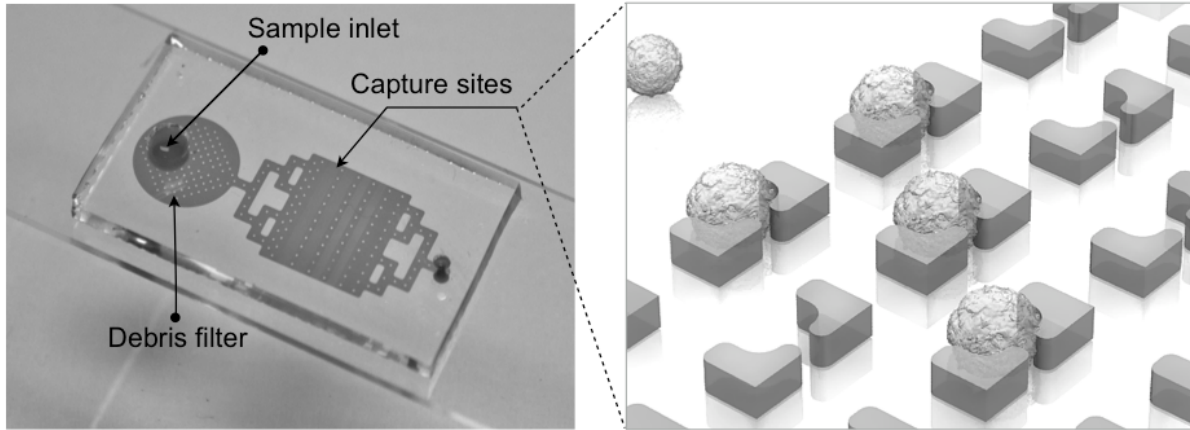
PDMS channels were made using the SU-8 wafer mold. After patterning, the wafer surface was treated by trichlorosilane (Sigma Aldrich, St Louis, MO, USA) under vacuum. PDMS (Dow Corning, Midland, MI, USA) was mixed with curing agent at a ratio of 10:1. The mixtures was poured over the treated wafer mold and baked at  $60 \text{ }^\circ\text{C}$  for one hour to cure. After

curing, the PDMS layer was lifted from the wafer and bonded to a glass slides using surface plasma treatment.



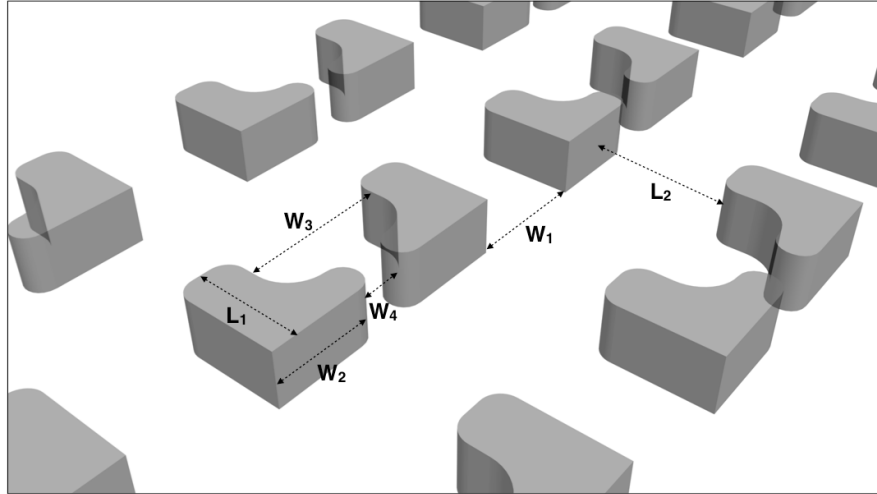
**Figure 4.1. Summary of lymphoma detection and analysis scheme.**

Paucicellular samples are harvested and captured on the chip without preprocessing. Following on-chip fixation, permeabilization, and immunostaining, the chip is imaged and cytometry is carried out with an in-house image process algorithm.



**Figure 4.2. Photograph and schematics of lymphocyte capture chip.**

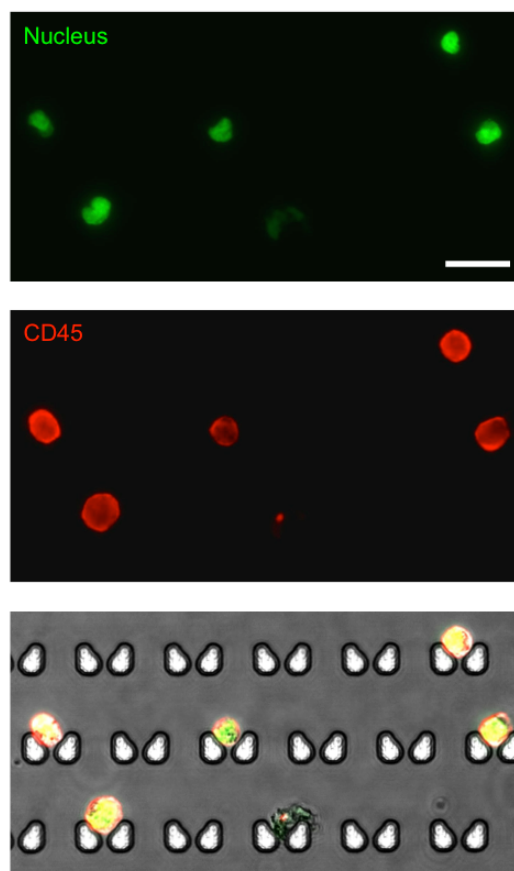
The chip attached to a microslide, showing inlet, debris filter, and capture area, which contains four arrays of  $20 \times 300$  single-cell capture sites.



**Figure 4.3. Fluidic structures in microfluidic chip.**

There are two capturing zones, one for capture larger cells and one for smaller. Design parameters for the capture sites are:  $W_1 = 30 \mu\text{m}$  and  $16 \mu\text{m}$ ;  $W_2 = 10 \mu\text{m}$ ;  $W_3 = 14 \mu\text{m}$ ;  $W_4 = 4 \mu\text{m}$ ;  $L_1 = 15 \mu\text{m}$ ;  $L_2 = 40 \mu\text{m}$  and  $25 \mu\text{m}$ .

#### 4.2.2. System Characterization



**Figure 4.4. Validation of on-chip capture and imaging.**

DB cells dual-labeled with Hoechst and anti-CD45-APC, and captured and imaged on-chip.

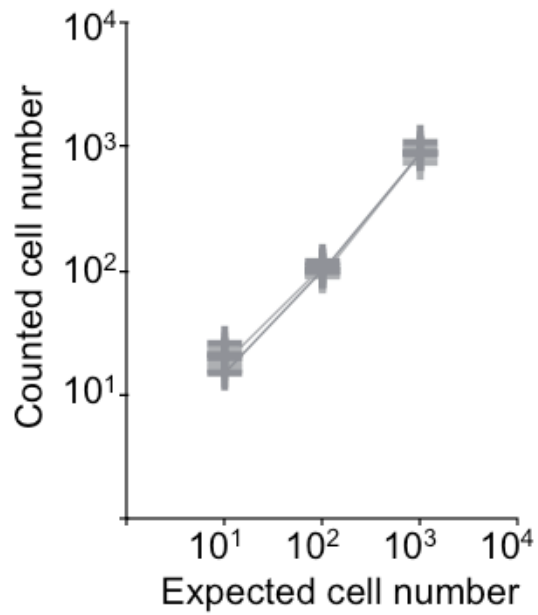
Capture sites are butterfly-shaped, staggered, and customized for lymphocyte size-based capture.

Scale bar, 25  $\mu\text{m}$ .

To validate the system design, cell lines were acquired from the following sources: DB, Toledo (Dr. Anthony Letai, Dana Farber Cancer Institute); RC-K8 (Dr. Thomas Gilmore, Boston University); SuDHL4, DOHH-2, Rec-1 (Dr. Russell Ryan, Massachusetts General Hospital); Daudi, Hut-78, Jurkat (ATCC). All cell lines (except Hut-78) were cultured (37 °C and 5% CO<sub>2</sub>) in RPMI 1640 media (Invitrogen) supplemented with 10% fetal bovine serum (FBS). Hut-78 cell line was cultured (37 °C and 5% CO<sub>2</sub>) in Iscove's Modified Dulbecco's Medium (Invitrogen) supplemented with 10% FBS.

We first characterized the device performance for cell capture. DB GCB-type DLBCL and the Daudi Burkitt lymphoma cell lines were stained for CD45 (an extracellular pan-lymphocyte marker) and nucleus, and samples were prepared with the nominal cell counts of 10, 100, or 1000 of the DB or Daudi cells. When these samples were processed by the chip (Figures 4.4 and 4.5), the observed capture efficiency was >90%; this contrasts with the 17-30% cell loss that occurs at each centrifugation step in traditional sample processing. {Dux et al., 1994, #13434; Kleine et al., 1999, #16609}

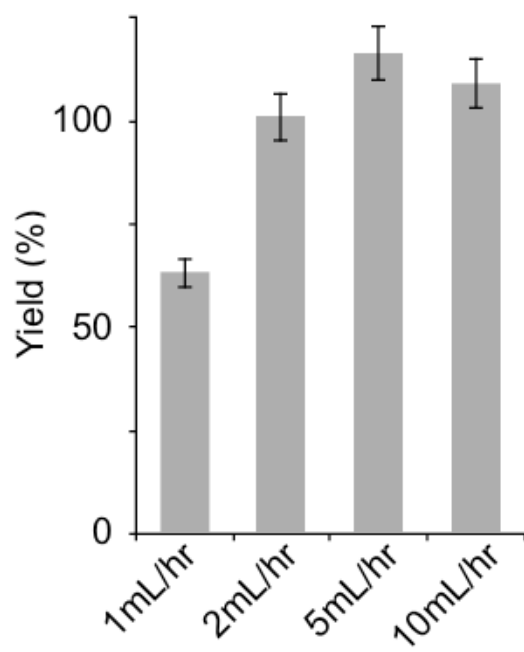




**Figure 4.5. Capture efficiency characterization.**

Capture efficiency of DB and Daudi cells is greater than 90% when 10, 100, or 1,000 lymphoma cells were introduced to the chip.

For the titration of cells, approximately  $1.5 \times 10^6$  cells from culture flasks were washed with PBS and stained for 30 min at room temperature in 1.5  $\mu\text{g}/\text{mL}$  Hoechst 33342 (Invitrogen) and APC anti-human-CD45 antibody according to manufacturer instructions (Clone HI30, BioLegend) in PBS containing 2% bovine serum albumin (BSA; Sigma Aldrich). Following a quick wash with PBS, cells were fixed in 2.6% paraformaldehyde (PFA) in PBS at room temperature for 20 min. Cells were then triple washed with PBS and counted using a hemocytometer (Hausser Scientific). The samples were diluted into quadruplicate aliquots of 10, 100, and 1,000 cells in 1 mL PBS in siliconized microtubes (Clear-view Snap-Cap, Sigma-Aldrich). Each sample was then introduced to a preconditioned device at a flow rate of 2 mL/hr. The captured cells were then counted via microscopy.



**Figure 4.6. Flow rate optimization.**

Optimization of flow rate based on capture efficiency of 10 μm beads.

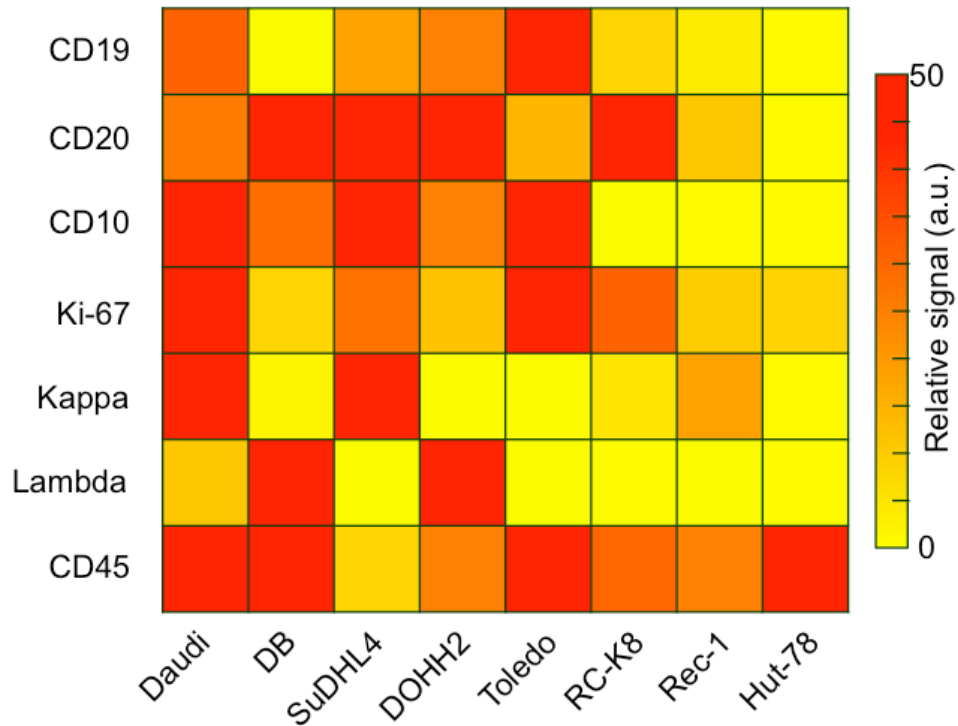
Fluorescent 10  $\mu\text{m}$  micro-beads (Bangs Laboratory, Fishers, IN, USA) were used to test capture efficiency and to identify the optimal flow rate. First, PDMS channels were preconditioned using pluronic copolymer solution with 0.1% F127 in DI water (Sigma Aldrich). The inlet of the channel was connected to a reservoir of beads in solution and the outlet to a syringe pump. The syringe pump was programmed to control the flow rate of the fluid. Bead solutions were diluted to 300 beads per 100  $\mu\text{L}$  and the total bead counts were about 300. After capturing, we use fluorescent microscope to image and count the total number of beads captured in the chip.

The optimal flow rate for maximal capture yield was between 2–5 mL/hr (Figure 4.6). At lower flow rates, cells could have more time to follow the fluidic stream, thereby bypassing capture sites.

### **4.2.3. Cell Line Profiling**

We profiled a panel of cell lines via flow cytometry to validate the markers and their respective antibodies (Figure 4.7). Besides the B-cell lymphoma lines Daudi and DB, we also profiled SuDHL4, DOHH2, and Toledo GCB-type DLBCL lines, the RC-K8 ABC-type DLBCL line, and the Rec-1 mantle cell lymphoma line. Hut-78, a T-cell line, was used as a control. The profiling results showed the importance of including both CD19 and CD20 to identify B cells; not all B-cell lines were found to express both markers. This finding is also supported by other reports that showed decreased CD20 in lymphomas either due to the cancer cell-of-origin or anti-CD20 immunotherapy. {Johnson et al., 2009, #15096; Hiraga et al., 2009, #75042; Miyoshi et al.,

2012, #80514} We also found the restricted expression of kappa or lambda light chain surface immunoglobulins, which are markers of clonality, across the cell lines.



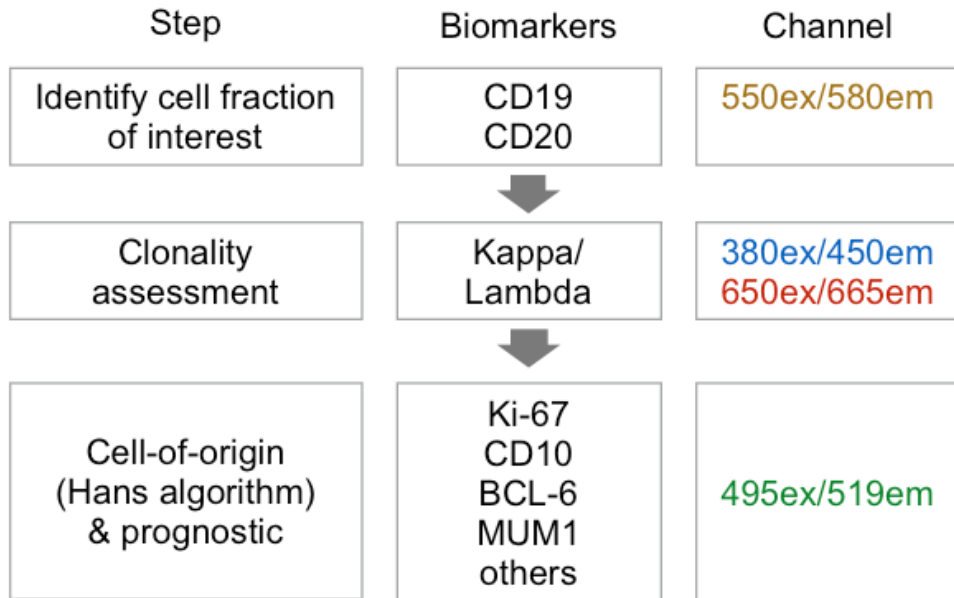
**Figure 4.7. Antibody validation and cell line profiling by flow cytometry.**

Relative expression levels of B-cell antigens relevant to diagnosis and prognosis (rows) on several lymphoma cell lines (columns). Daudi is a Burkitt’s lymphoma line; DB, SuDHL4, DOHH2, and Toledo are GCB-type DLBCL lines, RC-K8 is an ABC-type DLBCL line, Rec-1 is a mantle cell lymphoma line, and Hut-78 is a T-cell lymphoma control.

To perform flow cytometry, cells were fixed with 2.6% PFA (15 min at 37 °C), 2× washed with PBS, and then incubated (30 min) in PBS containing 2% BSA (staining buffer, SB). Approximately  $5 \times 10^5$  cells were incubated with 4.4 µg purified antibody in 42.5 µL SB (CD10, CD19, CD20, CD45, IgG) or with 2.5 µg purified antibody in 50 µL SB (κ light chain, λ light chain) for 30 min at 4 °C. Antibody clones and manufacturers are listed in Table 4.2. For intracellular Ki-67 detection, we used a commercial kit (Foxp3/transcription factor staining buffer set, eBioscience) to fix and permeabilize cells. In brief, cells were treated with fixation/permeabilization (fix/perm) buffer, followed by incubation (30 min) with permeabilization/wash (perm/wash) buffer containing 2% BSA (permSB).  $5 \times 10^5$  cells were then incubated with 5 µg purified anti-Ki-67 antibody (clone B56, BD) or mouse IgG control in 50 µL permSB for 30 min at 4°C. Cells were then washed 1× with SB or permSB, and incubated in 20 µL 1:100 R-phycoerythrin (PE) goat anti-mouse-IgG (H+L) (1 mg/mL, Invitrogen) secondary antibody for 30 min at 4°C in SB or permSB. Unstained controls were incubated in just SB or permSB at each step. Staining was done in 96-well V-bottom plates (Corning). Following 1× wash with SB or permSB, cells were resuspended into 200 µL PBS containing 0.5% BSA. Stained and unstained control samples were measured on a BD LSRII Flow Cytometer, and analysis was done using FlowJo software (Tree Star). Mean PE values were found for each cell line and antibody combination, and normalized to (signal - background)/(IgG - background) for CD10, CD19, CD20, CD45, and Ki-67 or (signal - background)/(secondary - background) for κ light chain and λ light chain.

#### **4.2.4. Labeling Strategy**

Captured cells could be analyzed on-chip through multi-color immuno-microscopy. As outlined in Figure 4.8, three classifications can be performed: 1) the use of CD19 and/or CD20 to determine B cells; 2) the use of kappa or lambda light chains to identify clonal populations; and 3) additional phenotypic markers for subtyping and prognostic tasks.



**Figure 4.8. Imaging strategy for clinical diagnosis**

Proposed workflow for clinical diagnosis using image analysis.

Several different lymphomas arise from germinal center B cells, such as Burkitt and some DLBCLs (GCB-type), but most primary CNS lymphomas are ABC-type DLBCLs. {Camilleri-Broet et al., 2006, #23255} As expected, we found that the GCB marker CD10 is expressed in all the GCB cell lines tested, but not in ABC-type or mantle cell lymphoma. Since ABC-DLBCLs tend to be more aggressive, we chose Ki-67 as an important marker for characterization and prognosis. {Broyde et al., 2009, #41469} Our data for the DB, DOHH2, and Rec-1 lines suggests that low Ki-67 in a monoclonal population would indicate the need to test additional lymphoma markers, such as for GCB-type DLBCL or mantle cell lymphoma. MUM1 may also be important, as it was shown to be expressed in over 90% of PCNSLs. {Camilleri-Broet et al., 2006, #23255}.

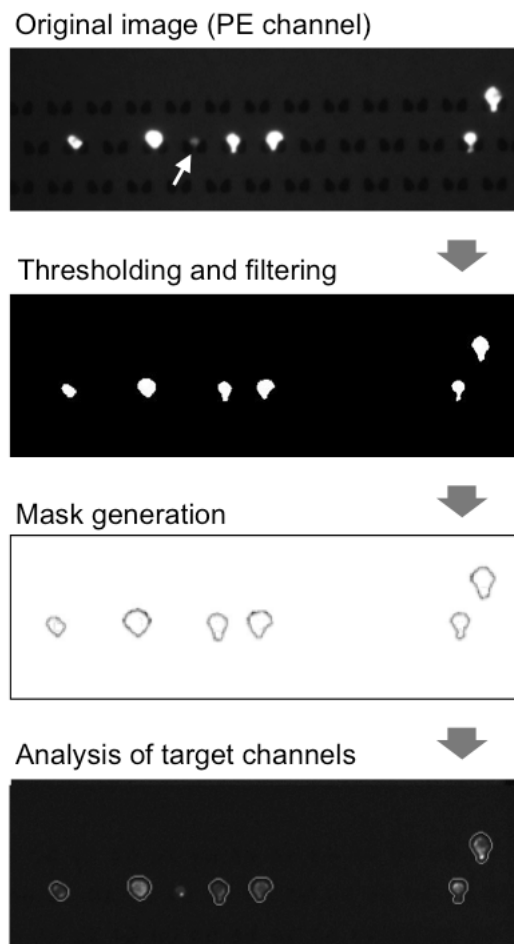
#### **4.2.5. Imaging Analysis**

As a proof-of-concept for analysis of lymphocytes from clinical samples, we developed an image processing algorithm for clonality assessment using the spiked CSF samples. Following the workflow described in Figure 4.9, we first made a mask around cells expressing CD19 and/or CD20 (PE channel), and then quantified the mean fluorescence intensity from our target channels in each individual cell (Figure 4.11). A size filter was also included to exclude non-cell debris from analysis (Figure. 4.11A, grey arrow).

Images were analyzed using an in-house Matlab (Mathworks, Natick, MA) script. Briefly, images from the CD19/20 (PE) channel were thresholded and binarized using Otsu's method with an additional uniform offset to compensate for the specific properties of the images. Following thresholding, image regions were analyzed and filtered by eliminating any regions



greater or less than preset total pixel areas based on the magnification of the images. Additional noise was filtered by using “open-close” morphological filtering. Boundaries of the remaining regions were then recorded and overlaid on target channels where values for the pixels in each mask area for both lambda (Alexa Fluor 647) and kappa (Brilliant Violet 421) channels were generated. Final values for both lambda and kappa channels for each cell were calculated by averaging the most intense 25% of pixels in each region.



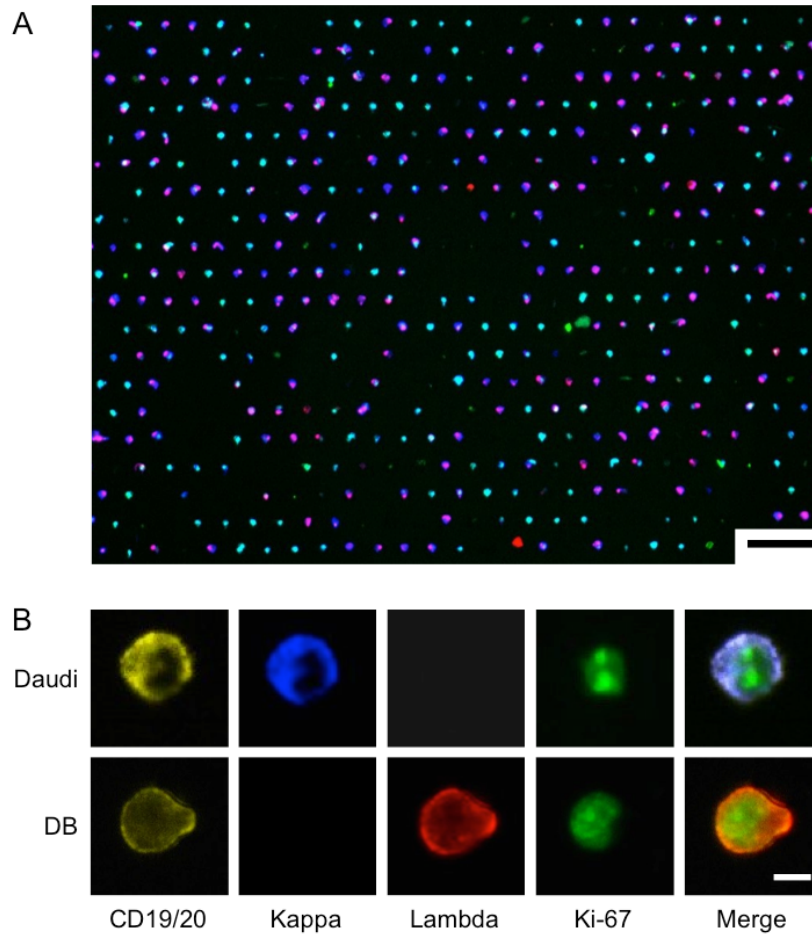
**Figure 4.9. Sample image analysis using an in-house image processing algorithm.**

Thresholding in the PE channel (CD19, CD20) is used to select B cells, and size-based filtering removes non-cell debris (white arrow). Target channels are analyzed within masks created from PE channel gating.

## **4.3. Demonstration**

### **4.3.1. On-Chip Cell Staining and Imaging**

We chose to use Daudi and DB cells as a model system for on-chip analysis, since they respectively highly express kappa and lambda light chain. To demonstrate both extracellular and intracellular antigen analysis, we performed on-chip staining of CD19/CD20, kappa/lambda, and Ki-67. We prepared cells for on-chip testing by diluting DB and Daudi lymphoma cells into artificial CSF. The cells were then fixed and stained on the chip, and imaged in four channels (Figure 4.10; see Table 4.2 for antibody clones and fluorochromes). Figure 4.10A shows the overlay of the four imaging channels after a 1:1 mixture of DB and Daudi cells was captured and stained on-chip. Figure 4.10B demonstrates high-resolution imaging of individual cells and markers. Although the cell populations appear to be heterogeneous, their restricted kappa/lambda expression can be seen at higher magnification.



**Figure 4.10. On-Chip Imaging.**

(A) 1:1 mixture of DB and Daudi cells were captured and stained on-chip using a cocktail of antibodies: anti-CD19-PE, anti-CD20-PE, anti-Kappa-Brilliant Violet 421, anti-Lambda-Alexa Fluor 647, and anti-Ki-67-Alexa Fluor 488. A. Low-magnification image shows overall capture site layout and cell heterogeneity. Scale bar, 75  $\mu\text{m}$ . (B) High-resolution images of differential expression of individual markers on the two cell lines. Scale bar, 5  $\mu\text{m}$ .

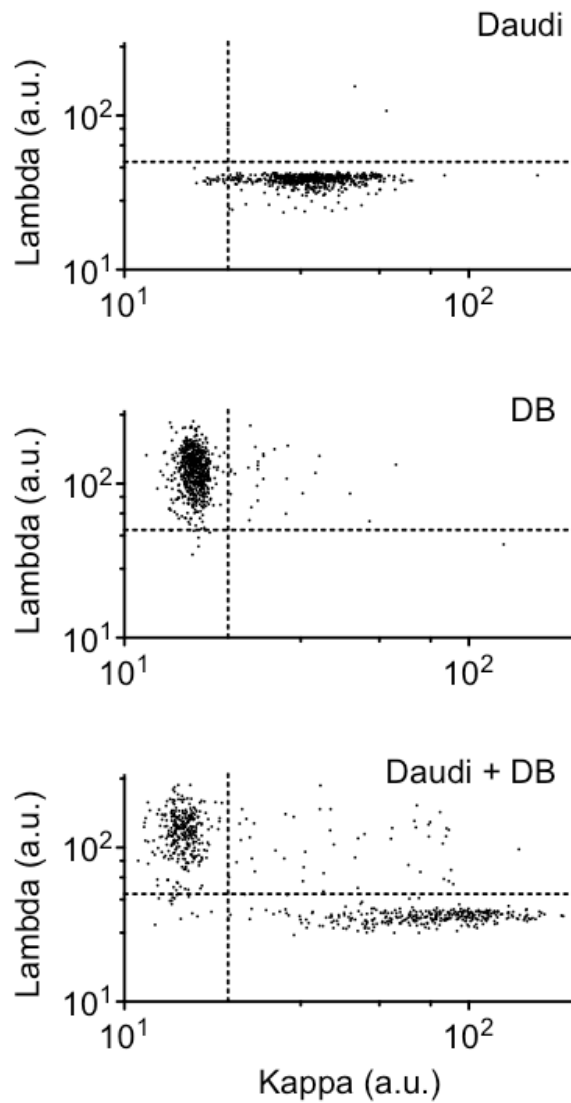
<b>Antigen</b>	<b>Clone</b>	<b>Provider</b>	<b>Fluorochrome (on chip)</b>
CD10	HI10a	BioLegend	—
CD19	HIB19	BioLegend	R-PE
CD20	2H7	BioLegend	R-PE
CD45	HI30	BioLegend	—
Ki-67	B56	BD Biosciences	Alexa Fluor 488
κ light chain	MHK-49	BioLegend	Brilliant Violet 421
λ light chain	JDC-12	BD Biosciences	Alexa Fluor 647

**Table 4.2. Antibodies for On-chip Imaging.**

### 4.3.2. Analysis of Clinical Samples

To perform on-chip imaging, about 1000 DB, Daudi, or a 1:1 mixture of cells were diluted into 1 mL of artificial cerebrospinal perfusion fluid (aCSF; Harvard Apparatus). Samples were introduced to the device at the flow rate of 2 mL/hr. Following the cell capture, fix/perm buffer was perfused over the cells for 10 min, followed by permSB for 5 min, and PBS containing 2% FBS and 1% BSA for 5 min, all at a flow rate of 1 mL/hr. A cocktail of antibodies containing 1  $\mu$ L of anti-Ki-67, anti-CD19, and anti-CD20, and 2  $\mu$ L of anti- $\kappa$  light chain and anti- $\lambda$  light chain was perfused over the cells at 1 mL/hr for 5 min. Lastly, to reduce background signal from antibodies binding to the channel surface, washing buffer (PBS with 2% FBS and 1% BSA) was perfused at 1 mL/hr for 5 min. Alternatively, cells were exposed to Ibrutinib-BFL using conditions recently described, {Turetsky et al., 2014, #57220} followed by staining with Hoechst 33342 and anti-CD20-APC (clone 2H7; BioLegend). Images were captured on a Nikon Eclipse TE2000S inverted microscope (Nikon) equipped with four filter sets (#31000v2, #41001, #41002b, #41024; Chroma Technology).

After quantification using our imaging analysis algorithm, we were able to clearly distinguish DB ( $\lambda$ -expressing) and Daudi ( $\kappa$ -expressing) cell populations from samples containing about 1,000 cells (Figure 4.11B).



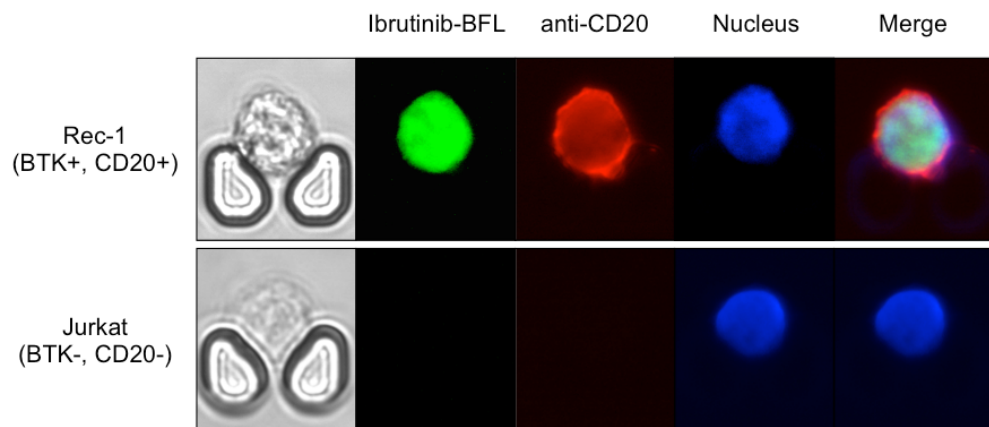
**Figure 4.11. Cell profiling for kappa/lambda monoclonality by image analysis.**

Scatterplots of mean pixel intensities from target imaging channels show clear separation of populations based on kappa and lambda light chain expression; top, DB cells; middle, Daudi cells; bottom, 1:1 mixture of DB and Daudi cells.

### 4.3.3. Drug Sensitivity Testing

We further performed drug sensitivity testing that would be clinically useful to guide intrathecal and/or systemic chemo- and targeted therapies. We used a companion imaging drugs that has recently been reported, Ibrutinib-BFL, an inhibitor of Bruton's Tyrosine Kinase (BTK); {Turetsky et al., 2014, #57220} other imaging drugs include fluorescent rituximab or caged methotrexate. Ibrutinib is approved for several B-cell malignancies, including mantle cell lymphoma, and the Rec-1 cell line has been shown to be sensitive to the drug. {Rahal et al., 2014, #35570; Ponader and Burger, 2014, #51617} Imaging the Rec-1 cells with Ibrutinib-BFL on the chip shows not only the binding of Ibrutinib, but also their cell-to-cell heterogeneity due to differences in BTK inhibitor sensitivity and BTK protein turnover (Figure 4.12).





**Figure 4.12. On-chip drug testing.**

On chip imaging of BTK-positive Rec-1 cells or BTK-negative Jurkat T-cell leukemia cells using fluorescent BTK inhibitor (Ibrutinib-BFL), anti-CD20-APC, and Hoechst stain.

## 4.4 Summary and Discussion

CNS lymphoma is difficult to diagnose and characterize at the site of disease, often requiring multiple invasive lumbar punctures to retrieve sufficient numbers of cells to allow cytopathologic analysis. Due to the paucicellularity and heterogeneity of CSF samples, we hypothesized that a microfluidic capture device would allow characterization of populations of lymphoma cells in the CSF on a single-cell level. Here, we showed that we can indeed image both intracellular and extracellular diagnostic markers from lymphoma cells spiked into artificial CSF in under an hour, and further use an image processing algorithm to quantitate their expression level. By adding additional criteria, differential diagnosis using the Hans algorithm can identify the cell-of-origin of a PCNSL, perhaps pointing to an undiagnosed systemic lymphoma if germinal origin is found{Hans et al., 2004, #19293; Camilleri-Broet et al., 2006, #23255}.

For secondary CNS lymphoma, it is important to know the extent of metastasis, its aggression, and its response to treatment. Methotrexate is currently used intrathecally or at very high systemic doses to treat CNS disease, but it has thus far not been possible to track response to treatment other than by low resolution MRI or insensitive cytology, neither of which would catch minimal disease{Abrey et al., 2005, #75525; Korfel et al., 2012, #90470; Korfel and Schlegel, 2013, #29787}. By profiling lymphoid cells in CSF based on kappa/lambda restriction or proliferative grade, or by customizing antibody staining for intracellular or extracellular markers based on particular characteristics of the primary tumor (e.g. c-myc rearrangement, CD10, CD5), CNS lymphoma cell counts can be tracked over time and prognostic assessments can be made{Lossos et al., 2004, #8275; Gurel et al., 2008, #4665}. Additionally, there are

several new lymphoma drugs in clinical trials, yet few are tested for CNS efficacy. This approach could provide a companion diagnostic that can directly test for brain-blood-barrier drug permeability or look for specific marker inhibition following intrathecal administration, such as BTK inhibitors or anti-CD20, {Antonini et al., 2007, #23882; Younes and Berry, 2012, #36102; Wilson et al., 2014, #508; Fleuren et al., 2014, #80963}. To test for such drug accumulation (single cell pharmacokinetics) in primary lymphoma cells, we tested Ibrutinib-BFL directly on chip. Finally, another approach includes removing CSF after intrathecal injection of chemotherapy drugs to track treatment response over time.

Additional technologies can be added to front- or back-processing on the chip for further improvements and applications. For example, it will be possible to further purify B cells by negative selection of other cell types, such as T cells and monocytes. Since the capture is passive (i.e., no antibodies on the chip), we can also use optical approaches to remove single cells of interest off the chip for further characterization, such as by quantitative PCR and sequencing — now possible on a single-cell level {Zong et al., 2012, #46322}. Another possibility will be to add a CCD or iPhone camera readout to enable the chip to be used for lymphoma diagnosis in resource-poor settings. We estimate that in this application a 1:5 cutoff ratio of kappa-to-lambda fluorescence signal would be enough to establish clonality with high specificity. Overall, we believe this new application of single-cell molecular profiling on a microfluidic chip for lymphoma will address questions regarding the diagnosis and treatment response of the disease not only in CSF, but also in other paucicellular samples such as fine needle aspirates, peritoneal fluid samples, pediatric applications or vitreous fluid analysis.

# Chapter 5 Magnetic-Microfluidic Chip for Circulating Tumor Cell Separation

## 5.1. Background

### 5.1.1. Separation of Circulating Tumor Cells (CTC)

Circulating tumor cells (CTC) have been shown as a promising biomarker for cancer diagnosis and treatment monitoring{Cristofanilli et al., 2004, #71167; Gottlieb et al., 1981, #79461}. However, its routine detection remains a challenge because of its low abundance in blood. Isolating these CTCs from blood sample can be as difficult as finding needles in a haystack.

Existing cell sorting methods include size-based filtration, antibody-based capture, and negative depletion. These methods have drawbacks when applied to CTC detection in blood. Size-based filtration often results in cell damage due to sheer stress{De Giorgi et al., 2010, #3807; Hosokawa et al., 2010, #29787; Lin et al., 2010, #26511; Zheng et al., 2007, #63707}. Antibody-based capture requires further release steps for downstream analysis{Gradilone et al., 2011, #8781; Nagrath et al., 2007, #511; Stott et al., 2010, #87073}. Negative selection has the advantage of minimal cell damage and releasing step. However, typical negative selection system requires multiple washing steps, during which process target cells can be lost. For low abundance cells such as CTC, this could leads to significant error in diagnostic results.

Currently, the most widely used cell sorting method in laboratories is fluorescence activated cell sorting (FACS). Despite its merits over other sorting systems, FACS device is inefficient for high volume screening and too bulky for POC diagnostic testing {Issadore et al., 2011, #83259}.

### **5.1.2. Magnetic-microfluidic Cell Sorting**

As an alternative to FACS, microfluidic sorting with immunomagnetic selection has emerged in recent years, which brings high potential for portable, low cost, high throughput cell sorting.

Immunomagnetic cell labeling strategy has been developed for effective selection of target cells. This strategy labels cells using magnetic particles coated with antibodies. Because of the high specificity of antibodies, cells can be effectively separated according to their molecular properties {Antoine et al., 1978, #72497; Negrath et al., 2007, #511}.

With the development of micro-fabrication, immunomagnetic separation can now be combined with high throughput microfluidic platforms to perform low cost, portable and high speed cell sorting {Kim and Soh, 2009, #73659; Pamme and Wilhelm, 2006, #56396} {Deng et al., 2001, #68967; Inglis et al., 2006, #40556; Xia et al., 2006, #59186}. One representative work is the hybrid magnetic-microfluidic filter system for the separation and profiling of CTCs {Chung et al., 2013, #22697}. One caveat of such system is the use of self-assembled magnetic particles. Although these magnets can generate strong local magnetic field in the microfluidic channel, they need to be embedded in the microfluidic channel during fabrication process. Consequently

the complexity of fabrication process increases and the microfluidic chip and magnetic materials cannot be reused.

To further simplify the process and further enhance the separation efficiency, we developed a new chess-board microfluidic-magnetic cell sorting system. It provides easier assembly process while achieving higher sorting efficiency.

## **5.2. Methods**

### **5.2.1. System Design**

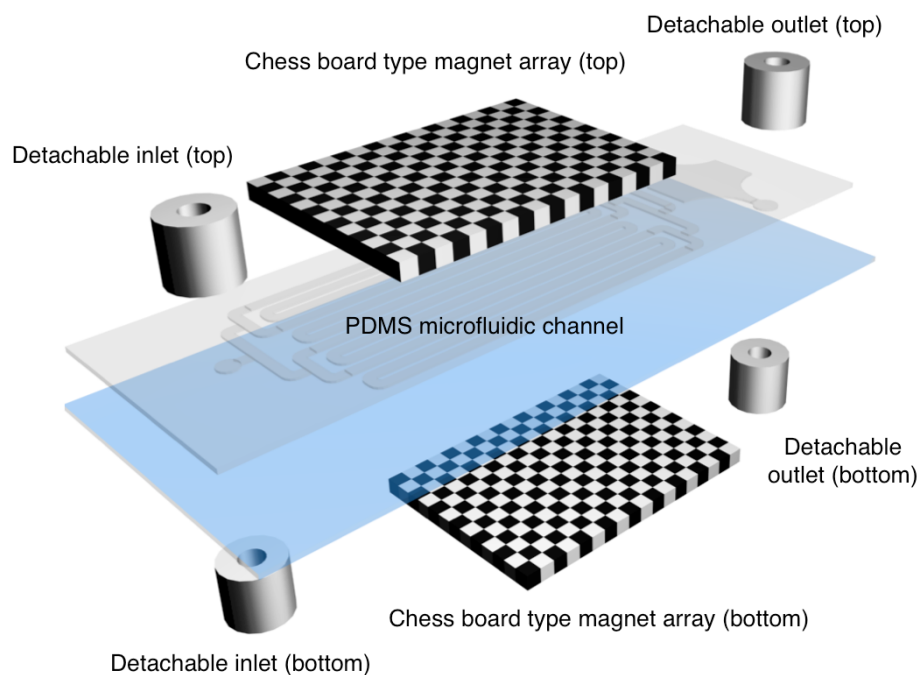
Figure 5.1 shows the schematics of the chess-board microfluidic-magnetic cell sorting system. This system has two layers of a chessboard-like magnet arrays. Each array has closely packed small magnets whose magnetic moments are alternating to each other (hence the term “chessboard”). We show in the next section that such magnetic configuration generates stronger trapping force compared to uniformly aligned magnet array.

A microfluidic chip with 50  $\mu\text{m}$  thickness is positioned in between the two magnet arrays. The chip includes into two regions (Figure 5.2). First region performs cell sorting and the second traps targets in single-cell capture sites for analysis. We choose negative selection strategy such that the target cells would not be labeled with particles. When samples of mixed cell population flow through the sorting region, non-target cells labeled with magnetic particles were trapped to the magnet arrays due to the magnetic field. Target cells free of magnetic moments can pass through the sorting region and enter capture region for single cell analysis. For application where

no additional signal cell analysis is needed, we use only the sorting region for simplification. The microfluidic chip is fabricated using standard SU-8 photolithography.

To facilitate easy assembly, two pairs of cylindrical magnets were used as fluidic inlet and outlet ports. The top magnet has a hollow bore wherein a tubing can be connected, or it can function as a standalone reservoir. The bottom magnet, which can be pre-installed in a device mounting holder, guides and pulls the top magnet.

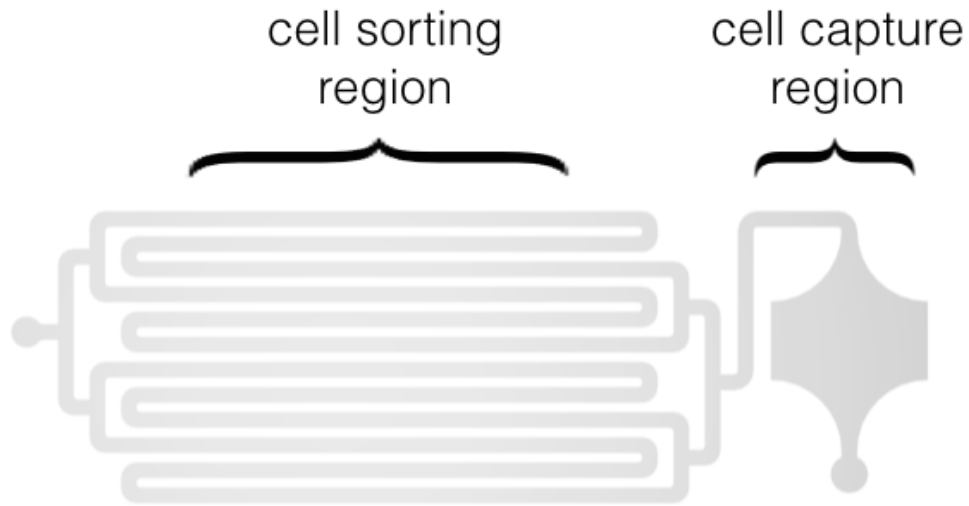
Figure 5.3 shows a cross section of the system. When a blood sample passes through the microfluidic channel, cells labeled with magnetic particles will be pulled by the magnetic force to top or bottom of the channel; the target cell, which is not magnetically tagged, will not be affected by the magnetic field and can pass through.



**Figure 5.1. Schematics of chessboard type magnetic-microfluidic cell sorter.**

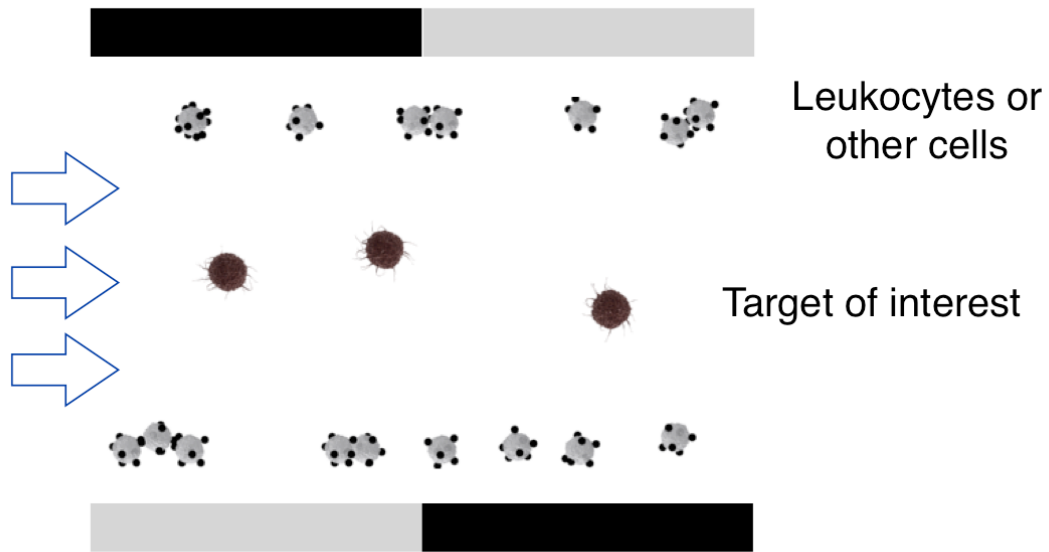
The system includes two chessboard-like magnet arrays, a microfluidic chip sandwiched in between the arrays, and two pairs of cylindrical magnets functioning as detachable fluidic inlet and outlet ports.





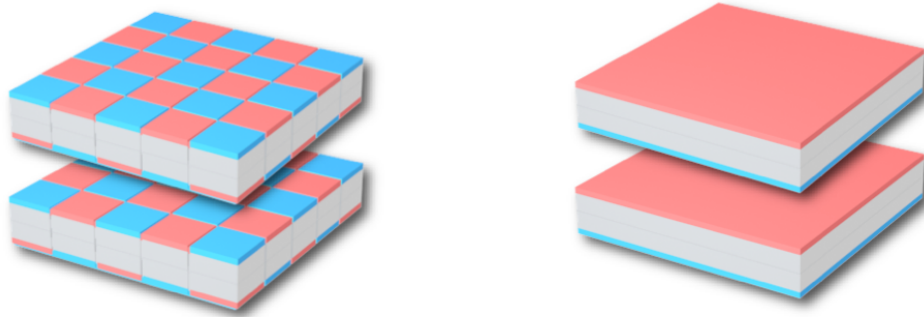
**Figure 5.2. Top view of microfluidic channel.**

The region on the left is for cell sorting and the region on the right is for single-cell capturing. The sorting region is positioned in between the magnet arrays. When cell sample passes through, cells labeled with magnetic particles will be trapped in the sorting region. The target (non-labeled) cells pass to the capturing region.



**Figure 5.3. Cross section view of system.**

The top and bottom panels are magnets with north (black) and south (grey) poles. The magnetic field generated in the microfluidic channel pulls the cells labeled with magnetic particles towards the magnets. The target cells remain unaffected by the field and pass through the channel along the flow direction.



**Figure 5.4. Configuration of magnet arrays in simulation.**

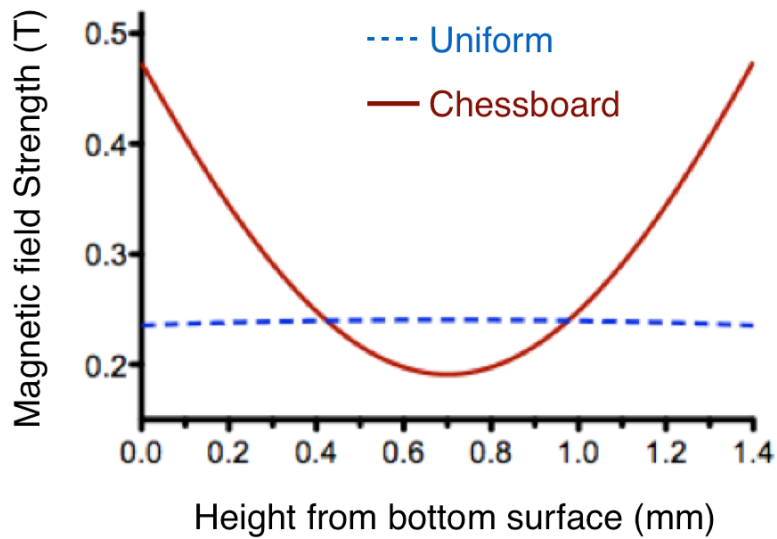
The left side shows the chessboard type magnet configuration and the right side shows uniform configuration. The magnet poles are color coded with blue (south) and red (north).

### 5.2.2. Magnetic Field Simulation

We show that chessboard magnet array can generate stronger magnetic force than its uniformly magnetized counterparts. The alternating magnetization can generate both a strong magnetic field ( $B$ ) and a large field gradient ( $\nabla B$ ). Thus the magnetic force, which is proportional to  $(B \cdot \nabla)B$  will be stronger in this configuration.

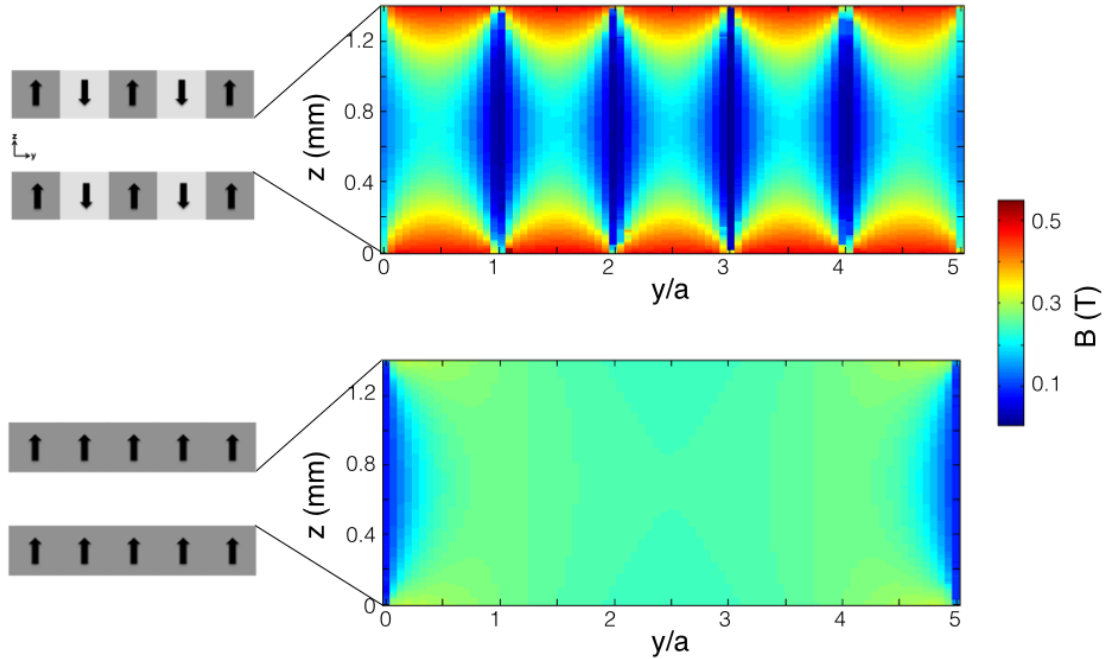
We first used 3D simulation tool (COMSOL Multiphysics) to calculate the magnetic field strength between the two arrays. Figure 5.4 shows the two magnet array of  $5 \times 5$  alternating magnets (1.55mm side length), and two uniform magnets of the same geometric setup. The NdFeB material was modeled with saturation magnetization  $M = 750 \text{ kA/m}$ .

Figure 5.5 shows the magnetic field strength  $B = |\mathbf{B}|$  change along  $z$ -direction (from bottom array to top array) between two magnet layers. It is shown that chessboard configuration results in a large absolute value of magnetic field component in the  $z$ -direction ( $B_z \sim 0.48 \text{ T}$ ) at  $z = 0 \text{ mm}$  (bottom) and  $z = 1.4 \text{ mm}$  (top); and a small absolute value of  $B_z \sim 0 \text{ T}$  in the middle of the gap. In contrast, the uniform magnet configuration results in an uniform magnetic field value of about  $0.35 \text{ T}$ . Not only the peak field strength is greater for the chessboard arrays, but also the quick change of  $B_z$  from the chessboard arrays contributes to strong gradient and hence stronger trapping force than the uniform arrays. Figure 5.6 shows the cross section of the same simulation. It further confirms the trend mentioned above.



**Figure 5.5. Magnetic field distribution along z-direction (from bottom to top array).**

The chessboard configuration generates a varying magnet field along z-direction, with stronger field near the magnet arrays and weaker in the middle of the gap. On contrast, the two pole magnet configuration generates a uniform field across the gap. For most regions, the uniform array has a weaker magnetic field than the chessboard design.



**Figure 5.6. Cross section view of magnetic field strength.**

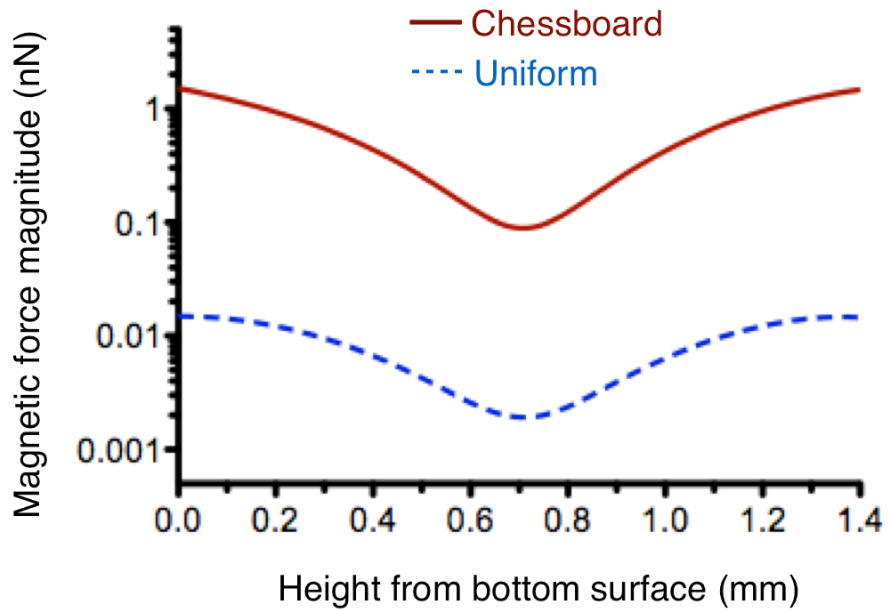
Top panel shows magnetic field strength  $B$  between the chessboard array ( $5 \times 5$ ). Bottom panel shows the magnetic field between uniform arrays.  $y$  is the horizontal direction and  $z$  is the vertical direction. To adjust for the variation of magnet size, we denote 'a' as the length of each small magnet. The  $y/a$  (unit-less) measures the horizontal distance with respect to the magnet size.

### 5.2.3. Magnetic Force Calculation

We calculated the magnet force generated by the chessboard arrays in the microfluidic channel. The magnetic force on a magnetic particle can be expressed as

$$F = \frac{V\chi}{\mu_0} (B \cdot \nabla) B$$

where  $V$  is the volume of the particle [m<sup>3</sup>],  $\chi$  is the susceptibility of the particle [dimensionless], and  $\mu_0$  is the vacuum permeability [V·s/A·m]. Using above equation, we calculated the magnetic force in both configurations, the chessboard array and the simple two-pole system. We assumed particles with 1  $\mu\text{m}$  radius and unit susceptibility. The simulation results show that the chessboard generates about 100 times larger force than the two-pole magnet (Figure 5.7).



**Figure 5.7. Comparison of magnetic force (chessboard vs uniform).**

The force is shown in log scale along z-direction from bottom to top magnet array. Chessboard type configuration, shown in red, leads to two order of magnitude increase in force from the uniform configuration (blue).



## 5.3. Demonstration

### 5.3.1. On-chip Bead Separation

To test the sorting efficiency of the system, we first used magnetic bead mixed with non-magnetic polystyrene beads (Figure 5.8). To facilitate better visualization, we use non-magnetic beads carrying red fluorescence and the magnetic beads carrying green fluorescence. A representative portion of the initial mixture of beads is shown in Figure 5.9. In the initial mix, A small quantity of non-magnetic beads were mixed with a high concentration of magnetic beads. Only sorting region in the microfluidic chip was used for this test.

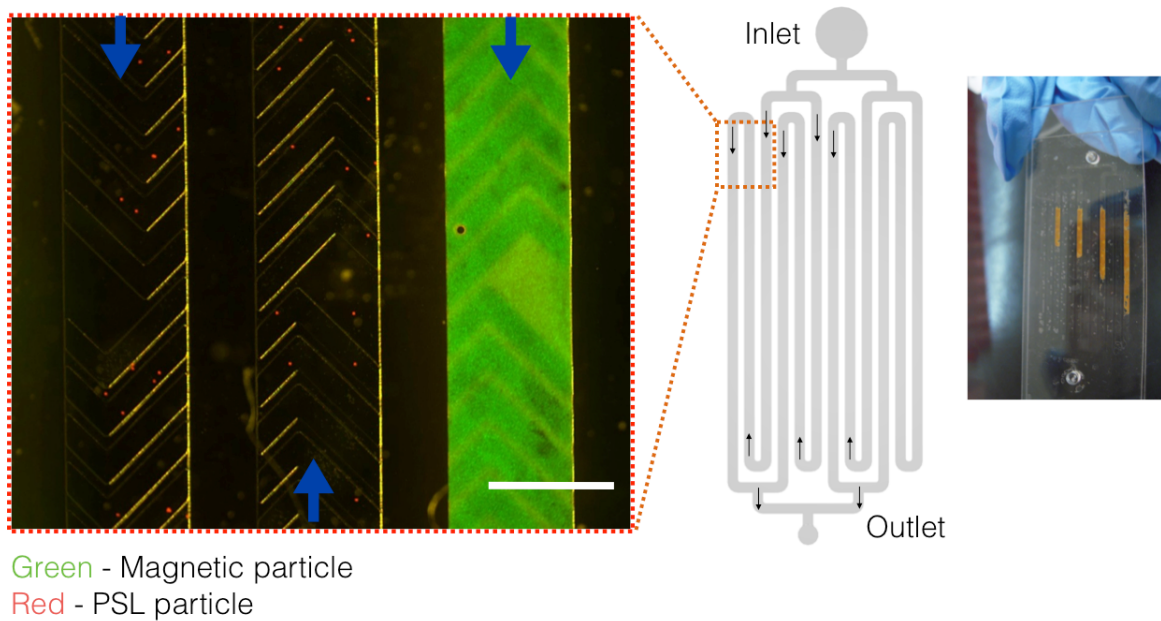
After passing the initial mix of beads through the system, nearly all magnetic beads were captured in the sorting zone (Figure 5.8). Figure 5.9 outlet image shows that no magnetic beads were observed at the outlet.

To further quantify the sorting efficiency of the system, the metric of enrichment ratio was used. We denote the number of non-magnetic particles at inlet as  $P_1$ , the number of magnetic particles at inlet as  $M_1$ , the number of non-magnetic particles at outlet as  $P_2$ , and the number of magnetic particles at outlet as  $M_2$ . The enrichment ratio of the system can then be measured by the equation below:

$$\text{Enrichment ratio} = (P_1/M_1)/(P_2/M_2).$$

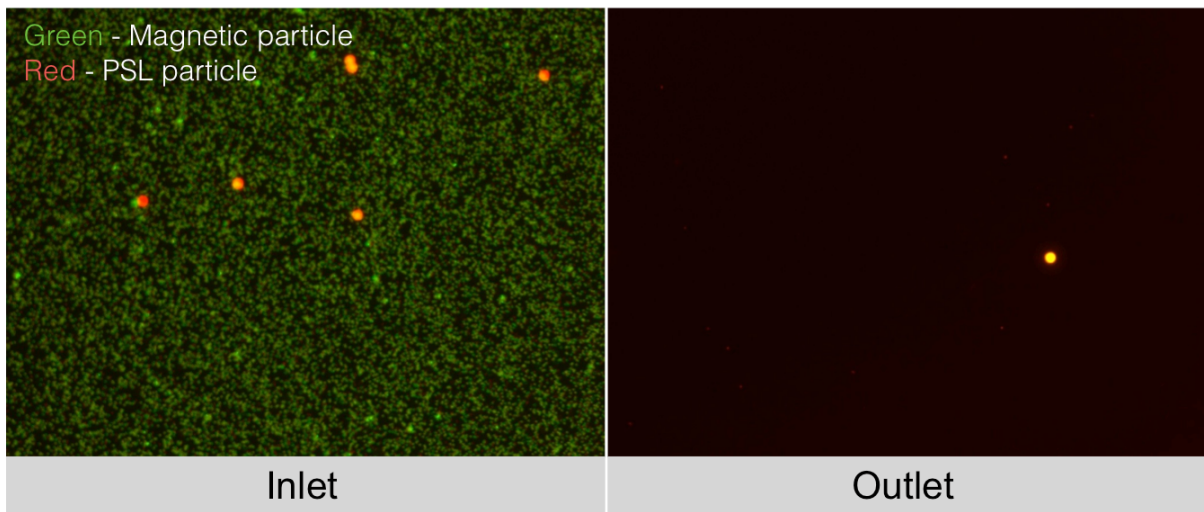
The number of particles before and after magnetic depletion was measured using a flow cytometer (LSRII, BD Biosciences), before ( $i = 1$ ) and after ( $i = 2$ ) the magnetic depletion. The enrichment ratio was then calculated (Figure 5.10). Multiple flow rates were used in this test. The chessboard type magnetic filter achieved highest enrichment ratio ( $\sim 30,000$ ) at 2 mL/hr flow

rate. Even at high flow rate of 20 mL/hr, it achieved enrichment ratio of (~3,500). The results confirm that this system can achieve higher enrichment ratio than previous work.



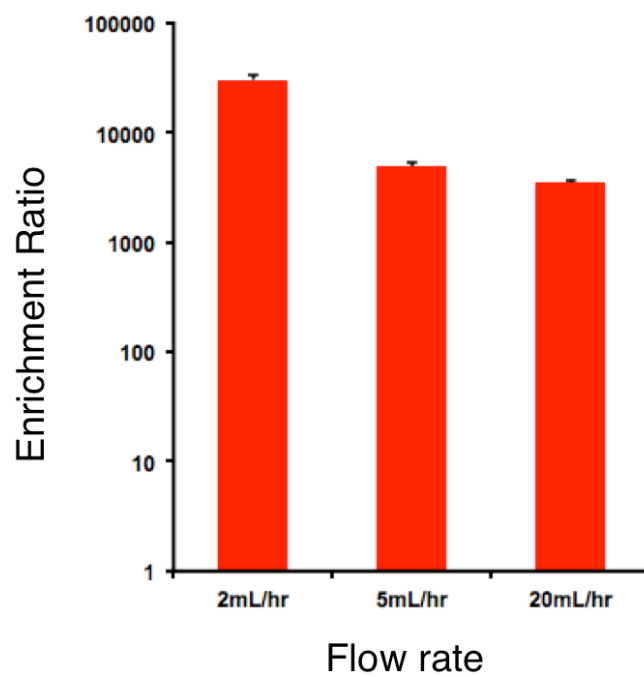
**Figure 5.8. Enrichment ratio test using microbeads.**

The image on the left is a zoomed-in section of the microfluidic channel taken under fluorescent microscope. The schematic of entire microfluidic chip is shown in the middle. The actual microfluidic chip after depletion is shown in the right most photo. The arrows in the channel indicate the flow direction. In the zoom-in fluorescent image, green magnetic beads are shown to be trapped in the beginning of flow path; red non-magnetic beads were shown in down stream the flow. The photo of the actual chip is taken in bright field. Magnetic beads (orange color in bright field) are shown to be trapped in the upstreams of the flow. PSL particle stands for polystyrene particles.



**Figure 5.9. Representative images at inlet and outlet from enrichment ratio test.**

The images were taken under a fluorescent microscope. The inlet mix contains a high concentration of magnetic beads (green) and a low concentration of nonmagnetic beads (red). After depletion, the mix at outlet only contains the non-magnetic beads. PSL particle stands for polystyrene particles.



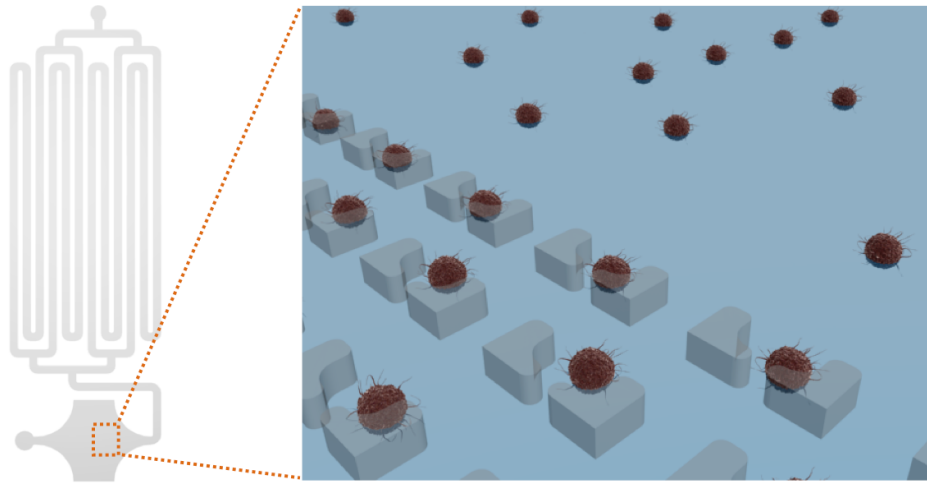
**Figure 5.10. Enrichment ratio of the system from bead sorting test.**

The enrichment ratio was tested at different flow rates. The highest efficiency (~3500) was achieved at 2 mL/hr.

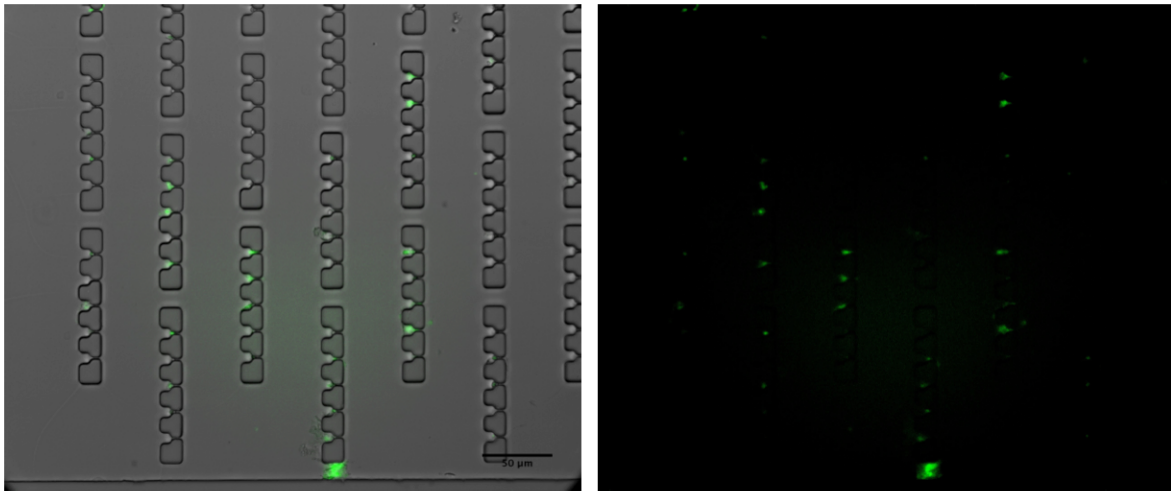
### 5.3.2. On-chip Cell Sorting

We further tested the sorting system using cells from mouse blood. To prepare the blood samples, mouse lung cancer cell lines of both metastatic and non-metastatic nature were grown. Cells were then injected to mouse to induce tumor formation. Blood was then sampled from the mice and lysed with red blood cell (RBC) lysis buffer to remove RBCs. By using FACS screening, we confirmed that the blood samples contained both circulating tumor cells and white blood cells (WBC). We then labeled the WBCs using magnetic beads conjugated with CD45, a pan-leukocyte marker for negative selection.

We prepared microfluidic channels with both cell sorting and capturing regions. The single-cell capture region was customized the small size of mouse CTCs ( $\cong 5 \mu\text{m}$ ). Figure 5.11 shows the process of both steps. Blood samples were flown through the system to deplete host cells and capture target CTCs. To measure the efficiency, we used fluorescence microscope to image the cell capture region (Figure 5.11). The result shows that WBCs were successfully depleted in the sorting region, and CTCs were successfully captured in the capture zone.



**Figure 5.11. Schematics of cell sorting and capture experiment.**



**Figure 5.12. Images of cell capture zone from blood sample tests.**

The structures in the bright field image (left) are capturing sites for mouse circulating tumor cells (CTC). The CTCs have inherent green fluorescence and is shown to be captured. The fluorescent image (right) confirms this observation.



## 5.4. Summary and Discussion

A new magnetic-microfluidic cell sorting and capturing system was developed as a promising tool for CTC detection and analysis. This system features a novel chessboard-like arrangement of alternating magnets. Compared to the previous work, it achieved stronger magnetic force in the microfluidic channel and hence higher sorting efficiency. Moreover, the system can be used with both negative and positive selection strategies. When used with negative selection, the system can be easily integrated with the single cell capturing method developed in the previous chapter for further cellular analysis. In addition, this system provides a simple assembly procedure which can significantly reduce the special training needed for operation.

We anticipate future improvement on this system and its broader use in POC testing. First, the sorting efficiency of the system can be further improved by combing cocktail antibody labeling strategy {Castro et al., 2014, #42059}. The cocktail labeling strategy can achieve higher specificity in binding desired cells in the blood stream. Second, genetic testing can be combined with cell sorting to streamline cancer detection and profiling {Zong et al., 2012, #22745}. Third, automatic magnet assembly method can be developed to further simply the system production.

## Chapter 6 Conclusion & Perspectives

### 6.1. Summary

Providing cost-effective, fast and accurate diagnostic testing to the majority of population in developing world and low-income regions remains a challenging issue. Despite the advancement in technology and medicine, there still lack effective tools to address this challenge.

In this thesis, novel point-of-care (POC) systems for cellular analysis have been introduced. They belong to two categories: optical POC systems and microfluidic POC systems. On the optical side, a lens-free digital holographic system was developed for cell imaging and profiling. Molecular diagnoses were achieved by integrating immunolabeling assay, cloud computing and digital processing. The resulting system enables quantitative cellular analysis and reports not only cancer cell counts but also the expression levels of molecular markers. In addition, a novel compressive sensing method was developed to enhance the resolution to sub-pixel level, which greatly broadened the application of this diagnostic system. This novel algorithm can be also used as a general framework for image reconstruction with nonlinear holographic systems.

Two microfluidic systems were developed for cell sorting and isolation in POC diagnostic tests. The first is a single-cell capture and analysis system customized for lymphoma diagnosis. The system can capture individual lymphoma cells from cerebral spinal fluid, and image both intracellular and extracellular diagnostic markers of these cells. The second is a magnetic-microfluidic system for the isolation of low abundance cells such as CTCs in blood. Using a unique magnetic array design, it achieved stronger magnetic force in the microfluidic

channel and higher sorting efficiency than similar microfluidic-magnetic platforms. Moreover, the system can be used with both negative and positive selection strategies.

## **6.2. Future directions**

These POC systems provides high potential to make diagnostic tests more accessible for low-income populations. We anticipate further improvements in these systems. For the lens-free digital holographic system, multiplexed cellular detection mechanism can be developed based on different optical properties of microbeads; DNA detection can also be incorporated into the system for more comprehensive screening of diseases. The compressive resolution enhancement method can be further combined with computational platforms such as GPU to achieve fast reconstruction results; mathematical transformations such as wavelet transform can be integrated into the algorithm such that more dense samples can be imaged and reconstructed at sub-pixel level. The single-cell capture system for lymphoma analysis can be further improved by combining with sequencing; it can also be combined with portable imaging systems such that it can be used for lymphoma diagnosis in resource-poor settings. The magnetic-microfluidic cell sorting system can be integrated with cocktail antibody labeling for higher sorting efficiency.

In conclusion, the optical and microfluidic POC systems introduced in this thesis provide promising approach for cheaper, faster and more accurate diagnostics. With future developments and improvements, these systems will bring us one step closer to more accessible healthcare globally.

## References

- Abrey, LE, Batchelor, TT, Ferreri, AJ, Gospodarowicz, M, Pulczynski, EJ, Zucca, E, Smith, JR, Korfel, A, Soussain, C, DeAngelis, LM, Neuwelt, EA, O'Neill, BP, Thiel, E, Shenkier, T, Graus, F, van den Bent, M, Seymour, JF, Poortmans, P, Armitage, JO, and Cavalli, F. "Report of an International Workshop to Standardize Baseline Evaluation and Response Criteria for Primary Cns Lymphoma." *J Clin Oncol* 23, no. 22 (2005): 5034-43.
- Agasti, Sarit S, Liong, Monty, Tassa, Carlos, Chung, Hyun Jung, Shaw, Stanley Y, Lee, Hakho, and Weissleder, Ralph. "Supramolecular Host-guest Interaction for Labeling and Detection of Cellular Biomarkers." *Angewandte Chemie International Edition* 51, no. 2 (2012): 450-54.
- Alizadeh, AA, Eisen, MB, Davis, RE, Ma, C, Lossos, IS, Rosenwald, A, Boldrick, JC, Sabet, H, Tran, T, Yu, X, Powell, JI, Yang, L, Marti, GE, Moore, T, Hudson, J Jr, Lu, L, Lewis, DB, Tibshirani, R, Sherlock, G, Chan, WC, Greiner, TC, Weisenburger, DD, Armitage, JO, Warnke, R, Levy, R, Wilson, W, Grever, MR, Byrd, JC, Botstein, D, Brown, PO, and Staudt, LM. "Distinct Types of Diffuse Large B-cell Lymphoma Identified By Gene Expression Profiling." *Nature* 403, no. 6769 (2000): 503-11.
- Antoine, Jean-Claude, Ternynck, The, Rodrigot, Maryvonne, and Avrameas, Stratis. "Lymphoid Cell Fractionation on Magnetic Polyacrylamide-agarose Beads." *Immunochemistry* 15, no. 7 (1978): 443-52.
- Antonini, G, Cox, MC, Montefusco, E, Ferrari, A, Conte, E, Morino, S, Latino, P, Trasimeni, G, and Monarca, B. "Intrathecal Anti-cd20 Antibody: an Effective and Safe Treatment for Leptomeningeal Lymphoma." *J Neurooncol* 81, no. 2 (2007): 197-99.
- Basiji, David A, Ortyrn, William E, Liang, Luchuan, Venkatachalam, Vidya, and Morrissey, Philip. "Cellular Image Analysis and Imaging By Flow Cytometry." *Clinics in laboratory medicine* 27, no. 3 (2007): 653-70.
- Basik, M, Aguilar-Mahecha, A, Rousseau, C, Diaz, Z, Tejpar, S, Spatz, A, Greenwood, CM, and Batist, G. "Biopsies: Next-generation Biospecimens for Tailoring Therapy." *Nat Rev Clin Oncol* 10, no. 8 (2013): 437-50.
- Beaglehole, R, Bonita, R, Alleyne, G, Horton, R, Li, L, Lincoln, P, Mbanya, JC, McKee, M, Moodie, R, Nishtar, S, Piot, P, Reddy, KS, and Stuckler, D. "Un High-level Meeting on Non-communicable Diseases: Addressing Four Questions." *Lancet* 378, no. 9789 (2011): 449-55.
- Bengtsson, E, and Malm, P. "Screening for Cervical Cancer Using Automated Analysis of Pap-smears." *Comput Math Methods Med* 2014 (2014): 842037.
- Bhambhani, A, and Blue, JT. "Lyophilization Strategies for Development of a High-concentration Monoclonal Antibody Formulation: Benefits and Pitfalls." *Am. Pharm. Rev* (2010): 31-38.

Bishara, W, Sikora, U, Mudanyali, O, Su, TW, Yaglidere, O, Luckhart, S, and Ozcan, A. "Holographic Pixel Super-resolution in Portable Lensless on-chip Microscopy Using a Fiber-optic Array." *Lab Chip* 11, no. 7 (2011): 1276-79.

Bishara, Waheb, Sikora, Uzair, Mudanyali, Onur, Su, Ting-Wei, Yaglidere, Oguzhan, Luckhart, Shirley, and Ozcan, Aydogan. "Holographic Pixel Super-resolution in Portable Lensless on-chip Microscopy Using a Fiber-optic Array." *Lab on a Chip* 11, no. 7 (2011a): 1276-79.

Bishara, Waheb, Sikora, Uzair, Mudanyali, Onur, Su, Ting-Wei, Yaglidere, Oguzhan, Luckhart, Shirley, and Ozcan, Aydogan. "Holographic Pixel Super-resolution in Portable Lensless on-chip Microscopy Using a Fiber-optic Array." *Lab on a Chip* 11, no. 7 (2011b): 1276-79.

Bloomfield, IG, Johnston, IH, and Bilston, LE. "Effects of Proteins, Blood Cells and Glucose on the Viscosity of Cerebrospinal Fluid." *Pediatr Neurosurg* 28, no. 5 (1998): 246-51.

Brady, David J, Choi, Kerkil, Marks, Daniel L, Horisaki, Ryoichi, and Lim, Sehoon. "Compressive Holography." *Optics express* 17, no. 15 (2009a): 13040-49.

Brady, David J, Choi, Kerkil, Marks, Daniel L, Horisaki, Ryoichi, and Lim, Sehoon. "Compressive Holography." *Optics express* 17, no. 15 (2009b): 13040-49.

Broyde, A, Boycov, O, Strenov, Y, Okon, E, Shpilberg, O, and Bairey, O. "Role and Prognostic Significance of the Ki-67 Index in Non-hodgkin's Lymphoma." *Am J Hematol* 84, no. 6 (2009): 338-43.

Bruckstein, Alfred M., Donoho, David L., and Elad, Michael. "From Sparse Solutions of Systems of Equations to Sparse Modeling of Signals and Images." *SIAM Rev.* 51, no. 1 (2009): 34-81.

Camilleri-Broet, S, Criniere, E, Broet, P, Delwail, V, Mokhtari, K, Moreau, A, Kujas, M, Raphael, M, Iraqi, W, Sautes-Fridman, C, Colombat, P, Hoang-Xuan, K, and Martin, A. "A Uniform Activated B-cell-like Immunophenotype Might Explain the Poor Prognosis of Primary Central Nervous System Lymphomas: Analysis of 83 Cases." *Blood* 107, no. 1 (2006): 190-96.

Candes, E.J., and Wakin, M.B. "An Introduction to Compressive Sampling." *IEEE Signal Process. Mag.* 25, no. 2 (2008): 21-30.

Candès, Emmanuel J. "Compressive Sampling." 2006.

Castro, CM, Ghazani, AA, Chung, J, Shao, H, Issadore, D, Yoon, TJ, Weissleder, R, and Lee, H. "Miniaturized Nuclear Magnetic Resonance Platform for Detection and Profiling of Circulating Tumor Cells." *Lab Chip* 14, no. 1 (2014): 14-23.

Chan, CP, Mak, WC, Cheung, KY, Sin, KK, Yu, CM, Rainer, TH, and Renneberg, R. "Evidence-based Point-of-care Diagnostics: Current Status and Emerging Technologies." *Annu Rev Anal Chem (Palo Alto Calif)* 6 (2013): 191-211.

Chin, CD, Linder, V, and Sia, SK. "Lab-on-a-chip Devices for Global Health: Past Studies and Future Opportunities." *Lab Chip* 7, no. 1 (2007): 41-57.

Chin, CD, Linder, V, and Sia, SK. "Commercialization of Microfluidic Point-of-care Diagnostic Devices." *Lab Chip* 12, no. 12 (2012a): 2118-34.

Chin, CD, Linder, V, and Sia, SK. "Commercialization of Microfluidic Point-of-care Diagnostic Devices." *Lab Chip* 12, no. 12 (2012b): 2118-34.

Chung, HJ, Castro, CM, Im, H, Lee, H, and Weissleder, R. "A Magneto-DNA Nanoparticle System for Rapid Detection and Phenotyping of Bacteria." *Nat Nanotechnol* 8, no. 5 (2013): 369-75.

Chung, J, Issadore, D, Ullal, A, Lee, K, Weissleder, R, and Lee, H. "Rare Cell Isolation and Profiling on a Hybrid Magnetic/size-sorting Chip." *Biomicrofluidics* 7, no. 5 (2013): 54107.

Coskun, AF, Su, TW, and Ozcan, A. "Wide Field-of-view Lens-free Fluorescent Imaging on a Chip." *Lab Chip* 10, no. 7 (2010): 824-27.

Cristofanilli, Massimo, Budd, G Thomas, Ellis, Matthew J, Stopeck, Alison, Matera, Jeri, Miller, M Craig, Reuben, James M, Doyle, Gerald V, Allard, W Jeffrey, and Terstappen, Leon WMM. "Circulating Tumor Cells, Disease Progression, and Survival in Metastatic Breast Cancer." *New England Journal of Medicine* 351, no. 8 (2004a): 781-91.

Cristofanilli, Massimo, Budd, G Thomas, Ellis, Matthew J, Stopeck, Alison, Matera, Jeri, Miller, M Craig, Reuben, James M, Doyle, Gerald V, Allard, W Jeffrey, and Terstappen, Leon WMM. "Circulating Tumor Cells, Disease Progression, and Survival in Metastatic Breast Cancer." *New England Journal of Medicine* 351, no. 8 (2004b): 781-91.

Daar, Abdallah S, Singer, Peter A, Persad, Deepa Leah, Pramming, Stig K, Matthews, David R, Beaglehole, Robert, Bernstein, Alan, Borysiewicz, Leszek K, Colagiuri, Stephen, and Ganguly, Nirmal. "Grand Challenges in Chronic Non-communicable Diseases." *Nature* 450, no. 7169 (2007): 494-96.

Dave, SS, Fu, K, Wright, GW, Lam, LT, Kluin, P, Boerma, EJ, Greiner, TC, Weisenburger, DD, Rosenwald, A, Ott, G, Muller-Hermelink, HK, Gascoyne, RD, Delabie, J, Rimsza, LM, Braziel, RM, Grogan, TM, Campo, E, Jaffe, ES, Dave, BJ, Sanger, W, Bast, M, Vose, JM, Armitage, JO, Connors, JM, Smeland, EB, Kvaloy, S, Holte, H, Fisher, RI, Miller, TP, Montserrat, E, Wilson, WH, Bahl, M, Zhao, H, Yang, L, Powell, J, Simon, R, Chan, WC, and Staudt, LM. "Molecular Diagnosis of Burkitt's Lymphoma." *N Engl J Med* 354, no. 23 (2006): 2431-42.

De Giorgi, Vincenzo, Pinzani, Pamela, Salvianti, Francesca, Panelos, John, Paglierani, Milena, Janowska, Agata, Grazzini, Marta, Wechsler, Janine, Orlando, Claudio, and Santucci, Marco. "Application of a Filtration-and Isolation-by-size Technique for the Detection of Circulating Tumor Cells in Cutaneous Melanoma." *Journal of Investigative Dermatology* 130, no. 10 (2010): 2440-47.

de Graaf, MT, Smitt, PA, Luitwieler, RL, van Velzen, C, van den Broek, PD, Kraan, J, and Gratama, JW. "Central Memory Cd4+ T Cells Dominate the Normal Cerebrospinal Fluid." *Cytometry B Clin Cytom* 80, no. 1 (2011): 43-50.

Deng, Tao, Whitesides, George M, Radhakrishnan, Mala, Zabow, Gary, and Prentiss, Mara. "Manipulation of Magnetic Microbeads in Suspension Using Micromagnetic Systems Fabricated With Soft Lithography." *Applied physics letters* 78, no. 12 (2001): 1775-77.

Dux, R, Kindler-Rohrborn, A, Annas, M, Faustmann, P, Lennartz, K, and Zimmermann, CW. "A Standardized Protocol for Flow Cytometric Analysis of Cells Isolated From Cerebrospinal Fluid." *J Neurol Sci* 121, no. 1 (1994): 74-78.

Fienup, J.R. "Phase Retrieval Algorithms: a Comparison." *Applied optics* 21, no. 15 (1982): 2758-69.

Fleuren, ED, Versleijen-Jonkers, YM, Heskamp, S, van Herpen, CM, Oyen, WJ, van der Graaf, WT, and Boerman, OC. "Theranostic Applications of Antibodies in Oncology." *Mol Oncol* (2014):

Fung, J., Martin, K.E., Perry, R.W., Kaz, D.M., McGorty, R., and Manoharan, V.N. "Measuring Translational, Rotational, and Vibrational Dynamics in Colloids With Digital Holographic Microscopy." *Optics express* 19, no. 9 (2011): 8051-65.

Garcia-Sucerquia, J., Xu, W., Jericho, S.K., Jericho, M.H., and Kreuzer, H.J. "4-d Imaging of Fluid Flow With Digital in-line Holographic Microscopy." *Optik - International Journal for Light and Electron Optics* 119, no. 9 (2008): 419-23.

Garcia-Sucerquia, J., Xu, W., Jericho, S.K., Klages, P., Jericho, M.H., and Kreuzer, H.J. "Digital in-line Holographic Microscopy." *Applied optics* 45, no. 5 (2006a): 836-50.

Garcia-Sucerquia, J., Xu, W., Jericho, S.K., Klages, P., Jericho, M.H., and Kreuzer, H.J. "Digital in-line Holographic Microscopy." *Applied optics* 45, no. 5 (2006b): 836-50.

Gazit, Snir, Szameit, Alexander, Eldar, Yonina C, and Segev, Mordechai. "Super-resolution and Reconstruction of Sparse Sub-wavelength Images." *Optics express* 17, no. 26 (2009): 23920-46.

Gill, S, Herbert, KE, Prince, HM, Wolf, MM, Wirth, A, Ryan, G, Carney, DA, Ritchie, DS, Davies, JM, and Seymour, JF. "Mantle Cell Lymphoma With Central Nervous System Involvement: Frequency and Clinical Features." *Br J Haematol* 147, no. 1 (2009): 83-88.

Gottlieb, Michael S, Schroff, Robert, Schanker, Howard M, Weisman, Joel D, Fan, Peng Thim, Wolf, Robert A, and Saxon, Andrew. "Pneumocystis Carinii Pneumonia and Mucosal Candidiasis in Previously Healthy Homosexual Men: Evidence of a New Acquired Cellular Immunodeficiency." *New England Journal of Medicine* 305, no. 24 (1981): 1425-31.

Gradilone, Angela, Raimondi, Cristina, Nicolazzo, Chiara, Petracca, Arianna, Gandini, Orietta, Vincenzi, Bruno, Naso, Giuseppe, Aglianò, Anna Maria, Cortesi, Enrico, and Gazzaniga, Paola. "Circulating Tumour Cells Lacking Cytokeratin in Breast Cancer: the Importance of Being Mesenchymal." *Journal of cellular and molecular medicine* 15, no. 5 (2011): 1066-70.

Greenbaum, A, Luo, W, Su, TW, Gorocs, Z, Xue, L, Isikman, SO, Coskun, AF, Mudanyali, O, and Ozcan, A. "Imaging Without Lenses: Achievements and Remaining Challenges of Wide-field on-chip Microscopy." *Nat Methods* 9, no. 9 (2012a): 889-95.

- Greenbaum, A, Luo, W, Su, TW, Gorocs, Z, Xue, L, Isikman, SO, Coskun, AF, Mudanyali, O, and Ozcan, A. "Imaging Without Lenses: Achievements and Remaining Challenges of Wide-field on-chip Microscopy." *Nat Methods* 9, no. 9 (2012b): 889-95.
- Greenbaum, Alon, Akbari, Najva, Feizi, Alborz, Luo, Wei, and Ozcan, Aydogan. "Field-portable Pixel Super-resolution Colour Microscope." *PloS one* 8, no. 9 (2013): e76475.
- Greenbaum, Alon, Luo, Wei, Khademhosseinieh, Bahar, Su, Ting-Wei, Coskun, Ahmet F., and Ozcan, Aydogan. "Increased Space-bandwidth Product in Pixel Super-resolved Lensfree on-chip Microscopy." *Sci. Rep.* 3 (2013):
- Gubala, V, Harris, LF, Ricco, AJ, Tan, MX, and Williams, DE. "Point of Care Diagnostics: Status and Future." *Anal Chem* 84, no. 2 (2012): 487-515.
- Gurel, B, Iwata, T, Koh, CM, Jenkins, RB, Lan, F, Van Dang, C, Hicks, JL, Morgan, J, Cornish, TC, Sutcliffe, S, Isaacs, WB, Luo, J, and De Marzo, AM. "Nuclear Myc Protein Overexpression is an Early Alteration in Human Prostate Carcinogenesis." *Mod Pathol* 21, no. 9 (2008): 1156-67.
- Gurkan, UA, Moon, S, Geckil, H, Xu, F, Wang, S, Lu, TJ, and Demirci, U. "Miniaturized Lensless Imaging Systems for Cell and Microorganism Visualization in Point-of-care Testing." *Biotechnol J* 6, no. 2 (2011): 138-49.
- Hans, CP, Weisenburger, DD, Greiner, TC, Gascoyne, RD, Delabie, J, Ott, G, Muller-Hermelink, HK, Campo, E, Braziel, RM, Jaffe, ES, Pan, Z, Farinha, P, Smith, LM, Falini, B, Banham, AH, Rosenwald, A, Staudt, LM, Connors, JM, Armitage, JO, and Chan, WC. "Confirmation of the Molecular Classification of Diffuse Large B-cell Lymphoma By Immunohistochemistry Using a Tissue Microarray." *Blood* 103, no. 1 (2004): 275-82.
- Haun, JB, Castro, CM, Wang, R, Peterson, VM, Marinelli, BS, Lee, H, and Weissleder, R. "Micro-nmr for Rapid Molecular Analysis of Human Tumor Samples." *Sci Transl Med* 3, no. 71 (2011): 71ra16.
- Haun, Jered B, Devaraj, Neal K, Hilderbrand, Scott A, Lee, Hakho, and Weissleder, Ralph. "Bioorthogonal Chemistry Amplifies Nanoparticle Binding and Enhances the Sensitivity of Cell Detection." *Nature nanotechnology* 5, no. 9 (2010): 660-65.
- Hegde, U, Filie, A, Little, RF, Janik, JE, Grant, N, Steinberg, SM, Dunleavy, K, Jaffe, ES, Abati, A, Stetler-Stevenson, M, and Wilson, WH. "High Incidence of Occult Leptomeningeal Disease Detected By Flow Cytometry in Newly Diagnosed Aggressive B-cell Lymphomas At Risk for Central Nervous System Involvement: the Role of Flow Cytometry Versus Cytology." *Blood* 105, no. 2 (2005): 496-502.
- Hiraga, J, Tomita, A, Sugimoto, T, Shimada, K, Ito, M, Nakamura, S, Kiyoi, H, Kinoshita, T, and Naoe, T. "Down-regulation of Cd20 Expression in B-cell Lymphoma Cells After Treatment With Rituximab-containing Combination Chemotherapies: Its Prevalence and Clinical Significance." *Blood* 113, no. 20 (2009): 4885-93.



Hoffmann, Jochen, Mark, Daniel, Lutz, Sascha, Zengerle, Roland, and von Stetten, Felix. "Pre-storage of Liquid Reagents in Glass Ampoules for DNA Extraction on a Fully Integrated Lab-on-a-chip Cartridge." *Lab on a Chip* 10, no. 11 (2010): 1480-84.

Hosokawa, Masahito, Hayata, Taishi, Fukuda, Yorikane, Arakaki, Atsushi, Yoshino, Tomoko, Tanaka, Tsuyoshi, and Matsunaga, Tadashi. "Size-selective Microcavity Array for Rapid and Efficient Detection of Circulating Tumor Cells." *Analytical chemistry* 82, no. 15 (2010): 6629-35.

Huang, Shichu, Do, Jaephil, Mahalanabis, Madhumita, Fan, Andy, Zhao, Lei, Jepeal, Lisa, Singh, Satish K, and Klapperich, Catherine M. "Low Cost Extraction and Isothermal Amplification of DNA for Infectious Diarrhea Diagnosis." *PloS one* 8, no. 3 (2013): e60059.

Im, H, Shao, H, Park, YI, Peterson, VM, Castro, CM, Weissleder, R, and Lee, H. "Label-free Detection and Molecular Profiling of Exosomes With a Nano-plasmonic Sensor." *Nat Biotechnol* 32, no. 5 (2014): 490-95.

Inglis, David W, Riehn, Robert, Sturm, James C, and Austin, Robert H. "Microfluidic High Gradient Magnetic Cell Separation." *Journal of Applied Physics* 99, no. 8 (2006): 08K101.

Isikman, SO, Sencan, I, Mudanyali, O, Bishara, W, Oztoprak, C, and Ozcan, A. "Color and Monochrome Lensless on-chip Imaging of Caenorhabditis Elegans Over a Wide Field-of-view." *Lab Chip* 10, no. 9 (2010): 1109-12.

Issadore, D, Chung, J, Shao, H, Liong, M, Ghazani, AA, Castro, CM, Weissleder, R, and Lee, H. "Ultrasensitive Clinical Enumeration of Rare Cells Ex Vivo Using a Micro-hall Detector." *Sci Transl Med* 4, no. 141 (2012): 141ra92.

Issadore, D, Park, YI, Shao, H, Min, C, Lee, K, Liong, M, Weissleder, R, and Lee, H. "Magnetic Sensing Technology for Molecular Analyses." *Lab Chip* 14, no. 14 (2014): 2385-97.

Issadore, D, Shao, H, Chung, J, Newton, A, Pittet, M, Weissleder, R, and Lee, H. "Self-assembled Magnetic Filter for Highly Efficient Immunomagnetic Separation." *Lab Chip* 11, no. 1 (2011): 147-51.

Jericho, Manfred H., and Kreuzer Jürgen, H. "Point Source Digital in-line Holographic Microscopy Digital in-line Holographic Microscopy." edited by Pietro Ferraro, Adam Wax, and Zeev Zalevsky, 3-30. Berlin, Heidelberg: Springer Berlin Heidelberg, 2011a.

Jericho, Manfred H., and Kreuzer Jürgen, H. "Point Source Digital in-line Holographic Microscopy Digital in-line Holographic Microscopy." edited by Pietro Ferraro, Adam Wax, and Zeev Zalevsky, 3-30. Berlin, Heidelberg: Springer Berlin Heidelberg, 2011b.

Jiang, Li, Mancuso, Matthew, Lu, Zhengda, Akar, Gunkut, Cesarman, Ethel, and Erickson, David. "Solar Thermal Polymerase Chain Reaction for Smartphone-assisted Molecular Diagnostics." *Scientific reports* 4 (2014): 4137.

Johnson, NA, Boyle, M, Bashashati, A, Leach, S, Brooks-Wilson, A, Sehn, LH, Chhanabhai, M, Brinkman, RR, Connors, JM, Weng, AP, and Gascoyne, RD. "Diffuse Large B-cell Lymphoma:

Reduced Cd20 Expression is Associated With an Inferior Survival.” *Blood* 113, no. 16 (2009): 3773-80.

Kim, SB, Bae, H, Cha, JM, Moon, SJ, Dokmeci, MR, Cropek, DM, and Khademhosseini, A. “A Cell-based Biosensor for Real-time Detection of Cardiotoxicity Using Lensfree Imaging.” *Lab on a Chip* 11, no. 10 (2011): 1801-07.

Kim, Unyoung, and Soh, H Tom. “Simultaneous Sorting of Multiple Bacterial Targets Using Integrated Dielectrophoretic–magnetic Activated Cell Sorter.” *Lab on a Chip* 9, no. 16 (2009): 2313-18.

Kleine, TO, Albrecht, J, and Zofel, P. “Flow Cytometry of Cerebrospinal Fluid (csf) Lymphocytes: Alterations of Blood/csf Ratios of Lymphocyte Subsets in Inflammation Disorders of Human Central Nervous System (cns).” *Clin Chem Lab Med* 37, no. 3 (1999): 231-41.

Korfel, A, Weller, M, Martus, P, Roth, P, Klasen, HA, Roeth, A, Rauch, M, Hertenstein, B, Fischer, T, Hundsberger, T, Leithauser, M, Birnbaum, T, Kirchen, H, Mergenthaler, HG, Schubert, J, Berdel, W, Birkmann, J, Hummel, M, Thiel, E, and Fischer, L. “Prognostic Impact of Meningeal Dissemination in Primary Cns Lymphoma (pcnsl): Experience From the G-pcnsl-sg1 Trial.” *Ann Oncol* 23, no. 9 (2012): 2374-80.

Kreis, T.M. “Frequency Analysis of Digital Holography With Reconstruction By Convolution.” *Optical Engineering* 41, no. 8 (2002): 1829-39.

Latychevskiaia, Tatiana, and Fink, Hans-Werner. “Solution to the Twin Image Problem in Holography.” *Phys. Rev. Lett.* 98, no. 23 (2007): 233901.

Lee, H, Sun, E, Ham, D, and Weissleder, R. “Chip-nmr Biosensor for Detection and Molecular Analysis of Cells.” *Nat Med* 14, no. 8 (2008a): 869-74.

Lee, H, Sun, E, Ham, D, and Weissleder, R. “Chip-nmr Biosensor for Detection and Molecular Analysis of Cells.” *Nat Med* 14, no. 8 (2008b): 869-74.

Lee, SA, Leitao, R, Zheng, G, Yang, S, Rodriguez, A, and Yang, C. “Color Capable Sub-pixel Resolving Optofluidic Microscope and Its Application to Blood Cell Imaging for Malaria Diagnosis.” *PLoS One* 6, no. 10 (2011): e26127.

Lee, SA, Zheng, G, Mukherjee, N, and Yang, C. “On-chip Continuous Monitoring of Motile Microorganisms on an Epetri Platform.” *Lab Chip* 12, no. 13 (2012): 2385-90.

Lenz, G, Wright, GW, Emre, NC, Kohlhammer, H, Dave, SS, Davis, RE, Carty, S, Lam, LT, Shaffer, AL, Xiao, W, Powell, J, Rosenwald, A, Ott, G, Muller-Hermelink, HK, Gascoyne, RD, Connors, JM, Campo, E, Jaffe, ES, Delabie, J, Smeland, EB, Rimsza, LM, Fisher, RI, Weisenburger, DD, Chan, WC, and Staudt, LM. “Molecular Subtypes of Diffuse Large B-cell Lymphoma Arise By Distinct Genetic Pathways.” *Proc Natl Acad Sci U S A* 105, no. 36 (2008): 13520-25.

Lewis, Nancy I., Xu, Wenbo, Jericho, Stefan K., Kreuzer, Hans J., Jericho, Manfred H., and Cembella, Allan D. “Swimming Speed of Three Species of *Alexandrium* (dinophyceae) as Determined By Digital in-line Holography.” *Phycologia* 45, no. 1 (2006): 61-70.

- Liang, R, Chiu, E, and Loke, SL. "Secondary Central Nervous System Involvement By Non-hodgkin's Lymphoma: the Risk Factors." *Hematol Oncol* 8, no. 3 (1990): 141-45.
- Lin, Henry K, Zheng, Siyang, Williams, Anthony J, Balic, Marija, Groshen, Susan, Scher, Howard I, Fleisher, Martin, Stadler, Walter, Datar, Ram H, and Tai, Yu-Chong. "Portable Filter-based Microdevice for Detection and Characterization of Circulating Tumor Cells." *Clinical Cancer Research* 16, no. 20 (2010): 5011-18.
- Liu, Changchun, Mauk, Michael G, Hart, Robert, Qiu, Xianbo, and Bau, Haim H. "A Self-heating Cartridge for Molecular Diagnostics." *Lab on a Chip* 11, no. 16 (2011): 2686-92.
- Lossos, IS, Czerwinski, DK, Alizadeh, AA, Wechser, MA, Tibshirani, R, Botstein, D, and Levy, R. "Prediction of Survival in Diffuse Large-b-cell Lymphoma Based on the Expression of Six Genes." *N Engl J Med* 350, no. 18 (2004): 1828-37.
- Lossos, IS, and Morgenzstern, D. "Prognostic Biomarkers in Diffuse Large B-cell Lymphoma." *J Clin Oncol* 24, no. 6 (2006): 995-1007.
- Mabey, D, Peeling, RW, Ustianowski, A, and Perkins, MD. "Diagnostics for the Developing World." *Nat Rev Microbiol* 2, no. 3 (2004): 231-40.
- Maheswaran, Shyamala, Sequist, Lecia V, Nagrath, Sunitha, Ulkus, Lindsey, Brannigan, Brian, Collura, Chey V, Inserra, Elizabeth, Diederichs, Sven, Iafrate, A John, and Bell, Daphne W. "Detection of Mutations in Egfr in Circulating Lung-cancer Cells." *New England Journal of Medicine* 359, no. 4 (2008): 366-77.
- Marim, M, Angelini, E, Olivo-Marin, JC, and Atlan, M. "Off-axis Compressed Holographic Microscopy in Low-light Conditions." *Opt Lett* 36, no. 1 (2011): 79-81.
- McElhinney, Conor P, McDonald, John B, Castro, Albertina, Frauel, Yann, Javidi, Bahram, and Naughton, Thomas J. "Depth-independent Segmentation of Macroscopic Three-dimensional Objects Encoded in Single Perspectives of Digital Holograms." *Optics letters* 32, no. 10 (2007): 1229-31.
- Miyoshi, H, Arakawa, F, Sato, K, Kimura, Y, Kiyasu, J, Takeuchi, M, Yoshida, M, Ichikawa, A, Ishibashi, Y, Nakamura, Y, Nakashima, S, Niino, D, Sugita, Y, and Ohshima, K. "Comparison of Cd20 Expression in B-cell Lymphoma Between Newly Diagnosed, Untreated Cases and Those After Rituximab Treatment." *Cancer Sci* 103, no. 8 (2012): 1567-73.
- Mudanyali, O, Oztoprak, C, Tseng, D, Erlinger, A, and Ozcan, A. "Detection of Waterborne Parasites Using Field-portable and Cost-effective Lensfree Microscopy." *Lab Chip* 10, no. 18 (2010): 2419-23.
- Mudanyali, O, Tseng, D, Oh, C, Isikman, SO, Sencan, I, Bishara, W, Oztoprak, C, Seo, S, Khademhosseini, B, and Ozcan, A. "Compact, Light-weight and Cost-effective Microscope Based on Lensless Incoherent Holography for Telemedicine Applications." *Lab Chip* 10, no. 11 (2010): 1417-28.
- Mudanyali, Onur, Bishara, Waheb, and Ozcan, Aydogan. "Lensfree Super-resolution Holographic Microscopy Using Wetting Films on a Chip." *Optics express* 19, no. 18 (2011): 17378-89.

Mudanyali, Onur, Erlinger, Anthony, Seo, Sungkyu, Su, Ting-Wei, Tseng, Derek, and Ozcan, Aydogan. “Lensless on-chip Imaging of Cells Provides a New Tool for High-throughput Cell-biology and Medical Diagnostics.” *JoVE* 34 (2009):

Mudanyali, Onur, McLeod, Euan, Luo, Wei, Greenbaum, Alon, Coskun, Ahmet F, Hennequin, Yves, Allier, Cédric P, and Ozcan, Aydogan. “Wide-field Optical Detection of Nanoparticles Using on-chip Microscopy and Self-assembled Nanolenses.” *Nature photonics* 7, no. 3 (2013): 247-54.

Myers, FB, and Lee, LP. “Innovations in Optical Microfluidic Technologies for Point-of-care Diagnostics.” *Lab Chip* 8, no. 12 (2008): 2015-31.

Nagrath, S, Sequist, LV, Maheswaran, S, Bell, DW, Irimia, D, Ulkus, L, Smith, MR, Kwak, EL, Digumarthy, S, Muzikansky, A, Ryan, P, Balis, UJ, Tompkins, RG, Haber, DA, and Toner, M. “Isolation of Rare Circulating Tumour Cells in Cancer Patients By Microchip Technology.” *Nature* 450, no. 7173 (2007): 1235-39.

Nagrath, Sunitha, Sequist, Lecia V, Maheswaran, Shyamala, Bell, Daphne W, Irimia, Daniel, Ulkus, Lindsey, Smith, Matthew R, Kwak, Eunice L, Digumarthy, Subba, and Muzikansky, Alona. “Isolation of Rare Circulating Tumour Cells in Cancer Patients By Microchip Technology.” *Nature* 450, no. 7173 (2007): 1235-39.

Narayan, KM Venkat, Ali, Mohammed K, del Rio, Carlos, Koplan, Jeffrey P, and Curran, James. “Global Noncommunicable Diseases—lessons From the Hiv-aids Experience.” *New England Journal of Medicine* 365, no. 10 (2011): 876-78.

Ojesina, AI, Lichtenstein, L, Freeman, SS, Peadarallu, CS, Imaz-Rosshandler, I, Pugh, TJ, Cherniack, AD, Ambrogio, L, Cibulskis, K, Bertelsen, B, Romero-Cordoba, S, Trevino, V, Vazquez-Santillan, K, Guadarrama, AS, Wright, AA, Rosenberg, MW, Duke, F, Kaplan, B, Wang, R, Nickerson, E, Walline, HM, Lawrence, MS, Stewart, C, Carter, SL, McKenna, A, Rodriguez-Sanchez, IP, Espinosa-Castilla, M, Woie, K, Bjorge, L, Wik, E, Halle, MK, Hoivik, EA, Krakstad, C, Gabino, NB, Gomez-Macias, GS, Valdez-Chapa, LD, Garza-Rodriguez, ML, Maytorena, G, Vazquez, J, Rodea, C, Cravioto, A, Cortes, ML, Greulich, H, Crum, CP, Neuberger, DS, Hidalgo-Miranda, A, Escareno, CR, Akshen, LA, Carey, TE, Vintermyr, OK, Gabriel, SB, Barrera-Saldana, HA, Melendez-Zajgla, J, Getz, G, Salvesen, HB, and Meyerson, M. “Landscape of Genomic Alterations in Cervical Carcinomas.” *Nature* 506, no. 7488 (2014): 371-75.

Pamme, Nicole, and Wilhelm, Claire. “Continuous Sorting of Magnetic Cells Via on-chip Free-flow Magnetophoresis.” *Lab on a Chip* 6, no. 8 (2006): 974-80.

Peterson, VM, Castro, CM, Chung, J, Miller, NC, Ullal, AV, Castano, MD, Penson, RT, Lee, H, Birrer, MJ, and Weissleder, R. “Ascites Analysis By a Microfluidic Chip Allows Tumor-cell Profiling.” *Proc Natl Acad Sci U S A* 110, no. 51 (2013a): E4978-86.

Peterson, VM, Castro, CM, Chung, J, Miller, NC, Ullal, AV, Castano, MD, Penson, RT, Lee, H, Birrer, MJ, and Weissleder, R. “Ascites Analysis By a Microfluidic Chip Allows Tumor-cell Profiling.” *Proc Natl Acad Sci U S A* 110, no. 51 (2013b): E4978-86.

- Ponader, S, and Burger, JA. "Bruton's Tyrosine Kinase: From X-linked Agammaglobulinemia Toward Targeted Therapy for B-cell Malignancies." *J Clin Oncol* 32, no. 17 (2014): 1830-39.
- Quijano, S, Lopez, A, Manuel Sancho, J, Panizo, C, Deben, G, Castilla, C, Antonio Garcia-Vela, J, Salar, A, Alonso-Vence, N, Gonzalez-Barca, E, Penalver, FJ, Plaza-Villa, J, Morado, M, Garcia-Marco, J, Arias, J, Briones, J, Ferrer, S, Capote, J, Nicolas, C, and Orfao, A. "Identification of Leptomeningeal Disease in Aggressive B-cell Non-hodgkin's Lymphoma: Improved Sensitivity of Flow Cytometry." *J Clin Oncol* 27, no. 9 (2009): 1462-69.
- Rahal, R, Frick, M, Romero, R, Korn, JM, Kridel, R, Chan, FC, Meissner, B, Bhang, HE, Ruddy, D, Kauffmann, A, Farsidjani, A, Derti, A, Rakiec, D, Naylor, T, Pfister, E, Kovats, S, Kim, S, Dietze, K, Dorken, B, Steidl, C, Tzankov, A, Hummel, M, Monahan, J, Morrissey, MP, Fritsch, C, Sellers, WR, Cooke, VG, Gascoyne, RD, Lenz, G, and Stegmeier, F. "Pharmacological and Genomic Profiling Identifies Nf-kappab-targeted Treatment Strategies for Mantle Cell Lymphoma." *Nat Med* 20, no. 1 (2014): 87-92.
- Rivenson, Yair, Stern, Adrian, and Javidi, Bahram. "Overview of Compressive Sensing Techniques Applied in Holography [invited]." *Applied optics* 52, no. 1 (2013): A423-32.
- Rivenson, Yair, Stern, Adrian, and Rosen, Joseph. "Compressive Multiple View Projection Incoherent Holography." *Optics express* 19, no. 7 (2011): 6109-18.
- Rubenstein, JL, Fridlyand, J, Shen, A, Aldape, K, Ginzinger, D, Batchelor, T, Treseler, P, Berger, M, McDermott, M, Prados, M, Karch, J, Okada, C, Hyun, W, Parikh, S, Haqq, C, and Shuman, M. "Gene Expression and Angiotropism in Primary Cns Lymphoma." *Blood* 107, no. 9 (2006): 3716-23.
- Schabet, M. "Epidemiology of Primary Cns Lymphoma." *J Neurooncol* 43, no. 3 (1999): 199-201.
- Schiffman, M, and Solomon, D. "Clinical Practice. Cervical-cancer Screening With Human Papillomavirus and Cytologic Cotesting." *N Engl J Med* 369, no. 24 (2013): 2324-31.
- Schroers, R, Baraniskin, A, Heute, C, Vorgerd, M, Brunn, A, Kuhnenn, J, Kowoll, A, Alekseyev, A, Schmiegel, W, Schlegel, U, Deckert, M, and Pels, H. "Diagnosis of Leptomeningeal Disease in Diffuse Large B-cell Lymphomas of the Central Nervous System By Flow Cytometry and Cytopathology." *Eur J Haematol* 85, no. 6 (2010): 520-28.
- Seo, S, Isikman, SO, Sencan, I, Mudanyali, O, Su, TW, Bishara, W, Erlinger, A, and Ozcan, A. "High-throughput Lens-free Blood Analysis on a Chip." *Anal Chem* 82, no. 11 (2010): 4621-27.
- Seo, S, Su, TW, Tseng, DK, Erlinger, A, and Ozcan, A. "Lensfree Holographic Imaging for on-chip Cytometry and Diagnostics." *Lab Chip* 9, no. 6 (2009): 777-87.
- Stott, Shannon L, Lee, Richard J, Nagrath, Sunitha, Yu, Min, Miyamoto, David T, Ulkus, Lindsey, Inserra, Elizabeth J, Ulman, Matthew, Springer, Simeon, and Nakamura, Zev. "Isolation and Characterization of Circulating Tumor Cells From Patients With Localized and Metastatic Prostate Cancer." *Science translational medicine* 2, no. 25 (2010): 25ra23-25ra23.

- Su, Ting-Wei, Choi, Inkyum, Feng, Jiawen, Huang, Calvin, McLeod, Euan, and Ozcan, Aydogan. "Sperm Trajectories Form Chiral Ribbons." *Scientific reports* 3 (2013): 1664.
- Sun, T, Holmes, D, Gawad, S, Green, NG, and Morgan, H. "High Speed Multi-frequency Impedance Analysis of Single Particles in a Microfluidic Cytometer Using Maximum Length Sequences." *Lab Chip* 7, no. 8 (2007): 1034-40.
- Szameit, A, Shechtman, Y, Osherovich, E, Bullklich, E, Sidorenko, P, Dana, H, Steiner, S, Kley, EB, Gazit, S, Cohen-Hyams, T, Shoham, S, Zibulevsky, M, Yavneh, I, Eldar, YC, Cohen, O, and Segev, M. "Sparsity-based Single-shot Subwavelength Coherent Diffractive Imaging." *Nat Mater* 11, no. 5 (2012): 455-59.
- Trimble, Edward L. "Global Cooperation in Gynecologic Cancer." *Journal of gynecologic oncology* 21, no. 1 (2010): 1-2.
- Turetsky, A, Kim, E, Kohler, RH, Miller, MA, and Weissleder, R. "Single Cell Imaging of Bruton's Tyrosine Kinase Using an Irreversible Inhibitor." *Sci Rep* 4 (2014): 4782.
- Ullal, AV, Peterson, V, Agasti, SS, Tuang, S, Juric, D, Castro, CM, and Weissleder, R. "Cancer Cell Profiling By Barcoding Allows Multiplexed Protein Analysis in Fine-needle Aspirates." *Sci Transl Med* 6, no. 219 (2014): 219ra9.
- van Besien, K, Ha, CS, Murphy, S, McLaughlin, P, Rodriguez, A, Amin, K, Forman, A, Romaguera, J, Hagemester, F, Younes, A, Bachier, C, Sarris, A, Sobocinski, KS, Cox, JD, and Cabanillas, F. "Risk Factors, Treatment, and Outcome of Central Nervous System Recurrence in Adults With Intermediate-grade and Immunoblastic Lymphoma." *Blood* 91, no. 4 (1998): 1178-84.
- Varmus, Harold, and Trimble, Edward L. "Integrating Cancer Control Into Global Health." *Science Translational Medicine* 3, no. 101 (2011): 101cm28-101cm28.
- Villano, JL, Koshy, M, Shaikh, H, Dolecek, TA, and McCarthy, BJ. "Age, Gender, and Racial Differences in Incidence and Survival in Primary Cns Lymphoma." *Br J Cancer* 105, no. 9 (2011): 1414-18.
- Weston, CL, Glantz, MJ, and Connor, JR. "Detection of Cancer Cells in the Cerebrospinal Fluid: Current Methods and Future Directions." *Fluids Barriers CNS* 8, no. 1 (2011): 14.
- Wilson, WH, Bromberg, JE, Stetler-Stevenson, M, Steinberg, SM, Martin-Martin, L, Muniz, C, Sancho, JM, Caballero, MD, Davidis, MA, Brooimans, RA, Sanchez-Gonzalez, B, Salar, A, Gonzalez-Barca, E, Ribera, JM, Shovlin, M, Filie, A, Dunleavy, K, Mehrling, T, Spina, M, and Orfao, A. "Detection and Outcome of Occult Leptomeningeal Disease in Diffuse Large B-cell Lymphoma and Burkitt Lymphoma." *Haematologica* (2014):
- Xia, Nan, Hunt, Tom P, Mayers, Brian T, Alsberg, Eben, Whitesides, George M, Westervelt, Robert M, and Ingber, Donald E. "Combined Microfluidic-micromagnetic Separation of Living Cells in Continuous Flow." *Biomedical Microdevices* 8, no. 4 (2006): 299-308.

- Xu, Wenbo, Jericho, MH, Meinertzhagen, IA, and Kreuzer, HJ. "Digital in-line Holography for Biological Applications." *Proceedings of the National Academy of Sciences* 98, no. 20 (2001): 11301-05.
- Yager, P, Domingo, GJ, and Gerdes, J. "Point-of-care Diagnostics for Global Health." *Annu Rev Biomed Eng* 10 (2008): 107-44.
- Yager, P, Edwards, T, Fu, E, Helton, K, Nelson, K, Tam, MR, and Weigl, BH. "Microfluidic Diagnostic Technologies for Global Public Health." *Nature* 442, no. 7101 (2006): 412-18.
- Younes, A, and Berry, DA. "From Drug Discovery to Biomarker-driven Clinical Trials in Lymphoma." *Nat Rev Clin Oncol* 9, no. 11 (2012): 643-53.
- Zborowski, Maciej, and Jeffrey J Chalmers. *Magnetic Cell Separation*. Vol. 32, Elsevier, 2011.
- Zheng, G, Lee, SA, Antebi, Y, Elowitz, MB, and Yang, C. "The Epetri Dish, an on-chip Cell Imaging Platform Based on Subpixel Perspective Sweeping Microscopy (spsm)." *Proc Natl Acad Sci U S A* 108, no. 41 (2011a): 16889-94.
- Zheng, G, Lee, SA, Antebi, Y, Elowitz, MB, and Yang, C. "The Epetri Dish, an on-chip Cell Imaging Platform Based on Subpixel Perspective Sweeping Microscopy (spsm)." *Proc Natl Acad Sci U S A* 108, no. 41 (2011b): 16889-94.
- Zheng, G, Lee, SA, Yang, S, and Yang, C. "Sub-pixel Resolving Optofluidic Microscope for on-chip Cell Imaging." *Lab Chip* 10, no. 22 (2010): 3125-29.
- Zheng, Guoan, Horstmeyer, Roarke, and Yang, Changhuei. "Wide-field, High-resolution Fourier Ptychographic Microscopy." *Nature Photonics* 7, no. 9 (2013): 739-45.
- Zheng, Guoan, lee, Seung Ah, Antebi, Yaron, Elowitz, Michael B., Yang, Changhuei, Xu, W., Jericho, S.K., Jericho, M.H., and Kreuzer, H.J. "The Epetri Dish, an on-chip Cell Imaging Platform Based on Subpixel Perspective Sweeping Microscopy." *PNAS* 108, no. 41 (2011): 16889.
- Zheng, Siyang, Lin, Henry, Liu, Jing-Quan, Balic, Marija, Datar, Ram, Cote, Richard J, and Tai, Yu-Chong. "Membrane Microfilter Device for Selective Capture, Electrolysis and Genomic Analysis of Human Circulating Tumor Cells." *Journal of Chromatography A* 1162, no. 2 (2007): 154-61.
- Ziegler, JL, Bluming, AZ, Morrow, RH, Fass, L, and Carbone, PP. "Central Nervous System Involvement in Burkitt's Lymphoma." *Blood* 36, no. 6 (1970): 718-28.
- Zong, C, Lu, S, Chapman, AR, and Xie, XS. "Genome-wide Detection of Single-nucleotide and Copy-number Variations of a Single Human Cell." *Science* 338, no. 6114 (2012a): 1622-26.